DESIGNING VIRUS-LIKE NANOPARTICLES AS T_1-ENHANCED MRI CONTRAST AGENTS

by

Shefah Alma Qazi

A dissertation submitted in partial fulfillment
of the requirements for the degree

of

Doctor of Philosophy

in

Biochemistry

MONTANA STATE UNIVERSITY
Bozeman, Montana

November 2014

ACKNOWLEDGEMENTS

This great achievement and milestone in my life would not have been possible without the support and guidance of so many. First and foremost, I would like to thank my committee. Mary Cloninger, your smile, encouragement and positive attitude always brought my spirits up. Sarah Codd, your insights on MR imaging has been instrumental in pushing my projects forward. Brian Bother and Trevor Rainey, both of whom I've had the pleasure of taking classes with, thank you for always challenging me to think critically and for being available to answer questions at a moment's notice. A special thanks to Jennifer Smith, who is the reason I came to MSU. Last but not least, I want to thank my PhD advisor, Trevor Douglas, who has given me countless opportunities to learn and grow as a young scientist, for which I am forever grateful.

The success of my projects was attainable through various lab funding sources, the American Heart Association (AHA) Western Associate's Predoctoral Fellowship, and the Kopriva Fellowship. The supportive nature of the lab helped me to stay motivated on a day to day basis. In particular, Masaki Uchida, your mentorship significantly impacted my development as a graduate student. Amy Servid, my roommate and lab mate during this 5 year journey, your friendship is one I will truly miss, along with our late night brainstorms in the apartment. To all my wonderful friends and family, your support has meant so much. Shahina Akter and Dalia Roksana, thank you for giving me a home away from home. Hasim Turhan and Quarney Waiz Ali, when things got tough you put things into perspective, thanks for believing in me every step of the way. Lastly, I would like to dedicate this dissertation to my dad, who survived three heart attacks and triple bypass surgery. He has taught me that with hard work and determination, no dream is too big.

TABLE OF CONTENTS

TABLE OF CONTENTS - CONTINUED

TABLE OF CONTENTS - CONTINUED

TABLE OF CONTENTS - CONTINUED

LIST OF TABLES

Table Page

.

.

LIST OF FIGURES

LIST OF FIGURES - CONTINUED

Figure Page

LIST OF FIGURES - CONTINUED

Figure Page

LIST OF FIGURES - CONTINUED

Figure Page

LIST OF FIGURES - CONTINUED

Figure Page

ABSTRACT

The field of nanotechnology is a rapidly growing field. In the past few decades, nanoparticles have been utilized for use in biomedical applications with a huge impact in enhancing diagnostic techniques. Protein cages and virus-like particles are biological examples of nanoparticles. They are highly symmetric, well-defined architectures made from multiple protein subunits and can be genetically or chemically engineered to impart desired new functionalities and have been used for design of nanomaterials for improving current diagnostic techniques, as discussed in this thesis. One of the main techniques for diagnosis used today is magnetic resonance imaging (MRI) as it provides good spatial resolution of soft tissues without using harmful ionizing radiation. However, due to poor sensitivity of this technique, contrast agents are often utilized by clinicians to aid in diagnosis of diseased tissues. The main MRI contrast agents used in T_1-enhanced imaging are small Gd-containing molecules. Due to the toxicity of free Gd ions, these agents are administered in a tightly chelated form. Even in this form, high doses increase the risk of toxicity. Thus, it is important to reduce overall dosage of these contrast agents.

In this thesis, we discuss design principles for virus-like particle based MRI contrast agents as next generation diagnostics which can overcome the above mentioned barriers. Conjugating clinically approved contrast agents to nano-sized virus-like particles changes the intrinsic properties of the contrast agent, directly impacting and increasing MRI contrast. Modifying the interior surface of these cage-like containers to grow functionalizable polymers provides multiple sites for conjugation of small molecule contrast agents, resulting in high payload of these agents. Modifying the exterior surface of these cage-like containers to present targeting ligands and enable them to localize at desired tissues of interest. All three of these design considerations contribute to higher contrast, significantly lower clinical dose requirements, and allow for safe administration of Gd (III) ions for enhanced imaging. As gadolinium-based contrast agents are directly linked with nephrogenic systemic fibrosis, a rare but deadly disease that causes hardening of tissues and organs, an alternate low-risk metal-complex, Mn (III) porphyrins, has also been explored for bioconjugation to virus-like particles.

CHAPTER 1

INTRODUCTION

Nanoparticles have made a significant impact in material science for the past few decades, because they exhibit unique properties (e.g. magnetic, photonic and catalytic) different from bulk materials. Because the emergent properties of nanoparticles are often intimately related to their dimension, control of particle size and morphology are important.

Through millions of years of evolution, nature has developed cage-like protein assemblies that are designed to encapsulate guest molecules and protect them from the external environment.[1; 2] These protein cage architectures assemble from a distinct number of subunits to form precisely defined molecular containers in the nanometer-size range. Conceptually, there are three different interfaces presented by all protein cage nanoparticles (Figure 1.1). These are the interior and exterior surfaces as well as the interface between subunits.[3] Their interior cavity can provide a confined environment for selectively directed synthesis of polymers and other cargo while their exterior surface can provide multivalent platform for imparting targeting ability or stealth ability.

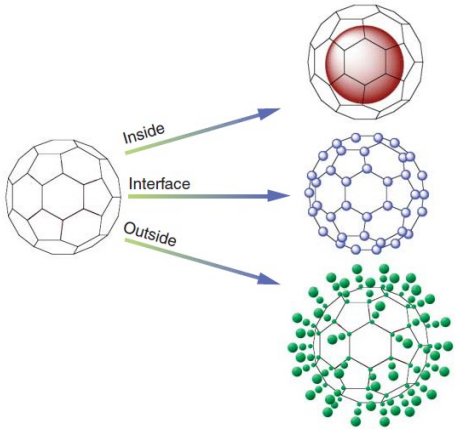

Figure 1.1: Inside Interface and Outside. Schematic of the three important interfaces of assembled protein cage architectures that are available for chemical and genetic manipulation. The outer surface, the interior surface, and the interface between subunits have all been used for the construction of multivalent, multifunctional protein cage–based materials. Taken from Douglas et. al. [4]

Examples of these cage-like architectures are chaperonins,[5-7] DNA-binding proteins,[8-13] and a very large class of protein cages – viruses.[4; 14; 15] Typically these protein cages are roughly spherical in shape and represent a range of relatively simple symmetries including tetrahedral, octahedral, and icosahedral. Materials scientists have been inspired by the natural function of protein cages and have exploited them as platforms for development of a wide range of nanomaterials.[4; 16-18] A library of functional protein cage nanoparticles that serve as platforms for such purposes as biomimetic materials synthesis, magnetic resonance imaging (MRI) contrast agents, gene therapy, drug encapsulation, cell specific targeting and catalysis are being developed. All of the protein cage nanoparticles represented in Figure 1.2, as well as many others, have also been probed by both chemical and genetic modification for adding non-native functionality and exploiting the great versatility of protein cage architectures.[1; 3; 19-26]

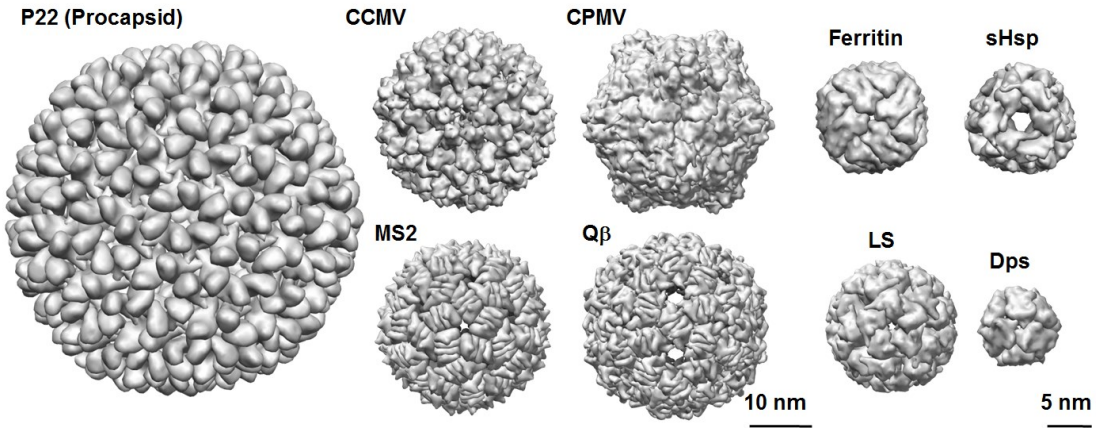

Figure 1.2: Space-filling images of protein cage nanoparticle including viral capsids P22 procapsid form (58 nm diameter) *PDB 3IYI*, CCMV (28 nm) *PDB 1CWP*, CPMV (30 nm) *PDB 1NYZ*, MS2 (27nm) *PDB 2MS2*, Qβ (30nm) *PDB 1QBE*, ferritin (12 nm) *PDB 2FHA*, small heat shock protein (sHsp, 12 nm) *PDB 1SHS*, Lumazine synthase (LS, 15nm) *PDB 1RVV,* and DNA binding protein from starved cells (Dps, 9 nm) *PDB 1QGH*. The images were reproduced using the UCSF Chimera package (http://www.cgl.ucsf.edu/chimera/) from the Resource for Biocomputing, Visualization, and Informatics at the University of California (supported by NIH P41 RR-01081) [27]. Taken from Qazi et. al. 2013. [28]

Nanoparticles in Biomedical Applications

Over the past few decades, numerous nanoparticles have been engineered for biomedical applications, due to therapeutic advantages, such as targeted drug delivery and the potential for early diagnosis and treatment of disease.[29-31] These delivery vehicles have two important advantages over delivery of drug or diagnostic agents alone. First, therapeutic and diagnostic agents can be encapsulated, covalently attached, or adsorbed on to such nano-carriers, overcoming drug solubility issues. Second, the surface of these nanoparticles can be functionalized with targeting ligands or polymers to direct their delivery to specific tissues and cells. Such approaches may enhance detection sensitivity in medical imaging, improve therapeutic effectiveness, and decrease side effects.

Ultimately, these nanoparticles can be multifunctional carriers for targeting cell receptors and simultaneously deliver drugs or diagnostic agents to the desired tissue target.[29] The next section will focus on advantages for using nanoparticles for diagnostics, in particular for their use in magnetic resonance imaging.

Development of Nanoparticle Contrast Agents for Magnetic Resonance Imaging

Medical imaging has been a technique used by clinicians to diagnose ailments of the body for over a century now. Magnetic resonance imaging (MRI) provides high-resolution images without employing harmful ionizing radiation which some of the other techniques - x-rays, cat scans, and positron emission tomography - employ. Instead, as the name implies, MRI uses nuclear magnetic resonance (NMR) to observe signals from ^1H nuclei spins of water molecules in the body, and using Fourier Transform, these signals are converted into a 3-dimensional image.

When a sample is placed in a static magnetic field, B_0, the spins of the ^1H proton nuclei (spin quantum number I = ½) are split in 2I+1=2 energy states. Boltzmann's law governs the populations of these two states. At equilibrium, the lower energy state, N_α (m=+½), is more populated than the higher energy state, N_β (m=-½). The vector sum of these spins can be represented as net magnetization, M_0, with the magnetic moments μ aligned along B_0 (z-axis) (Figure 1.3b). These magnetic moments μ revolve around the external magnetic field B_0 with an angular velocity known as the Larmor frequency, ω_L, which is identical to the angular velocity, ω_o, required to obtain a transition between the

two energy states of the nucleus.[32] The angular velocity is in turn related to the static magnetic field according to

$$\omega_0 = \gamma B_0 \qquad \text{(eq 1.1)}$$

where γ is the nuclear gyromagnetic ratio. For a hydrogen atom, $\gamma = 42.58\ MHz/T$.

At equilibrium, the magnetic moments μ precess around B_0 incoherently, or out-of-phase (Figure 1.3b). When a radiofrequency (RF) pulse is applied to the sample, two things occur. First, there is an equal population of the lower energy state, N_α (m=+½) and the higher energy state, N_β (m=-½). Also, the magnetic moments μ precess around B_0 in-phase. Consequently, this shifts M_0 from the z-axis to the xy-plane (Figure 1.3c).

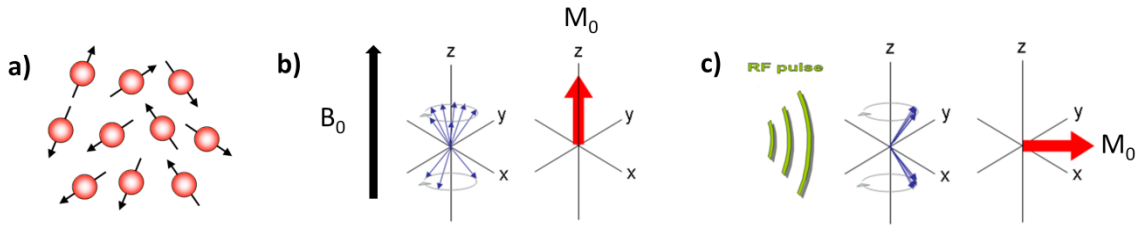

Figure 1.3: Hydrogen proton magnetization. a) Spins (black arrows) of water hydrogen protons (red circles) precess around individual magnetic fields and are randomly oriented when body is at rest. b) When body is in MRI scanner, proton spins precess around magnetic field of scanner (B_0) (blue arrows) with net magnetization in positive z-axis (red arrow). c) After a series of radiofrequency (RF) pulses are applied, spins orient up and down in same amount (blue arrows), canceling net magnetization in z-axis, and precess in-phase, shifting net magnetization is in xy-axis (red arrow). Modified from http://www.cardiff.ac.uk/biosi/researchsites/emric/basics.html.

As spins return or "relax" to thermal equilibrium states, two processes occur simultaneously. First, spins re-align with magnetic field B_0 to re-establish Boltzmann distribution, resulting in an exponential signal growth in the z-axis. This is a spin-lattice

effect, and referred to as T_1-longitudtional relaxation. (Figure 1.4a) T_1 is a time constant defined as when magnetization (M_z) recovers 63% of equilibrium magnetization or saturation (M_0).

$$M_z(t) = M_z(1 - e^{-t/T_1}) \qquad \text{(eq 1.2)}$$

At the same time, spins start to de-phase which results in an exponential signal decay in the xy-axis. This is a spin-spin effect, and referred to as T_2-transverse relaxation. T_2 is also a time constant defined as when magnetization (M_z) decays 37% from equilibrium magnetization or saturation (M_0). (Figure 1.4b)

$$M_z(t) = M_z(e^{-t/T_2}) \qquad \text{(eq 1.3)}$$

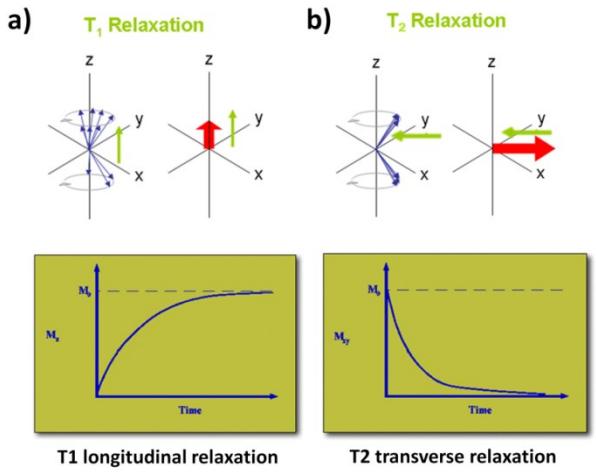

Figure 1.4: T_1 and T_2 relaxation. After a radiofrequency pulse is applied, the spins return to equilibrium state and two things happen simultaneously. a) The spins return to mostly aligned with the magnetic field of the MRI scanner, resulting in a gain in magnetization in the z-axis, and is called T_1 longitudinal relaxation process. b) The spins start precessing out of phase, resulting in a loss in magnetization in the xy-axis, and is called T_2 transverse relaxation process. T1 relaxation is due to spin-lattice effect while T_2 relaxation is due to spin-spin effect. Modified http://www.cardiff.ac.uk/biosi/researchsites/emric/basics.html.

The amount and mobility of these spins vary from tissue to tissue, thus the time it takes for the spins to return to equilibrium also vary. The signal collected is transformed into an image via Fourier Transform. The clinicians can manipulate the signal collection to be either T_1-weighted, watching a gain in magnetization signal (producing bright images) or T_2-weighted, watching a loss in magnetization signal (producing dark images), where short T_1's give bright spots and short T_2's give dark spots.

Despite the high resolution images, the technique is limited in sensitivity. This generally requires use of contrast agents which act as catalysts to enhance sensitivity for both the T_1 and T_2 relaxation process. The properties of the contrast agent determine whether they are more suited for T_1-enhanced contrast or T_2-enhanced contrast. The use of paramagnetic ions, such as Fe (III), Mn (II), and Gd (III), as contrast agents for MRI have been commonplace in the last 40 years or so, with Gd being the most widely used for T_1-enhanced contrast[33] and Fe for T_2-enhanced contrast. For the scope of this thesis, only T_1-enhanced contrast agents will be discussed from here on out. Gd (III) is by far the most effective T_1-enhanced contrast agent because it has favorable electronic properties for relaxing water proton spins quicker, with its slow electron spin and 7 unpaired electrons.[34] The main issue with Gd (III) ions is its toxicity. If administered as the free ion to the body, Gd has the potential to precipitate and can undergo transmetallation with vital metals, i.e. copper, calcium, or zinc, which are needed for the body to function. This would be lethal to the body, thus for safety, it is always administered in a chelated form. Most common ligands are linear DTPA (Figure 1.5a) and circular DOTA (Figure 1.5b) and their derivatives. The important thing to keep in mind is binding affinity must be

strong and agents must be soluble in bloodstream as mostly it's administered intravenously.

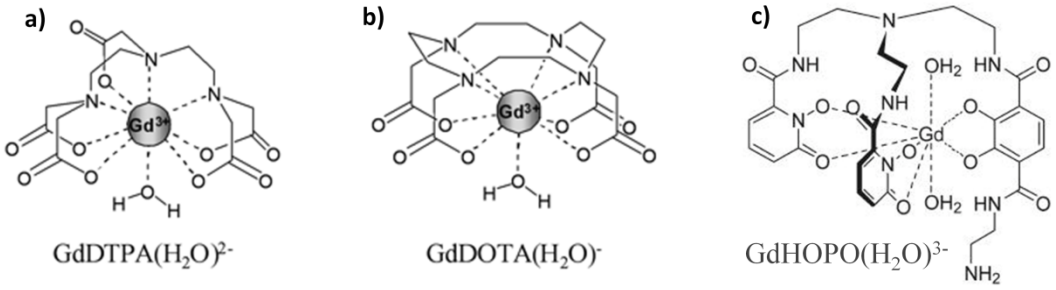

Figure 1.5: Small molecule contrast agents. a) DTPA-Gd is a common contrast agent used clinically, under the name Magnevist. b) DOTA-Gd is a common contrast agent used clinically, under the name Dotarem. c) A new ligand, HOPO, is being developed by Raymond lab in Berkeley, for binding of more water molecules to Gd, without compromising binding affinity. This is currently not available commercially. Common derivatives of DTPA and DOTA usually substitute a carboxyl arm for an amine, which result in lower binding affinity between ligand and metal, and raises concerns about toxicity.

The ability for a contrast agent to enhance image contrast is directly proportional to its relaxivity, r_1, that is, to the longitudinal relaxation rate increase of bulk water-molecules by the paramagnetic ion as defined by the principles of Solomon-Bloembergen-Morgan (SBM) theory for relaxivity.[25; 26; 38-40] It is calculated by subtracting $1/T_{1,\,H2O}$ (diamagnetic contribution from pure water) from $1/T_{1,\,obs}$ (observed relaxation time) of the solution containing the Gd complex, normalized to 1 mM Gd concentration. *(eq. 1.4)*.[35] It is reported in values of $mM^{-1}\cdot s^{-1}$ on a per mM Gd basis. Fast water relaxation is desired, thus the greater the r_1 value, the greater the contrast agent performance.

$$r_1 = (1/T_{1\,Obs} - 1/T_{1\,H2O})/[Gd] \qquad \text{(eq. 1.4)}$$

There are two contributions to relaxivity: an inner-sphere contribution, where water is directly bound to Gd, and outer-sphere contribution, where water is in bulk but still interacting with Gd. The outer-sphere relaxation is not well understood. From here-on, we will discuss inner-sphere contribution only which is given by eq. 1.5, where q is the number of coordinated water molecules, τ_m is the water residence lifetime, and $1/T_{1m}$ is the longitudinal relaxation rate.

$$r_1 = \frac{q}{[H_2O]}\left(\frac{1}{T_{1m}+\tau_m}\right) \qquad \text{(eq. 1.5)}$$

The longitudinal proton relaxation rate, $1/T_{1m}$, represents the sum of dipolar (through-space) and scalar (through-bond) mechanisms, where the scalar contribution is relatively small and often neglected.[32] The dipolar contribution includes another important term, τ_r, the rotational correlation time, which is directly proportional to r_1. To see full equations for the dipolar contribution, see Appendix B, Equation B1.

From the many parameters that effect relaxivity, q, τ_m, and τ_r have the most influence on inner-sphere relaxation and are tunable (Figure 1.6). Optimal relaxivity occurs with the following conditions: q should be maximized, τ_m should be optimized, and τ_r should be maximized, however there is a point where increase in τ_r no longer increases relaxivity.[34-36] These values for some small molecule contrast agents are listed in Table 1.1.

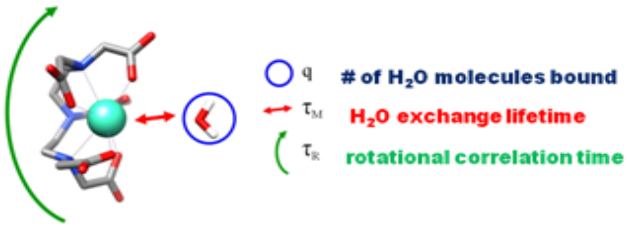

Figure 1.6: Clinically used T_1-enhanced contrast agent (*Magnevist)* with Gd^{3+} ion chelated to DTPA; parameters that affect r_1 relaxivity: q, τ_m, and τ_r. Taken from Liepold et. al. [36]

Ligand	Log K $_{Gd\ L}$	q	τ_m (ns)	τ_r (ns)	r_1 ($mM^{-1}\cdot s^{-1}$) @ 20 MHz
DOTA	24	1	122	53	3.6
DTPA	22	1	143	54	3.8
HOPO	21	2	20	15	9.0

Table 1.1: Comparison of relaxivity parameters for small molecule contrast agents

Most contrast agents have q=1, because DTPA and DOTA are octadentate, leaving only one-coordination site for Gd. However, q=2 ligands exist, with the compromise of significantly reducing binding affinity. One successful ligand which has high binding affinity and q=2 is HOPO and its derivatives (see Figure 1.5c/Table 1). These are fairly new ligands synthesized and well-studied in the Raymond group at Berkeley.[25] The main issue with HOPO-chelators is solubility which is currently being addressed by the group. The easiest of the three parameters to tune is τ_r. By conjugating DTPA-Gd to macromolecules, such as proteins, we can significantly increase τ_r, thus increasing relaxivity. This effect can be seen on a plot of relaxivity as a function of field strength, the nuclear magnetic dispersion profile (NMRD) (Figure 1.7). When small molecule contrast agents are conjugated to macromolecules, the dependence of relaxivity on field strength becomes clear. Conjugation of small molecules to nanoparticles are

well-studied and many bifunctional ligands of commercially available FDA-approved contrast agents are readily available, making it very easy for bioconjugation of small molecule contrast agents to larger nanoparticle platforms. Some of these bioconjugation techniques will be discussed further in Chapter 2.

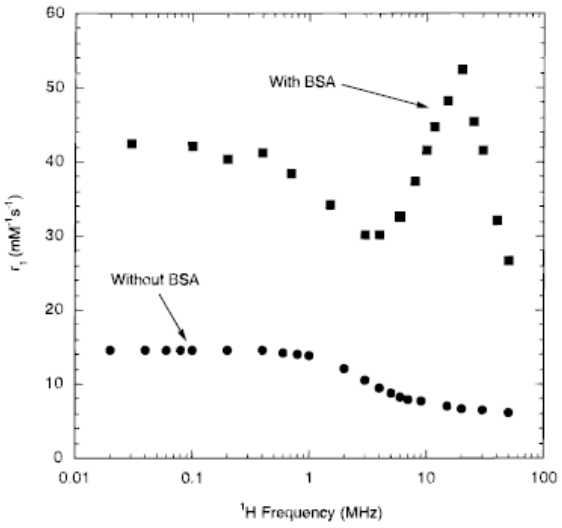

Figure 1.7. Nuclear magnetic dispersion profile (NMRD) of small molecule Gd-based contrast agent with (black squares) and without (black circles) bovine serum albumin (BSA) protein. Large increase in relaxivity due to slower tumbling of contrast agent, thus increased rotational correlation time (τ_r), consequently increasing relaxivity (r_1) with a maximum at 30 MHz. Taken from Caravan et. al. 1999.[37]

Over the past few decades, many nanoparticle platforms including lipid-based colloidal aggregates,[38; 39] linear polymers,[40] dendrimers,[41] nanodiamonds,[42] silica, gold, protein cages and virus-like particles (VLPs)[25; 26; 43-45] have been explored as efficient nanoparticle platforms for MRI contrast agents (Figure 1.8). Nanoparticles not only provide the basis for increasing τ_r,[46-48] but have two additional benefits in that large payloads of imaging agent can be delivered per nanoparticle and the nanoparticle can be directed to a specific molecular target.[49] [36; 39] This introduces a new term, instead of just

relaxivity per mM Gd, we now can consider relaxivity delivered per particle based on loading of Gd/particle. Thus, nanoparticle based MRI contrast agents can provide significant improvements in traditional biological imaging of cells and tissues and have potential to have highly desirable properties which clinicians seek.

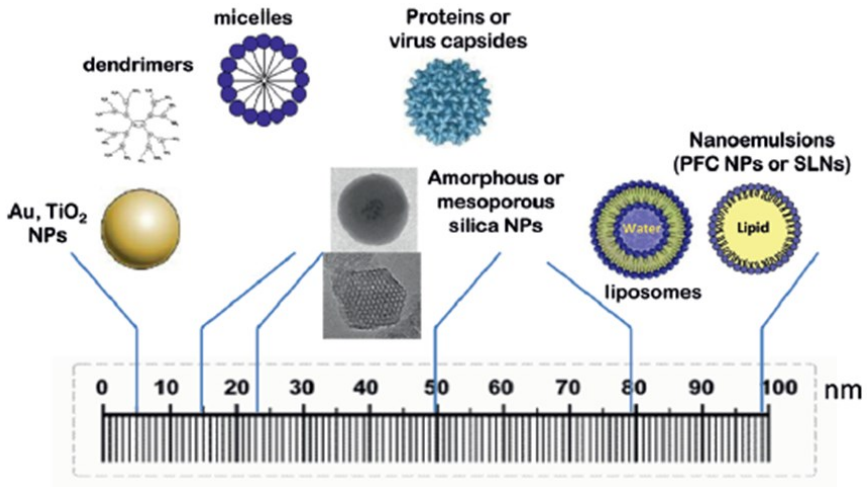

Figure 1.8: Some examples of nanoparticles as Gd-based MRI contrast agents represented in their size range. Modified from Botta et. al. 2012.[50]

All the nanoparticle platforms have benefits and disadvantages, which will be discussed briefly here. Lipid based nanoparticles have the benefit of being highly multivalent, thus having many sites where Gd can bind, resulting in a high loading delivery system. However, as Gd needs to directly interact with water to result in efficient relaxivity, lipid based systems have the downside of reduced water access to its hydrophobic center. So, only Gd on surface of lipids is accessible. There are also issues with controlled size of lipids and possibility of producing multilayer lipids. These issues make lipid-based systems difficult to characterize. Polymer and dendrimer-based systems also are highly multivalent but can also be highly polydisperse, again making them hard

to characterize. In addition, it has been found that close proximity between Gd-Gd ions has a negative impact on relaxivity which can occur in high generation dendrimers. Silica, gold, nanodiamonds[37; 45] or other carbon based systems have been shown to have a very positive effect on relaxivity and are being explored further by other groups. Lastly, protein cages and virus-like particles (VLP) are a new generation of nanoparticle based contrast agents. [36; 51; 52 26; 39]

These VLP based systems are greatly advantageous over the other systems for multiple reasons. First, they are well-controlled monodisperse, multivalent particles. They form into shell-like structures from multiple copies/subunits of proteins. The protein is a natural polymer that has modifiable surfaces with amino acid side chains such as primary amines of lysine, carboxyl groups of glutamic acid, or sulfur reactive groups of cysteine. In addition they can be genetically manipulated to have controlled addressable reactive groups from point mutations or even add certain small peptides as targeting ligands to bind to specific cell targets. [23; 53-66]

Due to the potential for enhancement of the loading capacity of protein architectures by building polymer scaffolds inside the empty inner sphere of protein cages, protein-polymer composites hold great promise as metal chelate carriers for next generation MRI contrast agents, and has been the main focus of this thesis.

Research Directions

The work described in this thesis has been inspired by the unique properties of nanoparticles which make them desirable for biomedical applications, specifically in the

design of T_1-enhanced MRI contrast agents from virus-like particles. In Chapter 3, the exterior surface of Qβ has been modified via two different bioconjugation techniques, Cu (I) catalyzed "click" chemistry (AACC) and atom transfer radical polymerization (ATRP). The ATRP polymer was subsequently functionalized with a small molecule contrast agent, Gd-DOTA. This construct had high loading capacity, and consequently had high ionic and particle relaxivities. In Chapter 4, the AACC approach of step-wise polymerization was extended to a larger virus-like particle, P22, up to generation 4.5. Instead of modifying the exterior surface, as was done with Qβ, the polymer was constrained to the interior surface of the capsid, such that the exterior surface was available for attachment of targeting ligands. The "click" polymer was functionalized with a different small molecule contrast agent, Gd-DTPA. By using a larger particle, the loading capacity was increased leading to higher ionic and particle relaxivities than with Qβ. In Chapter 5, ATRP was utilized to modify the full interior cavity of P22, in a simple one-step reaction, and subsequently labeled with Gd-DTPA. This resulted in one of the highest reported particle relaxivities of an MRI contrast agent to date. In Chapter 6, manganese porphyrins are conjugated to P22-ATRP in high payload. Manganese is explored as a T_1-enhanced contrast agent as an alternative to gadolinium based contrast agents, due to associated toxicity with gadolinium. Chapter 7 explores modification of the exterior surface of P22 for attachment of targeting ligands using two approaches, toward detection of atherosclerosis.

CHAPTER 2

BACKGROUND

The virus-like particle nanoparticle based MRI contrast agents described in the following chapters were inspired from viruses and virus-like particles. This chapter will discuss some general information and additional background on the virus-like particle platforms used in this thesis and the techniques used to modify these particles for use as MRI contrast agents. Additional background will be provided on three important design principles for developing protein cage nanoparticles as MRI contrast agents: 1) Increasing rotational correlation time (τ_r) of Gd-based small molecule contrast agents and general bioconjugation techniques. 2) Use of virus-like particles and protein cage nanoparticles to achieve high payload of Gd-based small molecule contrast agents. 3) Potential targets and display of targets on virus-like particles. In addition, potential toxicity issues with these particles will be discussed.

Viruses and Virus-Like Particles

Viruses and virus-like particles, an abundant subclass of protein cage nanoparticles,[67] are exquisite examples of supramolecular assembly that represents the organization of subunits into a precisely defined, stable protein cage.[4] Viruses come in many shapes and sizes and are extremely diverse in their life cycles and mechanisms of infection (Figure 2.1). However, many share a common structure based on icosahedral symmetry, consisting of an inner core of condensed nucleic acid within a spherical protein capsid. All viruses function by using protein or protein/lipid capsids in order to

protect and transport their nucleic acid to a host cell. They are metastable structures poised between the stability required for packaging and transport and the necessary instability associated with cargo release and infection. Many viruses package their genomic nucleic acid through non-covalent electrostatic interactions with the protein cage interface or through physical packaging at extremely high pressure, which indicates the unique distinction between the interior and exterior surfaces.

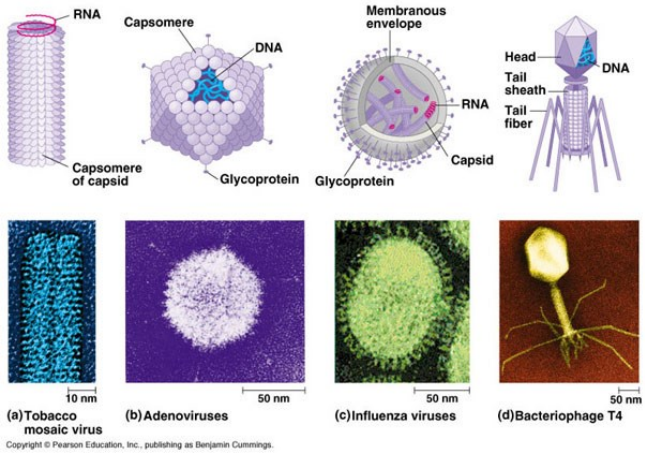

Figure 2.1: Different size and shape of viruses. Retrieved from http://learnsomescience.com/ microbiology/viruses-viroids-and-prions.

Virus-like particles, devoid of their genetic material, allow for significant flexibility with respect to cargo loading, targeting abilities, and controlled morphology of the capsids, and are thus desirable platforms for materials scientists and biomedical applications.[1; 4] This dissertation focuses mainly on the manipulation of P22 virus-like particles for the design and construction of MRI contrast agents, and will be discussed in more detail in the following section.

Bacteriophage P22

The bacteriophage P22, which infects *Salmonella typhimurium*, has been extensively studied over the years as a model system for virus assembly for double stranded DNA (dsDNA) viruses.[68; 69] Like most dsDNA viruses, assembly is a 2-step process. [70] In the first step, a precursor capsid is formed, denoted as the procapsid. In the second part of the process, dsDNA is packaged into the procapsids via an assumed ATP hydrolyzing complex.[71; 72] The assembly process of the icosahedral (T=7) short-tailed P22 bacteriophage is complex and consists of multiple gene products (gp) as outlined in Figure 2.2.[73] The procapsid is formed from gp5 (coat protein), gp8 (scaffold protein), and gp1 (portal protein), along with other gene products (Figure 2.2i). Attachment of gp2 and gp3 initiate the maturation process and packaging of DNA (Figure 2.2ii). As DNA is packaged, two critical structural changes occur: 1) gp8 (scaffold protein) leaves the capsid (Figure 2.2iii) and 2) P22 capsid expands by 10% in linear dimension and doubles in volume (Figure 2.2iv), changing morphology into a mature expanded form. Once the DNA is packaged to full capacity, referred to as a "headful" mechanism, gene products for terminase (Figure 2.2iv) and tail spike (Figure 2.2v) attach to gp1 (portal protein), and the capsid becomes infectious, ready to infect a host cell.

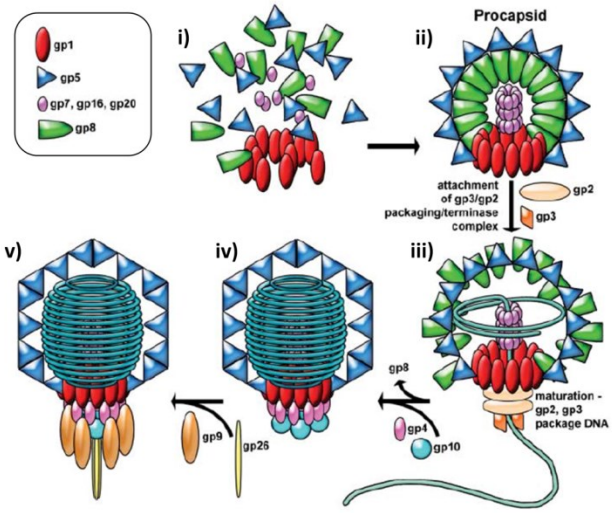

Figure 2.2: Assembly process of bacteriophage P22. (Adapted from Lander et. al.[73])

It has been shown that the 58 nm P22 procapsid (PC) can self-assemble in a non-infectious form, produced recombinantly in *E. coli*, using only gp5 (coat protein) and gp8 (scaffold protein).[74-76] This procapsid (PC) assembles from 420 subunit copies of a 46.6 kDa coat protein and up to 300 copies of a 33.6 kDa scaffold protein. The procapsid (PC) form can further undergo structural transformations which result in three different stable morphologies; empty shell (ES, 58 nm), expanded shell (EX, 64 nm) and wiffleball (WB, 64 nm), Figure 2.3. Upon treatment with guanidine hydrochloride (GuHCl), the scaffold protein leaves procapsid, making empty shell (ES).[77-81] If the procapsid or empty shell is heated to 65°C for 20 min, it undergoes a conformational change with an expansion of 10% in diameter and doubles in volume, resulting in a morphology similar to expanded head of P22 with packaged DNA, and it is called expanded form (EX).[82] If procapsid or expanded shell is heated to 75°C for 20 min, then it undergoes another conformational change to the wiffleball (WB) form, where twelve of the pentamers in the icosahedron are ejected leaving large 10 nm pores on the structure.[76; 77; 83] This form is not

biologically relevant in the life cycle of the bacteriophage, but is relevant in the design and utility of nanoparticles for easy exchange between the environment and capsid interior.

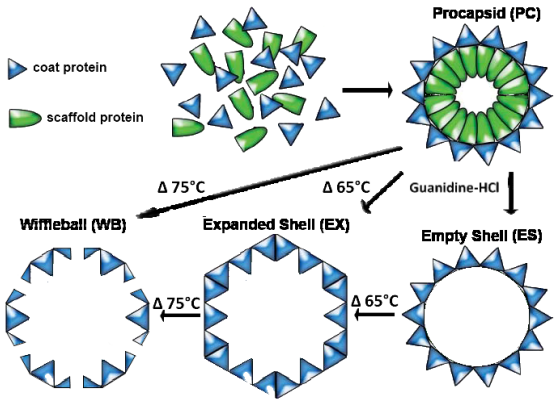

Figure 2.3: Non-infectious P22. (Adapted from Lander et. al.[73])

Because structural models exist for P22 capsid in all three of its forms (Figure 2.4), rationally designing and genetically engineering the capsid for site-selective modification exclusively to the interior or exterior surface of the capsid is possible.

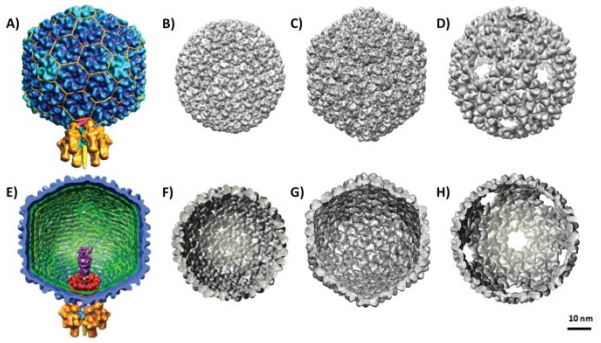

Figure 2.4. A 17 Å resolution asymmetric reconstruction of the infectious P22 virion (A). Cryo-EM reconstruction, showing exterior surface of capsid, of PC and ES, PDB ID: 3IYI (B), EX, PDB ID: 2XYZ (C) and WB, PDB ID: 3IYH (D). Cutaway views, showing interior surface of capsid, of infectious P22 virion (E), PC and ES (F), EX (G), and WB (H). Images were made using UCSF chimera, with the exception of (A) and (E), which were adapted from Lander et. al.[73]

Techniques for Achieving High Payload of Contrast in Virus-Like Particles

Several groups have made important contributions in the development of virus-like particle nanoparticles as MRI contrast agents. To date, there are four major categories, 1) endogenous metal binding sites,[84] 2) genetic insertion of a metal binding peptide,[44] 3) chemical attachment of small molecule chelates,[25; 26; 43] and 4) protein-polymer hybrid particles.[51] The majority of these complexes have been synthesized by chemically attaching derivatives of clinically employed contrast agents, such as Gd-DOTA (Dotarem), Gd-DTPA (Magnevist), and Gd-HOPO,[85] directly to functional groups on these protein cages.

The first chemists to turn toward the study and application of a viral scaffold as a candidate for complexation of gadolinium were Allen et. al.[84], with their study of the 28 nm-sized cowpea chlorotic mottle virus (CCMV) which offers 180 intrinsic metal binding sites at the three-fold axes of the icosahedral capsid structure. Under physiological conditions Ca^{2+} ions are bound to these sites, which were replaced with up to 140 Gd^{3+} or Tb^{3+} ions. In a subsequent study, genetic engineering was used to incorporate metal binding peptides to further enhance Gd-loading and affinity, yielding loadings of 172 Gd per CCMV,[44] which still holds the highest relaxivity value per Gd reported to date. However, in both cases, the particles could not be utilized for *in vivo* applications, due to low binding affinity of Gd to the endogenous and engineered binding sites of CCMV, thus increasing potential risk of toxicity of releasing Gd. An alternative approach to get high payload of Gd without the risk of releasing free Gd was

bioconjugation of highly stable NHS-DOTA-Gd to endogenous lysines on CCMV resulting in 60 Gd-DOTA per CCMV.[44]

Other systems have also been utilized for high payload of Gd. The 30 nm-sized cowpea mosaic virus (CPMV) underwent a two-step bioconjugation protocol to covalently link Gd-DOTA to its exterior surfaces via azide-alkyne click chemistry to yield 80 Gd per CPMV.[45] The Francis Lab at UC Berkeley has focused their efforts toward engineering the 27 nm-sized bacteriophage MS2 for high payload of Gd, utilizing a HOPO-chelator to conjugate to the surface of MS2, resulting in loadings ranging from 81-180 Gd per MS2.[25; 26; 86] To attain even higher loading per virus-like particle, constrained polymer networks can be grown inside these nanocontainers which contain functional groups for bioconjugation of small molecule contrast agents. Some polymerization techniques will be discussed in the next section.

Polymer Formation Inside Protein Cages Nanoparticles

There are two well-established methods for conjugating polymers to proteins, "grafting to" and "grafting from". The "grafting to" method involves synthesis of polymers with reactive chain-ends, which are subsequently attached to reactive groups on amino acid side chains of proteins and small peptides, the best known example being PEGylation of a protein.[87] This method has several shortcomings, including steric hindrance between protein/peptide and polymer, issues with separating final product from excess polymer, and typically results in a heterogeneous product which can be a problem for biological applications.[88]

In contrast, the "grafting from" approach, involves first attaching a small polymer initiator molecule to the protein, followed by growing the desired polymer from the initiator. By using this approach, steric hindrance is significantly reduced and conjugation efficiency is enhanced.[89] This approach produces two new problems: (1) synthesis of site-specific/stoichiometric conjugates in order to produce homogenous products and (2) growing the polymer from the protein in an aqueous environment.

The issue of site-specific conjugation can be easily dealt with when using protein cage nanoparticles as platforms, due to their controlled assembly and ability to be genetically and chemically modified at known sites. Among others,[90] two methods of polymerization have been adapted for synthesis under aqueous solutions, Cu (I) catalyzed azide alkyne cycloaddition "click" chemistry (AACC)[91-95] which is a step-wise polymerization technique and atom transfer radical polymerization (ATRP),[96-100] a standard example of the "grafting from" method. Both of these methods have been explored as polymerization techniques on the surface of Qβ (see Chapter 3) and interior surface of P22 capsids (See Chapters 4-6), for further functionalization toward its design as T_1-enhanced MRI contrast agents. The following sections will cover these methods in more detail.

Azide-Alkyne Click Chemistry (AACC)

The term "click chemistry" was first coined by Sharpless et. al. in 2001,[101] though [3+2] cycloadditions were introduced years ago by Huisgen{, 1961 #289}, and since have been employed by many researchers due to its simplicity. The chemistry involves a [3+2] cycloaddition between an azide and an alkyne and affords a 1,2,3-

triazole. However, this reaction yields both the 1,4- and 1,5-regioisomer addition products, see Figure 2.5.[95] In 2002, it was shown independently by Sharpless et. al[93] and Meldal et. al.[102] that a copper (I) catalysis of the 1,3-dipolar azide–alkyne cycloaddition (AACC) between an azide and a terminal alkyne results exclusively in the 1,4-regioisomer (Figure 2.5).

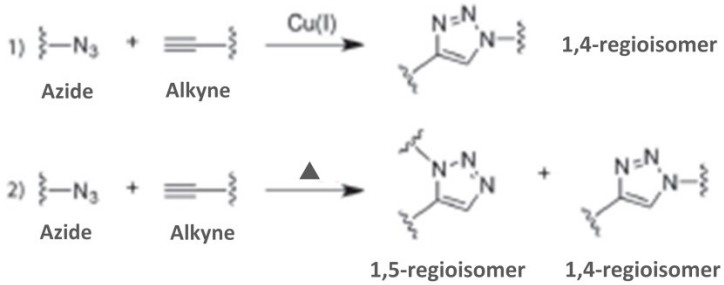

Figure 2.5: Azide-alkyne click chemistry in the presence of Cu (I) catalyst (1) versus heat (2). Adapted from Xi et. al. 2014. [95]

Considerable work has been done to improve the compatibility and efficiency of this click chemistry with biomolecules employed for the addition of peptides, fluorophores, and glycopolymers on the surface of protein cages.[101; 103; 104] Under biomolecule amenable conditions, the alkyne and azide functional groups are coupled through hetero [3+2] cycloaddition reactions mediated by a Cu (I) catalyst in the presence of a Cu-binding ligand, THPTA.[105; 106] This chemistry has been extensively explored by the Finn group for application to protein cages with the development of reaction modifications to protect the protein component and ensuring retention of the copper catalyst activity. Early applications of this approach include the click based attachment of Gd-MRI contrast agents to CPMV.[45] While effective, the reagents required that all

reactions be performed in a strict inert atmosphere. Further improvements to the process were made by changing the copper ligand and through the addition of molecules (such as amino guanidine for protection against protein damage) to the mixture, which allow the reaction to be mixed in a sealed vessel without extensive treatment to keep the reaction anoxic.[105] In this reaction mixture, any oxidized copper is regenerated by the presence of sodium ascorbate, while amino guanidine acts as a radical scavenger protecting the protein from reactive species generated by the sodium ascorbate and copper. These modified conditions have provided a streamlined path towards a variety of protein-conjugate type syntheses. This reaction type, while useful for the specific coupling of molecules to proteins, can also be used iteratively for the stepwise formation of a polymer, similar to the formation of a dendrimer. Click chemistry has been applied towards the synthesis of addressable organic polymers inside both sHsp[36; 51; 107] and the P22 VLP[108] (See Chapter 4) for the formation of an improved MRI contrast agent.

Atom Transfer Radical Polymerization (ATRP)

Of the several continuous biomolecule-anchored polymerization methods, the use of ATRP is particularly suited for improved formation of polymers inside protein cages. This method is not only rapid, monomer promiscuous, and results in products with relatively low polydispersity, but also the simplicity of the ATRP initiator means that it can be readily modified for amending to biomolecules (Figure 2.6). By combining ATRP with a container-like protein, the formation of a polymer scaffold constrained to the interior of protein cage nanoparticles can be afforded in a single short reaction.

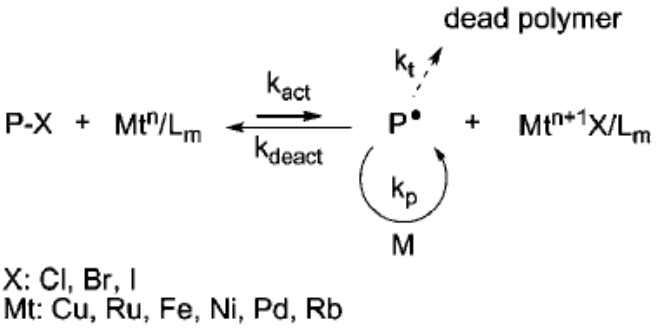

Figure 2.6: The activation-deactivation equilibrium in atom transfer radical polymerization (ATRP). Taken from Droumaguet et. al. 2010 [97]

The first report of using ATRP as a grafting-from method describes the modification of streptavidin with a modified biotin initiator for the successful growth of N-isopropyl acrylamide polymers (NIPAM).[109] Another early report of this method describes the use of BSA or lysozyme with a NIPAM polymer grown from a cysteine attached initiation site.[110] This approach has been used to build protein-polymer composites on surfaces of virus-like particles for bioconjugation to small molecule contrast agents, which result in high payload of contrast and high particle relaxivities.

Techniques for Increasing Rotational Correlation Time, τ_r

An additional advantage of using virus-like particles and other nanoparticles as platforms for MRI contrast agent development is the slow tumbling rates of these large macromolecular structures. The Solomon-Bloembergen-Morgan theory of paramagnetic relaxivity enhancement predicts that increasing the rotational correlation time of a paramagnetic ion (i.e. Gd^{3+}) which has a relatively long electronic relaxation time will increase the ion's relaxivity in the range of clinically relevant field strengths.[111-113] The

molecular dynamics of such paramagnetic ions dominate the dipole – dipole interactions between their unpaired electrons and the water protons in the inner shell.[114; 115] Macromolecules, such as polymers, dendrimers, lipids, gold nanoparticles, silica, and protein-based systems have a bulky physical structure which in turn results in slow rotation of the large molecules. By coupling a small molecule contrast agent or paramagnetic ion to these larger structures, the rotational correlation time, τ_R, is increased and consequently results in enhanced relaxivity and more enhancement per unit dose of the paramagnetic ion.[116] Some of the common ways to reduce contrast agent mobility has been (1) distributing the agent into a tissue with high viscosity. (2) Non-covalent binding of the complex to macromolecule. (3) Covalent attachment of the complex to macromolecules.

Distributing the agent into a tissue with high viscosity is not so much as a technique for reducing rotational correlation time, as it is to better understand how relaxivity changes in aqueous solutions versus in an *in vivo* environment. Small molecule contrast agents, such as Gd-DTPA, localize primarily in the intravascular and interstitial compartments of tissues and have similar relaxivities to those observed in aqueous solutions. On the other hand, studies have revealed modest increases in τ_r of small molecule imaging agents in intracellular environments which exhibit higher viscosity as compared to aqueous solutions.[117; 118]

Non-covalent binding of gadolinium complexes to high molecular weight, endogenous proteins theoretically presented an ideal situation, where the macromolecule would allow the contrast agent to have longer retention time and longer τ_r and higher

contrast in the body, while non-covalent binding allows rapid renal clearance of the small molecule contrast agent. Lauffer et. al.[119] first investigated reversible binding of MS-35, an amphiphilic, monomeric, gadolinium (III) chelate, to small serum protein albumin. Although albumin-bound agent had greater relaxivity, imaging instruments could not differentiate among enhancement from the free MS-35 and protein bound MS-35 forms, and thus, the signal represented a dynamic average of the relative proportion of the two states of the contrast agent.

Instead, by rigidly attaching chelates to macromolecular agents, contrast enhancement would be represented by a single population. The choice of the Gd (III)-chelate to be used in the conjugation with the macromolecular system depends on the functional group present on the macromolecule. Bifunctional chelating agents containing a polyamino polycarboxylic ligand (i.e DTPA or DOTA and their derivatives) are capable of strongly coordinating the Gd^{3+} ion on one side while a functional group on the other side is able to form a stable covalent bond with the carrier.[120] These agents can be conjugated through a large variety of chemical bonds, the most common being the amide, through reaction with an activated carboxyl acid with an amine, and thiourea, via reaction of a thioisocyanate with an amine. Other linkages can be obtained through reaction of maleimides or disulfides with thiols, aldehydes or isocyanates with amines. In addition to these more traditional conjugation chemistries, orthogonal chemistries such as Cu(I)-catalyzed azide-alkyne cycloaddition (click chemistry)[92], diazonium coupling, and oxime ligation are highly efficient alternatives. This is helpful when reagents are scarce, expensive or if water solubility is a problem. Silica and gold nanoparticles can also be

conjugated with bifunctioncal chelators which have trimethoxy and thiol groups, respectively.[121]

Targeting

Nanoparticles in the size range of 20–200 nm can accumulate inside the interstitial space at sites of inflammation or diseased tissues, due to increased pore size at these sites.[122] This phenomenon is known as the enhanced permeability and retention (EPR) effect, and can been exploited for the passive targeting of disease.[123; 124] The EPR effect has been observed with a variety of nanoparticle systems including polymers, liposomes, and protein cages.[125] In addition to passive targeting, protein cages can also be modified with various ligands to generate targeting through molecular recognition of molecules on specific cells or tissues.

Phage display is a powerful technique utilizing the protein cages of infectious virions for the isolation of peptides or capsids that bind to target molecules. DNA technology is used to construct a library of phages, and successive binding and isolation steps are used to select phages with the highest affinity for substrates of interest. These steps ultimately lead to a fairly homogenous population, for which the binding regions of a phage of interest can be isolated and sequenced. *In vivo* phage display has resulted in the identification of peptides that recognize proteins upregulated in certain tissues or disease states. The RGD,[126] LyP-1,[127] and VCAM-1[128] peptides were some of the first isolated sequences for in vivo targeting and have been displayed on a variety of surfaces for cell adhesion and targeting applications. Targeting peptides for integrins expressed on

cell surfaces[127] or for specific cellular compartments have been extensively used to direct the location of protein cage platforms.[129] Targeting allows for the localization of an imaging agent or drug.[130] The expression of the RGD peptide on surface of virus-like particles is explored in Chapter 7.

Toxicity and Immunogenic Response Associated with Gd-Loaded Virus-Like Particles

Nephrogenic Systemic Fibrosis (NSF)

Administering gadolinium based contrast agents (GBCAs) for magnetic resonance imaging (MRI) is pretty common practice and known to be safe to be administered at low doses. Although quite rare, nephrogenic systemic fibrosis (NSF) is a very serious condition that occurs in 6% of patients exposed to GBCAs.[131] The first reports of nephrogenic systemic fibrosis (NSF) were made in the 90s, and links between NSF and GBCAs were established in 2006. Time has shown that two factors are important for the development of NSF: (1) reduced renal function and (2) exposure to one of the less stable gadolinium-based contrast agents.[131-146]

NSF is a disorder that causes hardening of the skin and some organs and could be lethal. The mechanism for disease occurrence is unknown, although it is speculated that it is free Gd, not the Gd-ligand complex, which undergoes transmetallation with essential metals in the body, i.e. Zn, Cu, Ca, and signals a cascade reaction from the immune system which causes NSF. The most reported cases of NSF are associated with non-linear, non-ionic GBCAs, due to them being the least stable metal-ligand complex.[144] This aspect should be considered in design principles of macromolecular GBCAs. Now

that it has been brought to the attention of physicians and radiologist community, the occurrence of NSF has been reduced. However, it is important to look for safe alternatives such that patients with renal failure who need contrast agent MRIs have an option. One such option using Mn (III) porphyrins has been explored in Chapter 6.

Immunological Concerns

Although not covered in this thesis, immunological concerns in developing virus-like particles for *in vivo* applications should be addressed. While recognition of VLP platforms holds tremendous potential for medical applications, the immunogenicity of these architectures may limit their usefulness. Nanomedical applications that require more than one administration of the cage are bound to face increasing scrutiny due to the difference between the primary and secondary immunes, resulting in uncertainties about the *in vivo* effects of the protein cage therapeutic upon a second administration. Therefore, the design of protein cages that require only one administration or the usage of these constructs in situations where the potential benefit is greater than the risk involved may prove more fruitful for in vivo applications. An alternative approach is the masking of protein cages such that they are not as easily recognized by the immune system, and polymer coated particles show potential in this area. The masking of the exterior of protein cage surfaces from the immune system for applications in which immune responses are not desired can be accomplished through decoration of protein cages with homogenous polymers such as polyethylene glycol. Pegylation of CPMV[23] and MS2[59] capsids resulted in the reduction of antibodies generated against these constructs. Pegylation can inhibit proteolytic degradation and extend the circulation time of drug

carriers in vivo.[147] A more recent strategy to mitigate immune responses to carriers involves the decoration of carriers with "self" molecules or peptides to inhibit recognition.[148]

Conclusion

Viruses and virus-like particles are the inspiration for this work. In this thesis, the use of virus-like particles as nano-platforms for MRI contrast agent development and enhancement will be discussed. Three important design principles govern the modifications made to the virus-like particles: 1) Increasing rotational correlation time (τ_r) of Gd-based small molecule contrast agents. 2) High payload of Gd-based small molecule contrast agents per virus-like particle. 3) Expression of targeting peptides for display on surface of virus-like particles. Building organic polymers in virus-like particles provides not only a means to stabilize the architecture, but also a means to create a high density of attachment sites for active molecules such as Gd-chelates. Future viral capsid based materials will likely enable the development of a clinically translatable MR imaging probe for diagnosis of atherosclerosis using a disease-targeted virus capsid which may give insight into potential treatment of the disease. In addition, potential toxicity issues were discussed and alternatives were suggested.

CHAPTER 3

FUNCTIONAL VIRUS-BASED POLYMER-PROTEIN NANOPARTICLES BY ATOM TRANSFER RADICAL POLYMERIZATION

Contributions of Authors and Co-Authors

Manuscript in Chapter 3

Author: Jonathon K. Pokorski

Contributions: Designed and carried out the experiments and wrote the manuscript.

Co-author: Kurt Breitenkamp

Contributions: Designed and carried out the experiments.

Co-author: Lars Liepold

Contributions: Characterized the samples by NMR and analyzed the relaxivity data.

Co-author: Shefah Qazi

Contributions: Characterized the samples by NMR and analyzed the relaxivity data.

Co-author: MG Finn

Contributions: Obtained funding, coordinated the project, and assisted with the design of the experiments. Discussed the results and edited the manuscript at all stages.

Manuscript Information Page

Authors: Jonathan K. Pokorski, Kurt Breitenkamp, Lars Liepold, Shefah Qazi, and M.G. Finn
Journal: Journal of the American Chemical Society
Status of Manuscript:
____ Prepared for submission to a peer-reviewed journal
____ Officially submitted to a peer-reviewed journal
____ Accepted by a peer-reviewed journal
_X__ Published in a peer-reviewed journal

Publisher: American Chemical Society
Date of Submission: 2011
Issue in which manuscript appears: Volume 133, 9242-9245

CHAPTER 3

FUNCTIONAL VIRUS-BASED POLYMER-PROTEIN NANOPARTICLES BY ATOM TRANSFER RADICAL POLYMERIZATION

Published: *J. Am. Chem. Soc.*, **2011**, 133, 9242-9245.

Jonathan K. Pokorski,[†] Kurt Breitenkamp,[†] Lars O. Liepold,[‡] Shefah Qazi,[‡] and M.G. Finn[*,†]

[†]Department of Chemistry and The Skaggs Institute for Chemical Biology, The Scripps Research Institute, La Jolla, California 92037, United States

[‡]Department of Chemistry, Center for BioInspired Nanomaterials, Montana State University, Bozeman, Montana 59717, United States

Abstract

Viruses and virus-like particles (VLPs) are useful tools in biomedical research. Their defined structural attributes make them attractive platforms for engineered interactions over large molecular surface areas. In this report, we describe the use of VLPs as multivalent macroinitiators for atom transfer radical polymerization (ATRP). The introduction of chemically reactive monomers during polymerization provides a robust platform for post-synthetic modification via the copper-catalyzed azide-alkyne cycloaddition reaction. These results provide the basis to construct nanoparticle delivery vehicles and imaging agents using protein-polymer conjugates.

Introduction

Synthetic polymers are chemically diverse in terms of their size and composition, and have long been used for the display of multiple copies of functional units. In contrast to their synthetic counterparts, biopolymers such as viruses and virus-like particles (VLPs) exhibit unique qualities of monodispersity and chemical regularity, allowing for the precise, periodic chemical functionalization of capsid structures.[149; 150] VLPs can be both genetically[151] and chemically[150] modified to alter or introduce functionality and tailor biological functions. The combination of these two types of multivalent structures may prove advantageous in situations requiring organic nanoparticles with defined structural attributes.

Synthetic polymer nanoparticles prepared by emulsion, nanoprecipitation, self-assembly, or layer-by-layer techniques have been widely studied as delivery vehicles.[152]

Their potential advantages include high drug-loading capacities, ability to improve drug solubility, and the ready introduction of ligands for targeted delivery.[153] However, the production of polymeric nanoparticles with precise structural homogeneity remains a challenge to the field.[154] The use of biomolecular platforms is an attractive approach toward this end, and many examples exist of the modification of viral and non-viral protein structures with synthetic polymers using 'grafting to' approaches.[59; 116; 155; 156] In contrast, there are few examples of the use of protein nanoparticles as multivalent macroinitiators for polymerization,[157-159] and none using viruses.[160]

We describe here the radial polymerization of octa(ethylene glycol)-methacrylate (6, OEGMA) and the azido-functionalized analogue (7, OEGMA-N_3) directly from the surface of the bacteriophage Qβ virus-like particle by atom transfer radical polymerization (ATRP). ATRP and other controlled radical polymerization techniques have previously been used to prepare well-defined polymer-protein hybrid structures that maintain their biological functions while gaining improved pharmacokinetic properties.[109; 110; 161; 162] We expected ATRP to provide polymers with narrow molecular weight distributions, yielding structurally uniform hybrid protein-polymer nanoparticles from the monodisperse viral platform.

Results and Discussion

ATRP initiators were installed on the surface of Qβ using a two-step 'click' protocol (Figure 3.1), which would allow other functional units to be installed at the same time if desired. First, *N*-hydroxysuccinimide 3 was used to attach an azide group to

approximately 180 ± 30 of the 720 surface-accessible amine groups of the particle (a value that is controlled by the selection of reaction conditions for this step, and determined experimentally by mass spectrometry analysis of the denatured protein after modification). The resulting azido-particle 3 was then functionalized with a triglyme-based ATRP initiator (4) by copper-catalyzed azide-alkyne cycloadditon (CuAAC) to form Qβ macroinitiator 5.[105; 163] Polymers were grown from the multivalent initiator using a 2,2'-bipyridine/CuBr/$CuBr_2$ catalyst system that was previously shown to yield high-molecular weight polymers grafted from protein-based initiators in water.[164] A degassed, aqueous copper solution (0.1 mM final concentration) was added to a solution of particle 3 and the commercially available monomer 6 or 7 (final concentrations: 1 mg/mL (0.4 μM) in VLP and 72 mM in monomer). After overnight room-temperature reactions under nitrogen, the polymerizations were terminated by exposure to air and addition of EDTA. The resulting protein:polymer conjugates were purified from the small molecule reactants by sucrose gradient centrifugation and ultrapelleting.

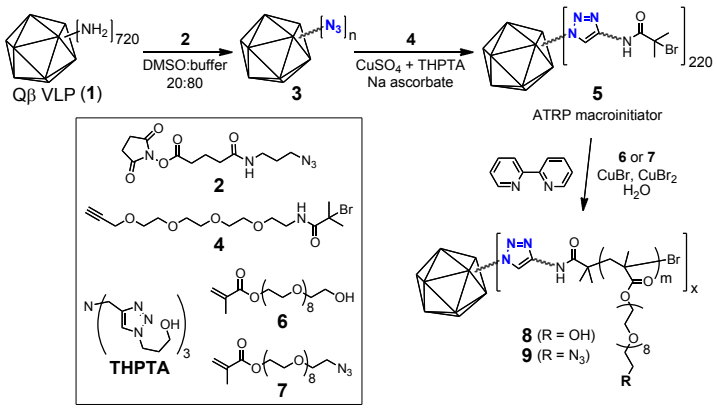

Figure 3.1: Preparation of the Qβ VLP macroinitiator and polymerization from its surface.

Size exclusion chromatography (SEC) and dynamic light scattering (DLS) were used to determine changes in particle size following ATRP. The former (Figure 3.2A) showed a shift in elution volume from approximately 12 min for unmodified Qβ particles to 9.5 min for the significantly larger poly(OEGMA)-coated product. A similar shift was seen in electrophoretic mobility when the particles were analyzed on a native agarose gel, where polymer coated particles remained near the baseline, a significant retardation compared to particle 5 (Figure 3.2D). DLS measurements (Figure 3.2E,F) confirmed the increase in particle hydrodynamic radius from 14 nm (Qβ wild-type) to approximately 24 nm for the polymer-coated particles, with a narrow size distribution (polydispersity = 18%). The virus capsids, when visualized by TEM, were shown to remain intact following ATRP (Figure 3.2B,C).

ATRP provides a tertiary bromide at the terminus of each growing polymer chain, which is amenable to further transformation.[165; 166] As shown in Figure 3, we reacted particle 8, which does not contain side-chain azide functionality, with a large molar excess of sodium azide in a water:DMSO mixture to substitute azide for bromide at the particle periphery. The resulting intermediate was then reacted with AlexaFluor488-alkyne under standard CuAAC bioconjugation conditions. Following sucrose gradient purification, the fluorescent particles were found to bear an average of approximately 20 dye molecules per particle by comparing Alexa UV absorbance (495 nm) versus total protein concentration (as measured by Bradford assay). No observable dye labeling occurred when 8 was subjected directly to CuAAC prior to sodium azide treatment, suggesting that no accessible azides remained following CuAAC to particle 3. The

labeling of only 20 chains on a particle that started with 180 potential initiation sites suggests that either polymer initiation is strongly inhibited by previously-initiated chains or that azide substitution and click cycloaddition reactions are inhibited by the presence of adjacent chains attached to the particle surface. Given the high efficiency of both azide nucleophilic attack and CuAAC coupling, we suspect that the former explanation is more likely. This issue will be studied further in upcoming experiments. We expect that the method of post-polymerization functionalization and bioconjugation described here will prove especially useful in attaching functional biomolecules such as cell targeting groups, cell penetrating peptides, or diagnostic agents.

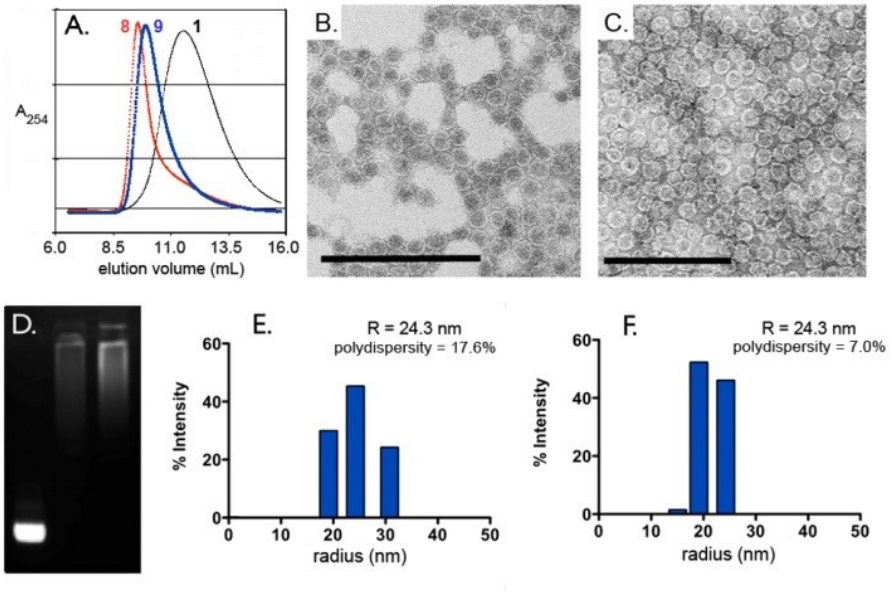

Figure 3.2: Characterization of Qβ-polymer particles. (A) Size-exclusion chromatographs. (B,C) TEM micrographs of poly(OEGMA) and poly(OEGMA-N_3) coated particles (8 and 9, respectively); scale bar = 200 nm. (D) Non-denaturing agarose gel stained with ethidium bromide: Lane 1= Qβ macroinitiator (5), Lane 2 = Qβ-poly(OEGMA) (8), Lane 3 = Qβ-poly(OEGMA-N_3) (9). (E,F) Dynamic light scattering histograms of 8 and 9, respectively.

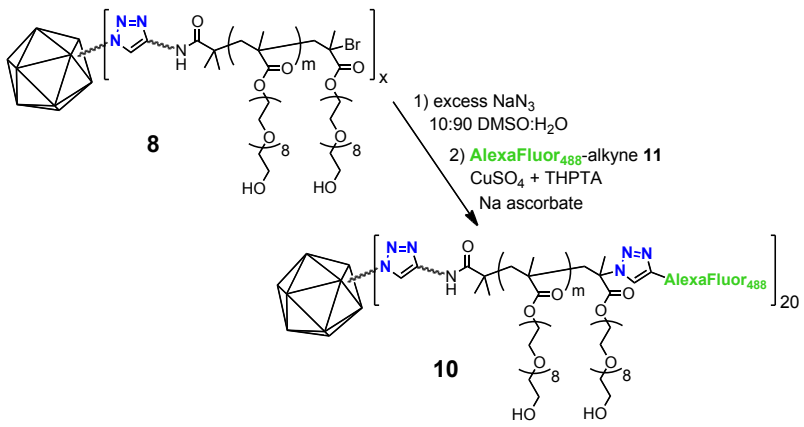

Figure 3.3: End labeling of Qβ-poly(OEGMA) (8). For the structure of 11, see Figure 3.4.

The azido-functionalized octa(ethylene glycol)-methacrylate (OEGMA-N_3, 7) also served as a competent monomer, allowing for a greater degree of post-polymerization functionalization while retaining PEG-like biocompatibility.[167] The polymerization of 7 proceeded in the same manner as 6 (Figure 3.1), yielding hybrid Qβ-poly(OEGMA-N_3) particle 9 with very similar properties to the poly(OEGMA)-coated 8: an approximate 10 nm increase in radius, narrow size distribution, and dramatically different electrophoretic mobility (Figure 3.2A,C,D, F).

To demonstrate the reactivity of poly(OEGMA-N_3) grafts, 9 was reacted with alkyne-substituted AlexaFluor488 dye 11 under CuAAC conditions (Figure 3.4A). Sucrose gradient centrifugation revealed an intensely colored green band, indicating a successful 'click' reaction (Figure 3.4B). The potential sensitivity of the molar absorptivity of these dyes to their molecular environment made quantification of the coupling efficiency at high dye loadings impossible by absorbance measurements. The same reaction was therefore performed with gadolinium complex 11, and the coupling result assayed by quantitation of Gd by inductively coupled plasma optical emission

spectroscopy (ICP-OES).[45] Loading values of 500-650 Gd complexes per particle were routinely found for reactions with different samples of 9.

Nanoparticles bearing Gd complexes have attracted substantial interest as magnetic resonance imaging agents due to benefits anticipated for their large size (slowing rotational relaxation rates) and high Gd loading capacities. Several variations using virus-like particles have been reported.[26; 36; 43; 44] We had earlier described the direct attachment of Gd(DOTA)-alkyne complex 12 to azide-derivatized particle 3, and the magnetic resonance behavior of the resulting conjugate 17.[45] Examination of the Qβ-polymer-Gd particle 15 found a similar relaxivity on a per Gd basis as 17 at two different Larmor frequencies (Table 3.1; approximately double the value of the Gd complex alone), suggesting that the polymer backbone does not impart additional conformational rigidity to the complexes or restrict access to water. The per particle relaxivity of 15 (7092 $mM^{-1}s^{-1}$), however, compares favorably to examples reported in the literature involving the covalent attachment of commercially available Gd reagents to virus particles.[26; 43; 44]

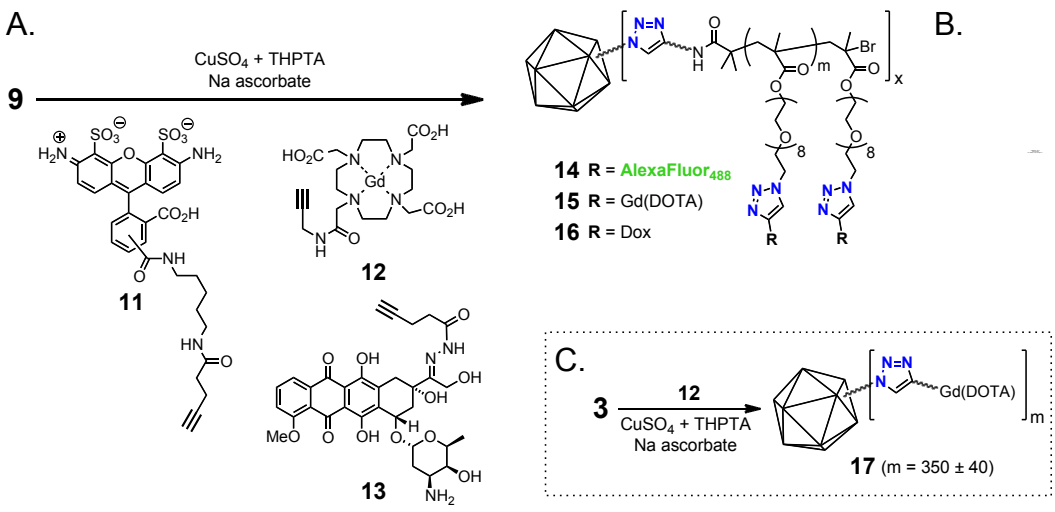

Figure 3.4: Conjugation to polymer side-chains. A) CuAAC reaction to append functionality to 9. B) UV illumination of sucrose gradient following CuAAC between 9 and 11 (upper band = unreacted 11, lower band = particle 14). C) Conjugation of Gd-DOTA complex 12 to azide-functionalized capsid 3.

		Relaxivity per Gd (per VLP) / $mM^{-1}s^{-1}$	
Sample	Gd/VLP	60 MHz	90 MHz
15	610	11.63 (7092)	10.12 (6174)
17	350	10.7 (3750)	11.64 (4075)

Table 3.1. T1 relaxivities for derivatized virus-like particles.

The multiple attachment points offered by the azide groups of polymer-decorated particle 9 may also be used to tether a releasable drug cargo. It has been reported that nanoparticles of approximately 25 nm radius are optimal for internalization via endocytotic pathways.[168] The relatively acidic environments of endosomal and lysosomal compartments (pH = 4.5-5.5) is most often used as the trigger for drug release, with

hydrazones being a popular motif.[169-171] Accordingly, we prepared a 'clickable' doxorubicin hydrazone 13 for conjugation to the Qβ-polyazide 9 (Figure 3.4A). Because of its poorer aqueous solubility than the Gd complex, fewer doxorubicin molecules were attached, an average of 150 per particle (approx. 3 wt-%), determined by measuring doxorubicin concentrations spectrophotometrically (280_{abs} = 490 nm) and comparing these to protein concentrations obtained by Bradford assay.[172] The resulting particles 16 remained intact with a narrow size distribution (DLS: radius = 22.7 nm, 14% polydispersity). This stands in contrast to the conjugation of 13 directly to particle 3, which led to degradation of the capsid structure and precipitation of the protein as occasionally happens with hydrophobic or polyaromatic molecules.

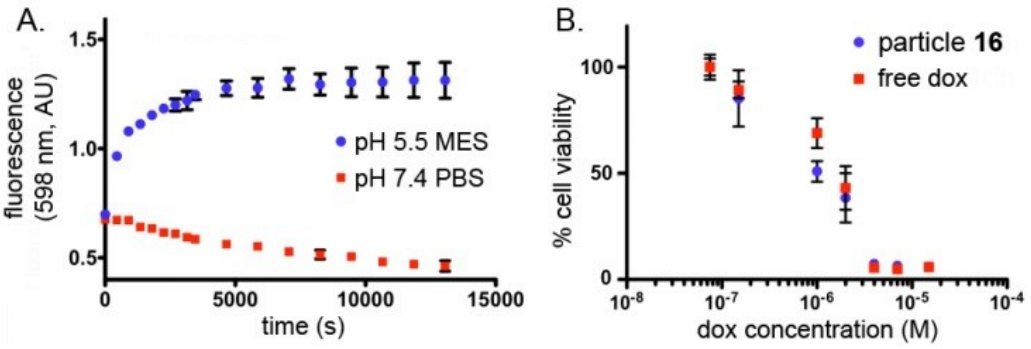

Figure 3.5: (A) *In vitro* release profile of doxorubicin from particle 16 at pH 7.4 and pH 5.5. (MES = 2(*N*-Morpholino)ethanesulfonic acid buffer; PBS = phosphate-buffered saline). B) MTT assay for cell viability after treatment with the indicated agents, see text.

The pH sensitivity of the Dox-conjugated particle 16 was assayed by fluorescence spectroscopy. The fluorescence of the Dox chromophores on 16 are known to be quenched at high local concentrations,[173] allowing us to monitor the release of the drug (λ_{ex} = 480 nm; λ_{em} = 598 nm) from the conjugate into solution at pH 7.4 and 5.5.[174; 175]

The maximum fluorescence was reached after approximately 2 h at pH 5.5, while no fluorescence increase was observed after 12 hours for the particles incubated at pH 7.4 (Figure 3.5A), consistent with the expected properties of the hydrazone linkage.

The pH-sensitive, doxorubicin-conjugated particle 16 was also found to be cytotoxic to HeLa cells, a cervical cancer cell line that is sensitive to treatment with doxorubicin.[176] Cells were incubated with varying concentrations of 16 or appropriate controls for 8 hours in pH 7 buffer (in which no cleavage of Dox from the particle occurs) and were assayed for cell viability the following day using the MTT assay. Polymer conjugate 16 exhibited a similar cytotoxicity profile to free doxorubicin (in terms of overall dox concentrations) under the same assay conditions (Figure 3.5B), indicating that the particles are internalized and release their payload to effect cell death. The cells showed no significant signs of toxicity when exposed to unloaded particles (9) at through the concentration range used with 16 (Appendix A).

Conclusion

In summary, we have shown that VLPs derived from the bacteriophage Qβ can serve as a platform for controlled radical polymerization to produce polymer-coated protein nanoparticles. The size and surface properties of Qβ can be significantly altered through ATRP, while still retaining the low polydispersities associated with VLPs. Furthermore, the polymer-coated particles are accessible to bioconjugation at both the chain termini and suitably derivatized polymer sidechains. The platform allows for both conjugation of small-molecule imaging agents and chemotherapeutics. Future studies will

focus on varying the nature and properties of the polymers produced by radial polymerization and on further exploration of this platform for development of targeted drug delivery and imaging agents.

.

CHAPTER 4

P22 VIRAL CAPSIDS AS NANOCOMPOSITE HIGH-RELAXIVITY MRI CONTRAST AGENTS

Contributions of Authors and Co-Authors

Manuscript in Chapter 4

Author: Shefah Qazi

Contributions: Designed and carried out the experiments and wrote the manuscript.

Co-author: Lars O. Liepold

Contributions: Designed and carried out the experiments and wrote the manuscript.

Co-author: Md Joynal Abedin

Contributions: Assisted in experimental design and synthesis of the P22 nanocomposite material.

Co-author: Ben Johnson

Contributions: Assisted in the initial characterization of the S39C mutant.

Co-author: Peter Prevelige

Contributions: Obtained funding and coordinated the project.

Co-author: Joseph A. Frank

Contributions: Assisted in NMR measurements.

Co-author: Trevor Douglas

Contributions: Obtained funding, coordinated the project, and assisted with the design of the experiments. Discussed the results and edited the manuscript at all stages.

Manuscript Information Page

Authors: Shefah Qazi, Lars O. Liepold, Md Joynal Abedin, Ben Johnson, Peter Prevelige, Joseph A. Frank, and Trevor Douglas
Journal: Molecular Pharmaceutics
Status of the manuscript:
____ Prepared for submission to a peer-reviewed journal
____ Officially submitted to a peer-reviewed journal
____ Accepted by a peer-reviewed journal
_X__ Published in a peer-reviewed journal

Publisher: American Chemical Society
Date of Submission: 2012
Issue in which manuscript appears: Volume 10, Issue 1, 11-17

CHAPTER 4

P22 VIRAL CAPSIDS AS NANOCOMPOSITE HIGH-RELAXIVITY MRI CONTRAST AGENTS

Published: *Molecular Pharmaceutics*, **2012**, 10 (1), 11-17.

Shefah Qazi,[†,§,ŧ] Lars O. Liepold,[†,§,ŧ] Md Joynal Abedin,[†,§] Ben Johnson, [†,§] Peter Prevelige,[‡] Joseph A. Frank, [ξ,€] and Trevor Douglas[†,§,*]

[†]Chemistry and Biochemistry Department, Montana State University, Bozeman, Montana, 59717, USA
[§]Center for Bio-Inspired Nanomaterials, Montana State University, Bozeman, Montana, 59717, USA
[‡]Department of Microbiology, University of Alabama at Birmingham, Birmingham, Alabama, 35294, USA
[ξ]Frank Laboratory, Radiology and Imaging Sciences, Clinical Center, National Institute of Health, Bethesda, Maryland, 20892, USA
[€]National Institute of Biomedical Imaging and Bioengineering, National Institute of Health, Bethesda, Maryland, 20892, USA
[ŧ]These authors contributed equally to this work

Abstract

Attachment of multiple chelated Gd^{3+} ions to the interior of bacteriophage P22 viral capsids afford nanoscale MRI contrast agents with extremely high relaxivity values. Highly fenestrated 'wiffleball' morphology is unique to P22 and assures water exchange between the environment and interior cavity of the capsid. The cavity of P22 'wiffleball' was functionalized with a branched oligomer comprising of multiple DTPA-Gd complexes resulting in an impressive payload of 1,900 Gd^{3+} ions inside each 64nm capsid. High relaxivities of $r_{1\ ionic}$ = 21.7 mM^{-1} sec^{-1} and $r_{1\ particle}$ = 41,300 mM^{-1} sec^{-1} at 298K, 0.65T (28MHz) are reported, with r_1/r_2 ratio of 0.80 and optimized rotational correlation time for this system. Specific design modifications are suggested for future improvements of viral capsid-based MRI contrast agents directed toward clinical translation.

Introduction

Magnetic resonance is often preferred over other imaging techniques because it employs harmless non-ionizing radiation to produce high contrast images that distinguish between pathological and normal tissues. Low sensitivity of this technique can be overcome by the use of contrast agents which provide additional contrast between tissues. Inherent properties of small molecule contrast agents can be significantly improved by slowing the rate of molecular tumbling through conjugation to a macromolecular platform.[35; 177] Various groups have explored dendrimers,[178] liposomes,[39; 179] protein cages,[36; 51] and more recently gold nanoparticles[180] as potential platforms for conjugation

of small molecule contrast agents. Here, we explore non-infectious bacteriophage P22 viral capsids as nanoscale MRI contrast agents because of their inherent multivalency and slow tumbling rates resulting from their large size.[25; 26; 43-45; 84; 106] Viral capsids are advantageous over other macromolecular contrast agents because they have two distinct surfaces available for independent conjugation of multiple imaging and targeting agents to the same scaffold. These agents can potentially be administered at low doses and still produce very high-contrast images, meeting an important criteria for next-generation diagnostic tools.

Virus capsids are dynamic, self-assembling systems that form highly symmetrical, multivalent, monodisperse structures and can be produced in heterologous expression systems in large quantities as genome-free capsids. These capsids are exceptionally robust, remaining stable at a range of temperatures, pH, and buffers, hence can be readily modified both genetically and chemically. Plant viruses and bacteriophages are particularly desirable in developing nanocomposites for applications in biomedicine because they are less likely to be pathogenic in humans.[149] Some virus-based systems that have been used for encapsulation of imaging agents include cowpea chlorotic mottle virus (CCMV),[44] cowpea mosaic virus (CPMV),[45] bacteriophages Qβ and MS2.[25; 26; 43] P22 bacteriophage, approximately double in size, allows for a much greater payload of imaging agent per capsid. It can undergo transformation to a 'wiffleball' form, creating a fenestrated capsid structure which allows small molecules to freely diffuse between the external medium and the capsid interior.[74; 75; 78] The substantial size of the interior cavity

can be more efficiently utilized through incorporation of an oligomer network coupled to multiple small molecule imaging agents.

Here, we explore the genetically modified P22 capsid in its 'wiffleball' architecture with site-specific thiol reactive residues at the 118 position as a T_1 Gd-based MRI contrast agent. Azide-alkyne click chemistry was used to synthesize a branched oligomeric network conjugated to DTPA-Gd complexes under optimal conditions[45] and the influence of individual factors that affect the overall relaxivity behavior of the viral capsid nanocomposite was examined.[181] The P22 nanocomposite has a higher loading capacity of imaging agents than previously described systems and as a result provides an extremely high relaxivity per particle.

Results and Discussion

In this work, we have utilized the P22 capsid as a synthetic template for the development of Gd-based T_1 MRI contrast agents because of its large interior cavity and our ability to take advantage of site specific modifications to the capsid. When bacteriophage P22, which naturally infects *Salmonella typhimurium*, is recombinantly expressed in *E. coli* it self-assembles into a 58nm procapsid structure from 420 identical subunits of coat protein and between 60 and 300 copies of an internal scaffold protein (Figure 4.1A).[74; 75] The capsid can be induced to undergo a series of structurally characterized morphological transformations from the procapsid (PC) form.[78; 79] Upon heating of P22 procapsid to 75°C, the capsid expands to 64nm causing the capsid wall to become thinner and selectively release all twelve of its icosahedral pentamers to produce

the wiffleball morphology (WB), creating a hollow nanocontainer with 10nm pores (Figure 4.1B) at the 5-fold axes.[76; 83] The wiffleball form is used in this study due to its near double increase in volume as compared to the PC form, and because the highly robust and porous structure allows for free molecular access across the protein shell. A single-point mutation in the wild-type P22 coat protein, K118C, was utilized for site-specific modification with a branched oligomer using azide-alkyne click chemistry (AACC). The 118C mutation introduces an addressable thiol in each of the 420 subunits of the P22 capsid and high-resolution structural models of the P22 capsid suggest that this site is mostly exposed to the internal surface (Figure 4.1C).[76]

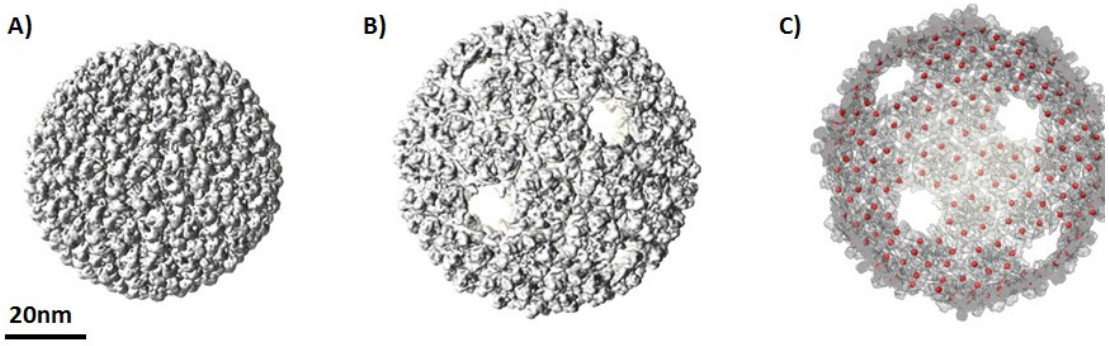

Figure 4.1: Cryo-EM reconstructions A) P22 PC procapsid (*pdb 3IYI),*[29] B) P22 WB wiffleball (*pdb 3IYH),*[29] C) P22 WB half cutaway view of capsid interior with residue 118 highlighted as red spheres.

Azide-alkyne click chemistry (AACC) is a well-established orthogonal oligomerization technique compatible with protein architectures. The reaction takes place between azide and alkyne moieties in the presence of a Cu (I) catalyst and an appropriate ligand to form a 1,4-substituted triazole. The internal oligomerization of P22 wiffleball was accomplished using previously described methods.[51; 105] Reaction was

initiated from the 118C mutation site after reaction of the thiol with N-propargyl bromoalkyne to create P22-alkyne (Figure 4.2A). 2-azido-1-azidomethyl-ethylamine (DAA) was coupled to 2-(4-isothiocyanatobenzyl)-diethylene-triamine pentaacetic acid gadolinium (*p*-SCN-Bn-DTPA-Gd) to create the bifunctional monomer (DAA-DTPA-Gd) (Figure 4.2B) used in the oligomerization reaction. A branched oligomeric structure was synthesized by reaction of DAA-DTPA-Gd with the P22-alkyne, followed by reaction with tripropargyl amine (Figure 4.2C) in a stepwise series of reactions to produce P22-AACC-Gd, until theoretical incorporation of seven DAA-DTPA-Gd moieties per subunit was achieved (Figure 4.2, Figure 4.3).

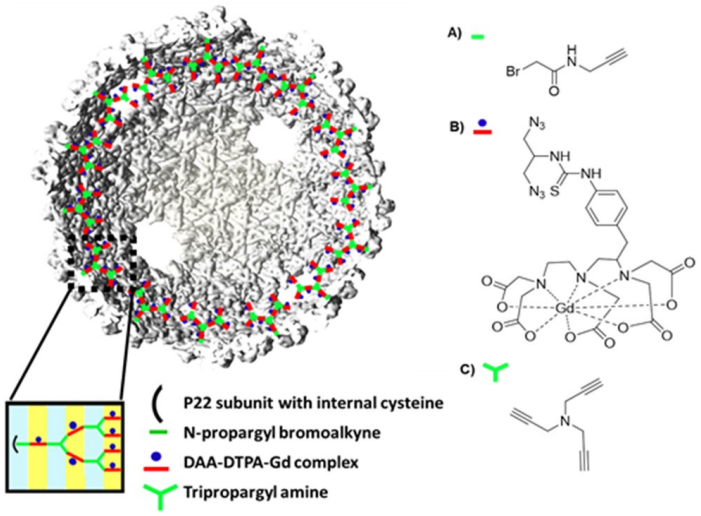

Figure 4.2: Theoretical incorporation of seven DAA-DTPA-Gd complexes per subunit of P22 WB. Monomers used for synthesis of branched oligomer A) N-propargyl bromoalkyne, B) 2-azido-1-azidomethyl-ethylamine coupled to 2-(4-isothiocyanatobenzyl)-diethylene-triamine pentaacetic acid gadolinium (DAA-DTPA-Gd complex), C) tripropargyl amine.

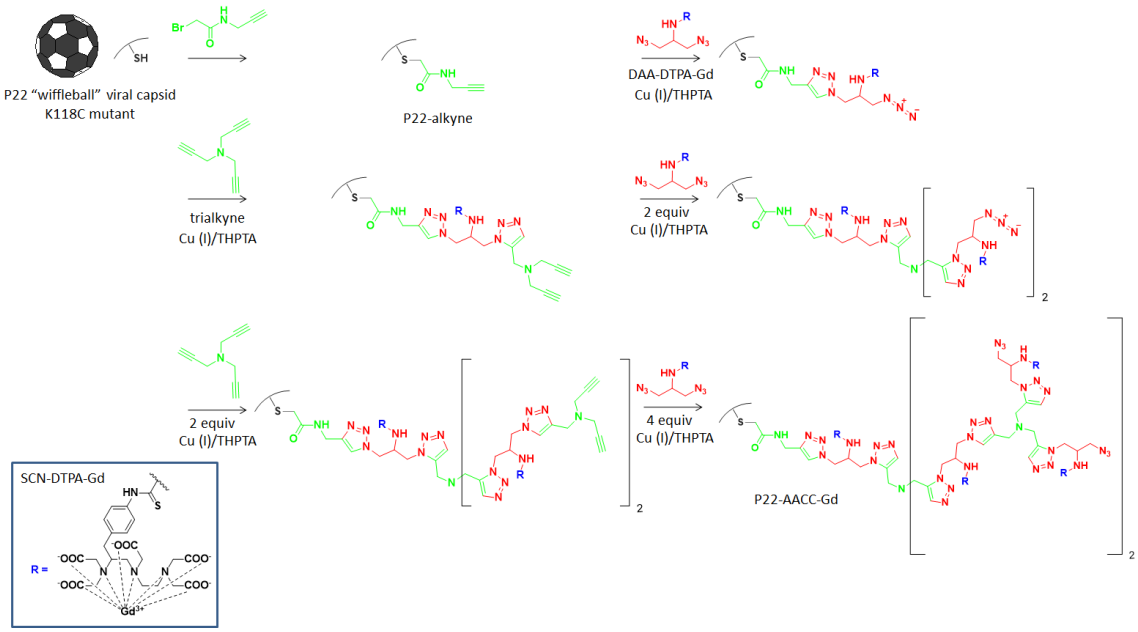

Figure 4.3: Overall synthetic scheme for generating P22-AACC-Gd with theoretical incorporation of seven DAA-Gd per capsid. Detailed experimental procedure can be found in previous reports.[7]

Physical characterization of the resulting nanocomposite suggested no increase in overall particle size of P22-AACC-Gd compared to P22 WB with a relative increase in mass, indicating that oligomer growth was confined to the interior of the capsid. P22-AACC-Gd was purified by size exclusion chromatography and the elution time was identical to that of the P22 WB indicating no change in the overall particle diameter (Figure 4.4C). Measurement of the particle sizes from transmission electron microscopy (Figure 4.4A) revealed mean diameters for P22 WB and P22-AACC-Gd of 57.4 ± 2.5 nm and 61.6 ± 2.3 nm, respectively. This was further confirmed by dynamic light scattering, which revealed a hydrodynamic diameter of 64.1 ± 7.1nm for P22 WB and 63.1 ± 5.9nm for P22-AACC-Gd (Figure 4.4B). Multi-angle light scattering, coupled to HPLC size exclusion chromatography, also revealed that the size of the P22 capsid remained

essentially unchanged for P22 WB and P22-AACC-Gd with an average radius of gyration of 29.7 ± 0.06nm and 29.6 ± 0.12nm, respectively (Figure 4.4C). Analysis of the MALS data additionally suggested an increase in mass for P22-AACC-Gd over the P22 WB, although absolute quantification is not possible because the refractive index increment (*dn/dc*) for the oligomer is not known. Further evidence of the mass increase associated with the oligomer growth was observed by sodium dodecyl sulfate-polyacrylamide gel electrophoresis (SDS-PAGE), which shows a shift in mobility of the subunit towards higher Mw (Appendix B, Figure B1) for P22-AACC-Gd, with no unmodified coat protein subunits visible. High Mw species visible in the SDS-PAGE gel are consistent with some degree of inter-subunit cross-linking between neighboring tripropargyl amine and DAA-DTPA-Gd 'click' monomers. Together these data suggest that modification of the capsid is fairly uniform and is confined primarily to the interior of the P22 capsid.

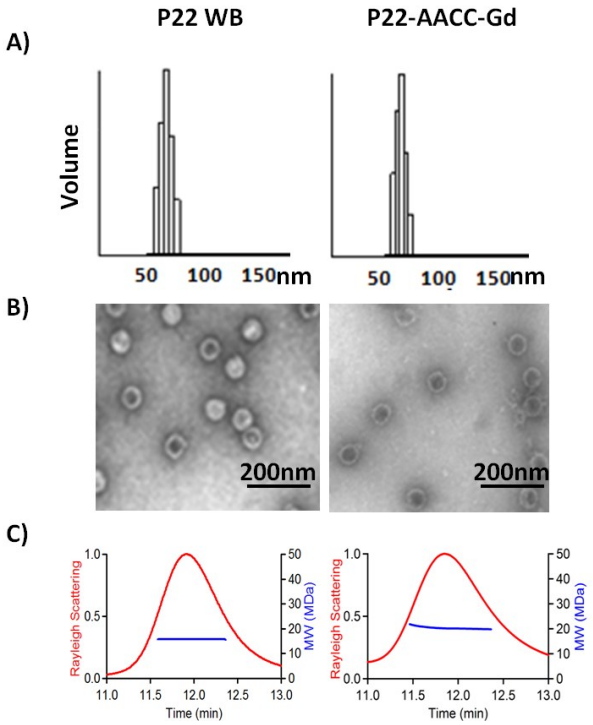

Figure 4.4: Similar capsid size before and after modification is reported using three different methods. A) DLS (average diameter): P22 WB = 64.1 $\pm$ 7.1nm, P22-AACC-Gd = 63.1 $\pm$ 5.9nm. B) TEM (average diameter): P22 WB = 57.4 $\pm$ 2.5nm, P22-AACC-Gd = 61.6 $\pm$ 2.3nm. C) SEC-MALS (average radius): P22 WB = 29.7 $\pm$ 0.06nm, P22-AACC-Gd = 29.8 $\pm$ 0.12nm. An increase in molecular weight after modification (blue line) is indicative of oligomer growth within P22 cavity.

Relaxivity measurements of P22-AACC-Gd were taken over a wide range of field strengths between 0.1T-1.4T (Figure 4.5). For $r_{1\ ionic}$ measurements, a peak centered at 0.6-0.8T was observed (Figure 4.5A), which is characteristic of chelator-Gd complexes attached to macromolecular systems tumbling slowly in solution.[35; 36; 44; 115; 181] Maximum relaxivity occurred at 0.65T, with an ionic relaxivity of $r_{1\ ionic}$ = 21.7 mM^{-1} s^{-1}, 6-fold greater than free DTPA-Gd,[182] and an exceedingly large per particle relaxivity, $r_{1\ particle}$ = 41,300 mM^{-1} s^{-1} with considerable loading of 1,900 Gd per capsid. The r_2 profile (Figure 4.5B) is also consistent with previous findings for large macromolecular systems, with r_2

$_{ionic}$ = 27.2 mM^{-1} s^{-1} and $r_{2\ particle}$ = 51,800 mM^{-1} s^{-1}. The absolute protein concentration of the modified P22 capsid was determined using standard amino acid analysis techniques and relaxivity measurements were used to determine Gd concentration.

Nuclear magnetic resonance dispersion (NMRD) profiles for P22-AACC-Gd were attained from fitting relaxivity versus field strength to the Solomon-Bloembergen-Morgan (SBM) analytical model for relaxivity.[115; 183; 184] The fits were influenced by five parameters: the number of Gd-bound water molecules (q), the mean residence lifetime for Gd-bound water (τ_M), the rotational correlation time (τ_R), the magnitude of the zero field splitting interaction (Δ), and the correlation time for transient zero field splitting fluctuation (τ_V). A total of four fits were explored, with all fitting schemes resulting in similar values for q, τ_R and τ_M. The best fit resulted in q = 0.92, as expected for DTPA-Gd complexes (q =1).[35] A rotational correlation time of τ_R = 160ns agrees well with reported values for bioconjugation of DTPA-Gd complexes to macromolecular systems, which lead to high ionic relaxivities due to slower tumbling of the nanocomposite as compared to free DTPA-Gd.[36; 86] A value for mean residence lifetime for water of τ_M = 530 ns is similar to Gd-DTPA alone (τ_M = 240ns),[36] which suggests, overall, incorporating DTPA-Gd complexes within the P22 cavity does not restrict water access. However, observation of a slight increase in τ_M could be explained due to obstruction of water access in the presence of the bulky oligomer network surrounding the Gd^{3+} ions.

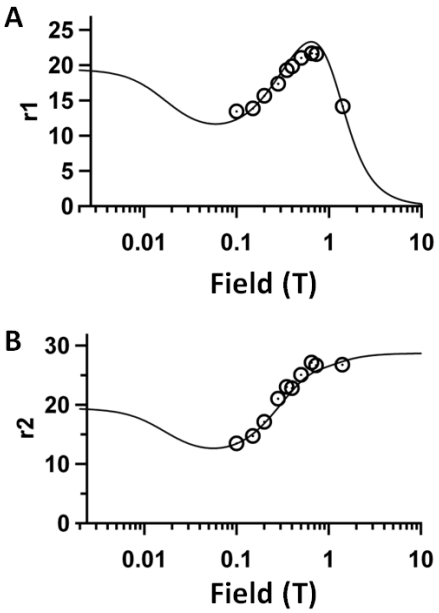

Figure 4.5: Nuclear magnetic dispersion profiles (NMRD) for P22-AACC-Gd, showing relaxivity as a function of field strength. The black circles indicate experimental data points which were fit to an SBM equation (Eqn. S1) where r_1 and r_2 were fit simultaneously (Table S1). A) $r_{1\ ionic}$ NMRD profile B) $r_{2\ ionic}$ NMRD profile.

MRI contrast agents with high ratios between the longitudinal and transverse relaxivities (r_1/r_2) ranging from 0.5-0.9 are defined as optimally performing Gd-based T_1 contrast agents.[39; 185] For P22-AACC-Gd, the r_1/r_2 ratios range from 0.80-0.53 for magnetic fields 0.65T–1.4T, with the highest ratio of 0.82 at 0.73T. This compelled us to explore the effects of mean residence lifetime (τ_M) and rotational correlation time (τ_R) on relaxivity at this field strength. We plotted relaxivity ($r_{1\ ionic}$) versus field strength using three different values for τ_M and τ_R (Figure 4.6) - the experimentally determined value (green), a value above the experimental (blue), and a value below the experimental (red). This allowed us to visualize how relaxivity at 0.73T (max. peak height) is affected by altering τ_M (Figure 4.6a) and τ_R (Figure 4.6b). It becomes apparent that while τ_R has been optimized for this system the τ_M can be further improved. The mean residence lifetime of

water, τ_M, could be altered by conjugating a different small molecule chelator-Gd complex[86] to the P22-oligomer composite.

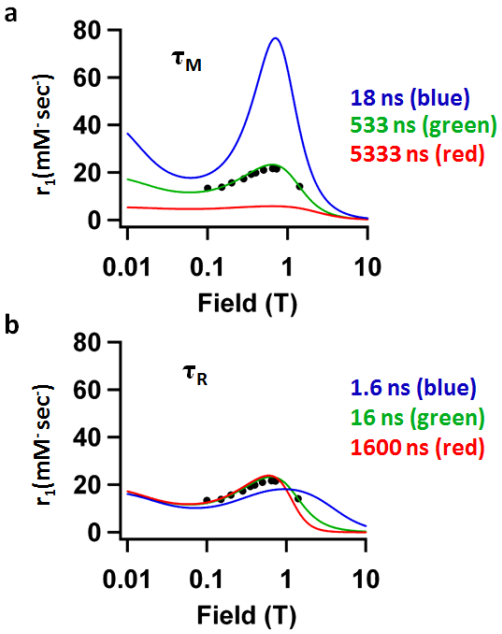

Figure 4.6: Plot of P22-AACC-Gd showing r_1 vs. field strength for three different values of a) τ_M – 18ns (blue), 533ns (green), 5333ns (red) and b) τ_R – 1.6ns (blue), 16ns (green), 1600ns (red). The black dots represent experimental values of r_1 for P22-AACC-Gd where the green line represents the best fit to the data. The plot illustrates that τ_R is optimized for P22-AACC-Gd at 0.73T (max. peak height), while τ_M could be further improved for this system.

In order for virus capsid-based MRI contrast agents to be clinically translatable, it is necessary to evaluate their relaxivity performance at higher field strengths. Using P22-AACC-Gd as a model system, its relaxivity (r_1 and r_1/r_2) performance was assessed at a range of field strengths for a range of τ_M values (Appendix B, Figure B2) using contour plots. Particular attention was paid to relaxivity values at 3T, another field strength commonly used clinically. We chose to evaluate the system at three different τ_R values for

τ_M =533ns (the established τ_M for our system). For τ_R = 0.1ns (Appendix B, Figure B2c), the τ_R value for free DTPA-Gd complexes,[186] we see low $r_{1\ ionic}$ of 3.2 mM^{-1} s^{-1} and high r_1/r_2 = 0.87. At a value of τ_R = 16ns (Appendix B, Figure B2c), the established τ_R for our system, $r_{1\ ionic}$ of 3.5 mM^{-1} s^{-1} is similar in value to free DTPA-Gd, while r_1/r_2 = 0.12 is lower than the optimal range. Reducing τ_R from 16ns to 1ns (Appendix B, Figure B2b) suggests an improvement in P22-AACC-Gd performance at 3T, as r_1 is improved from 3.5 mM^{-1} s^{-1} to 13.0 mM^{-1} s^{-1} and the r_1/r_2 ratio from 0.12 to 0.78. Lower rotational correlation times (τ_R) may be attained through conjugation of chelator-Gd complexes to a more flexible polymer. Utilizing an alternate polymer synthesis technique that creates a linear polymer instead of a branched polymer might result in greater degrees of freedom in terms of local motion of chelator-Gd complexes and will be explored in future work.

Conclusion

In summary, we have synthesized a branched oligomer conjugated to multiple DTPA-Gd complexes inside of P22 'wiffleball' viral capsids. This resulted in one of the highest reported particle relaxivities for viral-capsid based systems and a significant improvement in ionic relaxivity over free DTPA-Gd. The rotational correlation time has been optimized for this system, while conjugation of different chelator-Gd complexes has been suggested for improvement of the mean residence lifetime. Better performance of this system at high field strengths has been suggested via conjugation of DTPA-Gd complexes to more flexible polymer networks inside the viral capsid, or alternatively DTPA-Gd may be attached to polymer via a more flexible linker.[180] Current efforts are

focused on alternate polymerization techniques and addition of targeting ligands on the external surfaces of these viral nanoparticles.

Experimental

All materials were analytical grade and purchased from either Sigma-Aldrich or Fisher Scientific and used as received unless otherwise noted. All water was deionized using a NANOpure water purification system. Dynamic light scattering measurements were taken on a 90Plus particle size analyzer (Brookhaven). The synthesis of N-propargyl bromoacetamide and 2-azido-1-azidomethyl-ethylamine have been reported previously.[51] The *p*-SCN-Bn-DTPA was purchased from Macrocyclics.

Mutagenesis.

The P22 (K118C) point mutation was made using established polymerase chain reaction protocols (Qiagen) using pET-3a based plasmids encoding genes for scaffolding and coat protein. The amplified DNA was transformed into $CaCl_2$ treated competent *E. coli* strain BL21 (DE) and selected for ampicillin resistance.[187]

Protein Purification.

Transformed BL21 (DE) *E.coli* was grown in 1L cultures inoculated with 1 mL starter culture (37ºC, 220rpm). After 2 hours (OD_{600} = 0.6), the cultures were induced with 1mM IPTG and grown for 4 more hours. Cells were harvested by centrifugation at 3700g for 20 min. The cells were resuspended in PBS pH 7.6 and were incubated with DNase, RNase, and lysozyme (all Sigma-Aldrich) for 30 minutes at room temperature.

Cells were lysed further by sonication on ice (Branson Sonifier 250, Danbury, CT, power 4, duty cycle 50%, 3 × 5 min with 3 min intervals). Bacterial cell debris was removed via centrifugation at 12 000g for 45 min. The supernatant was then loaded on a 35% sucrose cushion and centrifuged at 48,000 rpm for 50 min in an ultra centrifuge (50.2Ti ultra centrifuge rotor). The resulting virus pellet was resuspended in PBS pH 7.0 and dialyzed to remove sucrose. The P22 empty shells (ES) were prepared by repeated extraction of scaffolding protein with 0.5M guanidine-HCl.[75] Purified ES were heated at 75ºC for 20 min to obtain P22 wiffleball (WB).[83] P22 WBs were further purified by 5-20% sucrose gradient centrifugation and dialyzed against buffer to remove residual sucrose. Each individual capsid form was routinely characterized using SDS-PAGE, native agarose gels, transmission electron microscopy (TEM, Leo 912 AB), and dynamic light scattering (DLS, Brookhaven 90Plus, Brookhaven, NY).[188] The protein concentration was determined by absorbance at 280nm using the extinction coefficient (44,920 M^{-1} cm^{-1}).

Synthesis of *p*-SCN-Bn-DTPA-Gd.

2-(4-isothiocyanatobenzyl)-diethylenetriaminepentaacetic acid (*p*-SCN-Bn-DTPA) (250mg, 0.385mmol, 128mM) was treated with gadolinium (III) chloride (157mg, 0.424mmol, 141mM, 1.1eqv) in water. The mixture was stirred for 3 hrs at room temperature, followed by removal of solvent by lyophilization under reduced pressure. The yield was quantitative and the slightly yellowish product was characterized by LC-MS. The product was used without further purification. LC-MS: A cluster of isotopic peaks centered at 696.23(±1,2,3,4) was found for SCN-Bn-DTPA-Gd ($C_{25}H_{32}N_{11}O_{10}SGd$). Theoretical value for $C_{22}H_{25}N_4O_{10}SGd$ is centered at 696.116.

Synthesis of Diazidopropylamine Conjugated to *p*-SCN-Bn-DTPA-Gd (DAA-DTPA-Gd).

p-SCN-Bn-DTPA (322mg, 0.462mmol, 154mM) was dissolved in water in a small round bottom flask. The pH of the solution was raised slowly to 8.5 with dilute NaOH solution. While stirring, 2-azido-1-azidomethyl-ethylamine (131mg, 0.924mmol, 308mM, 2.0 eqv) was added slowly in the reaction mixture. The mixture was stirred overnight at room temperature. Lyophilization of the mixture under reduced pressure yielded a slightly yellowish solid product. Excess 2-azido-1-azidomethyl-ethylamine was removed by washing the crude product several times with methylene chloride. The yield was quantitative and the product was characterized by LC-MS. This product was used without further purification for bio-conjugation with protein cage. LC-MS: A cluster of isotopic peaks centered at 837.145 (±1,2,3,4,5) was found for DAA-DTPA-Gd ($C_{25}H_{32}N_{11}O_{10}SGd$). Theoretical value for $C_{25}H_{32}N_{11}O_{10}SGd$ is centered at 837.138.

Synthesis of P22-AACC-Gd.

Unless otherwise noted, all reaction steps were done in HEPES buffer, pH 7.6. Each reaction product was purified by dialysis with molecular porous membrane (MWCO 12-14K). Concentrations were determined by UV-Vis spectrometry by OD_{280}. Oligomer was incorporated in a step-wise fashion to yield P22-AACC-Gd. Briefly, in pH 6.5 HEPES buffer, P22 (K118C) WB (83.3mg, 1.79umol, 1.79mM) was reacted with N-propargyl bromoacetamide (3.6mg, 17.9umol, 17.9mM, 10 eqv) by stirring 1h at room temperature, followed by incubation at 4°C overnight. The P22-alkyne was characterized by LC-MS. LC-MS: M+H 46693(found), M+H 46692(calcd).

The P22-alkyne (75mg, 1.61μmol, 215mM) was reacted with DAA-DTPA-Gd (13.5mg, 16.1μmol, 2.15M, 10 eqv) through Cu-catalyzed azide-alkyne coupling reaction.[103] Briefly, a 1:5 mixture of $CuSO_4$ and THPTA ligand[105] was prepared and added to the reaction mixture to achieve a final concentration of 0.90mM Cu (I) and 4.5mM THPTA ligand. This was followed by addition of sodium ascorbate and amino guanidine, both with final concentrations of 10.15mM. The reaction vial was purged with N_2, sealed and stirred for 1h at room temperature and incubated overnight with stirring at 4 °C. The reaction mixture was treated with 12-fold excess of 0.5M EDTA, pH 8.0 to chelate Cu ions associated with the P22 capsid derivatives. The resulting product was reacted with tripropargyl amine and DAA-DTPA-Gd in a step-wise fashion for a total of four more reactions under similar conditions as described above[51], until a theoretical yield of seven DAA-DPTA-Gd were incorporated per subunit of P22 wiffleball. The intact P22-AACC-Gd overall recovery was 44.4% (37mg, 0.80mol, 8.0mM).

Multi-Angle Light Scattering.

P22 and P22-AACC-Gd were injected using an Agilent 1200 autosampler with PBS pH 7.3 and 200ppm azide at 0.7ml/min as the running buffer. The buffer was degassed using an inline degasser. Samples were run over a WTC-100S5G guard column (Wyatt Technology Corporation) and a WTC-100S5 SEC column designed specifically for MALS (Wyatt Technology Corporation). The eluant was monitored using an in-line UV-Vis detector on the Agilent system as well as a Dawn Heleos 8 MALS detector and an Optilab T-rex RI detector (Wyatt Technology Corporation). All data were analyzed

using ASTRA software from Wyatt. Samples were stored in the autosampler at room temperature, and the sample chamber in the RI detector was held at 25°C to reduce thermal drift. Molecular weights were determined from MALS and RI signals using the ASTRA software and dn/dc values of 0.185 was used for all proteins.

Transmission Electron Microscopy.

P22 and P22-AACC-Gd were imaged by transmission electron microscopy (Leo 912 AB) by negatively staining the sample with 2% uranyl acetate on formvar carbon coated grids. Average diameters were determined from measurements of 10 particles for each sample.

Denaturing Gel Assay.

P22 and P22-AACC-Gd were analyzed using SDS-PAGE on 10-20% gradient Tris-glycine gels (Lonza).

Nuclear Magnetic Resonance Dispersion (NMRD).

T_1 and T_2 measurements were carried out on a variable field relaxometer. The longitudinal (T_1) and transverse (T_2) relaxation rate constants of P22-AACC-Gd were measured using an inversion-recovery and Carr-Purcell-Meiboom-Gill (CPMG) pulse sequence with 32 incremental tau values, respectively.[44] The measurements were collected for a range of Larmor frequencies between 2–62 MHz (0.05–1.5T) at 298K. Values for r_1, r_2, q, τ_M, and τ_R were determined by fitting the raw data to a Solomon-Bloembergen-Morgan (SBM) analytical model for relaxivity as previously described.[36] All plots were produced using Mathcad 14.0.

Gadolinium Concentration.

The gadolinium (Gd) concentration of P22-AACC-Gd was analyzed by NMR (300MHz Bruker NMR) through adaptation of a published procedure.[26; 189] Sample was prepared by digesting P22-AACC-Gd overnight in 30% HNO_3 at room temperature. A standard curve using $GdCl_3$ ranging from 0.3μM to 1968.3μM was used for quantification. The Gd concentration was further verified by inductively couple plasma mass spectrometry ICP-MS at Energy Labs (Billings, MT).

Protein Concentration.

Modification to standard procedure for amino acid analysis was used.[190] Briefly, P22-AACC-Gd was spun down in a rotary evaporator until sample was completely dry. A solution of 6N HCl containing 1% phenol was added to the sample. The sample was digested under anaerobic conditions for 18 hours at 110ºC, 20 psi. The acid from the digested sample was removed by a rotary evaporator. The sample was resuspended in H_2O and 1% formic acid. Standards of amino acids were prepared in 6N HCl ranging from 1.0μM to 2500μM. ESI-Q-TOF mass spectrometry (Q-TOF Premier, Waters) interfaced to a Waters UPLC was used to determine presence of most abundant amino acids. A standard curve was made using best fit amino acid data. The peak intensities correlating to amino acids in P22-AACC-Gd were fit to the standard curve to extrapolate amino acid concentrations, which were used to calculate the protein concentration based on the amino acid sequence of P22.

CHAPTER 5

USING THE INTERIOR CAVITY OF THE P22 CAPSID FOR SITE-SPECIFIC INITIATION OF ATOM TRANSFER RADICAL POLYMERIZATION WITH HIGH DENSITY CARGO LOADING

Contributions of Authors and Co-Authors

Manuscript in Chapter 5

Radical Polymerization with High-Density Cargo Loading

Author: Janice Lucon

Contributions: Designed and carried out the experiments and wrote the manuscript.

Co-author: Shefah Qazi

Contributions: Characterized the samples by NMR and analyzed the relaxivity data.

Co-author: Masaki Uchida

Contributions: Assisted in experimental design and the initial characterization of the S39C mutant.

Co-author: Gregory J. Bedwell

Contributions: Characterized the samples by analytical ultracentrifugation.

Co-author: Ben LaFrance

Contributions: Assisted in the initial characterization of the S39C mutant.

Co-author: Peter E. Prevelige, Jr

Contributions: Obtained funding and coordinated the project.

Co-author: Trevor Douglas

Contributions: Obtained funding, coordinated the project, and assisted with the design of the experiments. Discussed the results and edited the manuscript at all stages.

Manuscript Information Page

Authors: Janice Lucon, Shefah Qazi, Masaki Uchida, Gregory J. Bedwell, Ben LaFrance, Peter E. Prevelige, Jr, and Trevor Douglas
Journal: Nature Chemistry
Status of the manuscript:
____ Prepared for submission to a peer-reviewed journal
____ Officially submitted to a peer-reviewed journal
____ Accepted by a peer-reviewed journal
_X__ Published in a peer-reviewed journal

Publisher: Nature Publishing Group
Date of Submission: 2012
Issue in which manuscript appears: Volume 4, 781-788, Cover

CHAPTER 5

USING THE INTERIOR CAVITY OF THE P22 CAPSID FOR SITE-SPECIFIC INITIATION OF ATOM TRANSFER RADICAL POLYMERIZATION WITH HIGH DENSITY CARGO LOADING

Published: *Nature Chemistry*, **2012**, 4, 781-788 (Cover).

Janice Lucon[1,2], Shefah Qazi[1,2], Masaki Uchida[1,2], Gregory J. Bedwell[3], Ben LaFrance[1,2], Peter E. Prevelige, Jr.[3], and Trevor Douglas[1,2]

[1] Chemistry and Biochemistry Department, Montana State University, Bozeman, Montana, 59717
[2] Center for Bio-Inspired Nanomaterials, Montana State University, Bozeman, Montana, 59717
[3] Department of Microbiology, University of Alabama at Birmingham, Birmingham, Alabama, 35294

Abstract

Virus-like particles (VLPs) have emerged as important and versatile architectures for chemical manipulation in the development of functional hybrid nanostructures. Here we demonstrate a successful site -selective initiation of atom transfer radical polymerization reactions to form an addressable polymer constrained within the interior cavity of a VLP. Potentially, This protein–polymer hybrid of P22 and cross-linked poly(2-aminoethyl methacrylate) could be useful as a new high-density delivery vehicle for the encapsulation and delivery of small -molecule cargos. In particular, the encapsulated polymer can act as a scaffold for the attachment of small functional molecules, such as fluorescein dye or the magnetic resonance imaging (MRI) contrast agent Gd-diethylenetriaminepentacetate, through reactions with its pendant primary amine groups. Using this approach, a significant increase in the labelling density of the VLP, compared to that of previous modifications of VLPs, can be achieved. These results highlight the use of multimeric protein–polymer conjugates for their potential utility in the development of VLP-based MRI contrast agents with the possibility of loading other cargos.

Introduction

The use of protein–polymer composite materials for medical and materials applications is a growing field that aims to take advantage of the exquisite monodispersity and bioactivity of biomolecules and also impart new material properties via polymer conjugation. When a responsive polymer is selected, new thermo-, light- and

pH -sensitive macromolecular materials can be produced to control more fully the activity and phase solubility of the biomolecule.[191; 192] By adding a specific polymer to the biomolecule, the composite material may exhibit improved retention, lowered immunogenicity and increased bioavailability.[193-195] To attain the desired final material properties, careful selection of both the protein and the polymer components is essential. Much of this work focused on the site-specific conjugation of polymers to monomeric proteins, but when more complex multimeric biomolecules are employed, not only is the polymer location on the primary sequence of interest, but also the spatial relationship between the polymer and the overall protein architecture becomes increasingly important.

In particular, the use of virus-like particle (VLP) proteins, which are a special class of multimeric proteins that form symmetric protein shells surrounding an empty interior space, relies on two distinct environments that can be modified, either the exposed exterior or the confined interior. For the exterior surface, polymer formation or attachment was employed as a method to append molecules of interest designed to alter VLP solubility, increase stability or introduce new functionalities.[106; 196] Electrostatic interactions were used in several systems to package existing polymers or guide capsid assembly around polymers and polymer–nanoparticle composites to provide a charge - dependent occupation of the interior space.[1; 197-201] Synthesis of polymers in the interior space was limited to small protein cages, which were employed as a synthesis chamber for an untethered oligomer or for the development of an anchored addressable network.[51; 202]

We reported previously the use azide–alkyne ‘click’ chemistry to construct an anchored polymer network inside a small protein -cage architecture.[36; 51; 107] In this stepwise synthesis approach, polymer growth was directed to the protein -cage interior, which resulted in a protein-confined hyperbranched polymer. The protein shell acted as a barrier that limited the polymer size and left only the protein exterior exposed to the bulk solution. By labelling the resulting protein–polymer construct with a Gd-based magnetic resonance imaging (MRI) contrast agent, an enhanced magnetic resonance contrast agent was obtained, which highlights the utility of using the interior space to maximize cargo loading.[36] While this method is effective, the stepwise nature of the polymerization reaction makes the process onerous for larger constrained polymer syntheses. A preferable alternative route to achieve an anchored addressable polymer is to proceed via a continuous polymerization of simple monomers from an easily modified initiator. Of the several suitable continuous biomolecule-anchored polymerization methods, we chose to use atom -transfer radical polymerization (ATRP) as it is particularly suited to an improved formation of polymer inside a protein cage. This method is not only rapid, but also results in products with relatively low polydispersity in bulk solutions and is promiscuous with respect to the range of monomers that can be used. Also, the simplicity of the ATRP initiator means that it can be attached readily to the protein cage in a site-specific manner, and thereby we can control the site of polymer initiation. Thus, by combining ATRP with a container-like protein, the formation of a polymer scaffold constrained to the interior of a VLP architecture can be afforded in a single short reaction.

Here we report the use of ATRP to make addressable polymer networks within the confines of the bacteriophage P22 -based VLP (Figure 5.1). The 2-aminoethyl methacrylate (AEMA) monomer was selected because the primary amine-rich polymer synthesized within the P22 capsid could be modified subsequently with the small molecules of interest, which resulted in very high -density loadings of the capsid. The use of the AEMA network as a scaffold was demonstrated through the attachment of either fluorescein isothiocyanate (FITC) or Gd-DTPA-NCS (DTPA = diethylenetriaminepentacetate). Using this method, we can achieve a substantial increase in the degree of labeling per VLP compared to that given in previous reports, which demonstrates the potential capacity of the capsid interior for directed cargo loading.

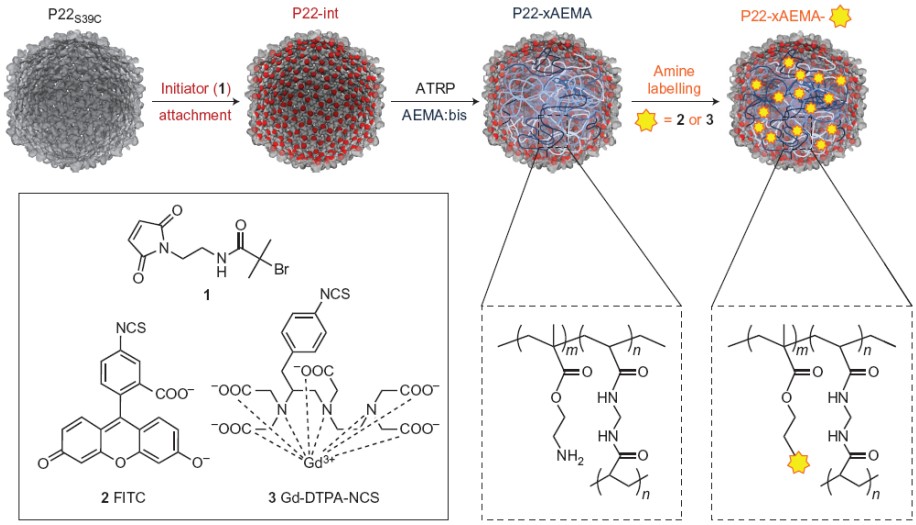

Figure 5.1: Schematic of the internally initiated ATRP polymerization within the P22 VLP. $P22_{S39C}$ modified with a cysteine-reactive ATRP initiator (1) was used as the macroinitiator and a size-constrained reaction vessel for ATRP growth of poly(AEMA) strands, cross-linked with bisacrylamide, inside the P22 VLP architecture to make P22-xAEMA. Subsequently, this internal polymer scaffold was modified with primary amine-reactive labeling agents, either (2) or (3), to introduce a high density of new functionality to the construct.

Results and Discussion

In this work we utilized a VLP (derived from the bacteriophage P22) that consists of 420 subunits arranged on an icosahedral lattice with a resulting exterior diameter of 64 nm and an unoccupied internal cavity with a 54 nm in diameter.[78] Recombinant expression in Escherichia coli requires co-expression of the coat protein and scaffold protein for self-assembly. This VLP is capable of transformation into a series of distinct morphologies, which includes the procapsid (PC) morphology that contains the scaffold protein, an empty shell (ES) form in which the scaffold protein is removed, an expanded form (EX) and a wiffleball (WB) structure in which all 12 pentamers are removed (Appendix C, Figure C1). The EX form most closely mimics the morphology found in the DNA containing infectious virion and is the form used in this study To attain the EX form, the scaffold protein is removed from the PC using successive guanidine.HCl extractions followed by heating at 65 8C, which generates the capsid in its EX morphology. A new P22 mutant was designed for use with ATRP that contained a single - point mutation in the wild-type coat protein ($P22_{S39C}$) and introduced an addressable thiol suitable for the attachment of an initiator (1). This site was selected specifically such that the introduced thiol could be exposed exclusively to the interior according to the currently available P22 structural models (Figure 5.2).[76; 77] Although the wild-type protein contains an intrinsic cysteine (C405) it was not removed because previous studies demonstrated that this site is not addressable.[80; 187] This new mutant was characterized and behaves in the same manner as the wild-type P22 capsid, going through the same series of morphological transformations. To obtain the EX morphology, the scaffold

protein was removed from $P22_{S39C}$ to generate the ES, heated to 65ºC, and subsequently analyzed to ensure the formation of the EX morphology (Figure 5.3). The characteristic shift of the particles to a lower electrophoretic mobility was observed on heating, consistent with expansion of the capsid. Precipitation of the protein was observed only at temperatures greater than 80 C, which indicates that the protein architecture is relatively thermostable (Appendix C, Figure C2). The size of the VLP, by dynamic light scattering (DLS), increased as expected from 60±4 nm (PC morphology) to 71±5 nm, consistent with the known range of values for the P22 particle in either the EX or WB morphologies (Figure 5.3D). By transmission electron microscopy (TEM) the overall structure of the VLP was retained and, after heating to 75 ºC large pores became apparent in the structure (Figure 5.3C), which is a characteristic of the WB morphology.

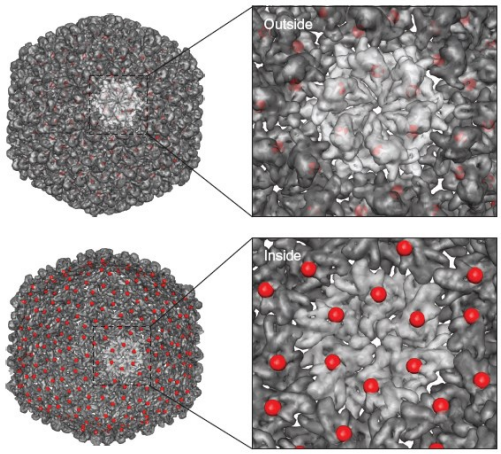

Figure 5.2: Structural model of the expanded morphology of the P22 capsid that shows the location of the S39C mutation. The location of the modified residue, S39C (in red) was derived from a structural model of P22 using coordinate data deposited as Protein Data Bank file 2XYZ. Both a view of the exterior of the capsid (top) and a half shell cut-away view that revealed the interior (bottom) of the capsid are included and illustrate that, according to this model, this mutation site is interior exposed.

To make the P22 macroinitiator, the $P22_{S39C}$ mutant was labeled with initiator 1, an amide derivative of a previously reported ATRP initiator. This cysteine -reactive ATRP initiator (Figure 5.1) was selected because of its efficient labeling, satisfactory initiation and demonstrated compatibility with biomolecules. Initiator 1, unlike the ester-containing form previously reported, is expected to be less susceptible to bond cleavage.[110; 203] It was synthesized through the modification of established protocols and selectively reacted with $P22_{S39C}$ to make $P22_{S39C}$-int with near-quantitative single labeling of the introduced cysteine, as observed by subunit mass spectrometry (Appendix C, Figure C3).

Using the $P22_{S39C}$-int macroinitiator construct, cross-linked AEMA polymer strands were synthesized inside this protein cage to make P22-xAEMA under standard ATRP biomolecule conditions using a Cu(I)/bipyridine To explore the range of reaction conditions available to the $P22_{S39C}$ system for internally directed polymerization reactions, initially a selection of AEMA:bisacrylamide monomer to subunit ratios (3,000–26,000) and temperatures (23, 40 and 60 ºC) as well as catalyst -loading ratios, were investigated. Samples were monitored by gel electrophoresis and DLS to determine reaction completion and suitable conditions (an example comparison is shown in Appendix C, Figure C4). The purified protein–polymer hybrid constructs were stable after polymerization and only at the highest temperature and loading conditions did the diameter of the cage increase significantly, which indicates that under most of the tested conditions the VLP effectively constrains the polymer growth to the interior of the capsid. From these test reactions it was apparent that the monomer loading had a greater impact

on the extent of polymerization than the temperature of the reaction, and that the reactions were effectively complete after less than three hrs.

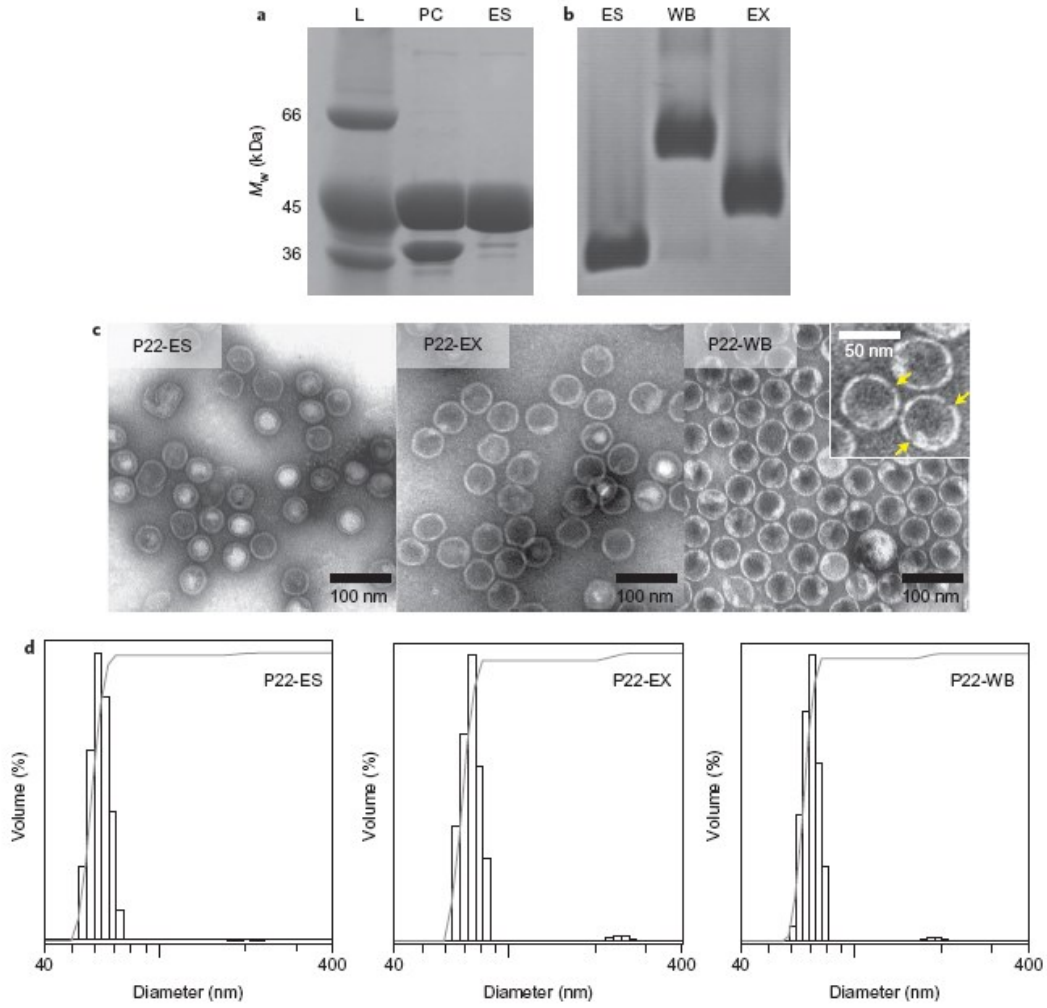

Figure 5.3: Characterization of the $P22_{S39C}$ mutant to verify morphological transformation. A) SDS-PAGE of the purified P22 before (PC) and after (ES) extraction of the scaffold protein. The lower band corresponds to scaffold (33.6 kDa) and the upper band is coat protein (46.6 kDa). L is the molecular weight standards. B) Native agarose gel of the P22 Es, EX and WB structures. The observed shift in mobility indicates the temperature-induced transformation from ES to EX and WB morphologies. C) Negatively stained TEM images of the ES, EX, and WB morphologies show the degree of particle-size homogeneity. The inset shows the appearance of small voids (yellow arrows) in the shell of the WB morphology. D) DLS of the three morphological forms (ES, EX, and WB). The measured hydrodynamic diameter for the expansion from ES (60 ± 4 nm) to EX (71 ± 5 nm) and WB (68 ± 4 nm) is as expected.

To verify further that our selected P22 mutant was confining the polymer, we compared the behavior of $P22_{S39C}$ to a second mutant of P22 coat protein ($P22_{K118C}$), described previously, and which has a reactive cysteine site predicted to be partially exposed to the exterior (Appendix C, Figure C5). [187] Both mutants were labeled with an ATRP initiator (Appendix C, Figures C6 and C7) and analyzed under simple polymerization conditions. We used the AEMA without addition of bisacrylamide at a loading of 26,000 monomers/subunit of the partially exterior-exposed $P22_{K118C}$ to make $P22_{K118C}$-AEMA, which resulted in dramatically different material properties compared to those of the $P22_{S39C}$ treated under the same conditions ($P22_{S39C}$-AEMA) and emphasizes the importance of site specificity for polymer initiation and growth in these protein architectures. When the initiator-labeled $P22_{K118C}$ was treated to make $P22_{K118C}$-AEMA, the construct exhibited an increase in diameter of about 20 nm, from 60 ± 3 nm to 81 ± 4 nm, as measured by DLS, which suggests the growth of polymer on the exterior of the cage (Appendix C, Figure C8), but the $P22_{S39C}$ -based sample diameter remained constant before (67 ± 4 nm) and after (67 ± 4 nm) polymerization. In addition, unlike $P22_{S39C}$-AEMA, the $P22_{K118C}$-AEMA hybrid was not very stable. Although no precipitation was observed under the reaction conditions, mass precipitation of the $P22_{K118C}$-AEMA occurred on purification. This loss could be alleviated partially by increasing the ionic strength of the buffer (>250 mM NaCl). Taken together, these data support a model in which the initiation site determines the overall access of the AEMA polymer to the exterior environment and when the polymer growth is exposed to the exterior of the cage, the protein–polymer composite destabilizes significantly. We

directed our efforts to the interior -facing $P22_{S39C}$-int macroinitiator construct at a midrange monomer loading (6,000 monomers/subunit) with bisacrylamide present and moderate temperature conditions (23ºC) for further investigation with four experimental replicates. After three hrs of reaction time, the synthesis was halted by exposing each sample to air and the protein–polymer conjugate ($P22_{S39C}$-xAEMA) was purified away from the remaining AEMA and bisacrylamide monomers and the copper catalyst by pelleting the protein construct using ultracentrifugation, which easily separates large macromolecular complexes from small molecular species. The resulting construct exhibited a dramatic shift in electrophoretic mobility, by native agarose gel, which indicates that the P22-int had become P22-xAEMA (Appendix C, Figure C9). On a subunit basis an increased subunit mass (by denaturing gel analysis) was observed, as indicated by a shift to a higher molecular mass (Figure 5.4A and Appendix C, Figure C9). By this analysis method, it appears that not all of the initiator-labeled subunits produced sufficiently long polymer chains for a mass shift to be apparent. Others also observed this incomplete initiation in both monomeric and multimeric systems when making grafted-from protein–polymer composites.[106; 110; 164; 203]

To confirm that the polymer was confined to the interior of the P22, the size of the $P22_{S39C}$-xAEMA construct was compared to that of the initial macroinitiator P22 complex. When the particles were visualized using TEM, the morphology of P22 after the reaction was unchanged from that before (Figure 5.4B). The average particle diameter was 51±3 nm in the unpolymerized $P22_{S39C}$-int and remained the same (53±3 nm) after the reaction. In addition, the hydrodynamic diameter, as measured by DLS, remained

unchanged on polymer formation (Figure 5.4C). The particle diameters were 70±10 nm and 71±3 nm, respectively, for $P22_{S39C}$-int and $P22_{S39C}$-xAEMA, which further confirms that the polymer was confined to the interior of the protein cage.

Multiangle light scattering (MALS) was used to analyze further the $P22_{S39C}$-xAEMA construct for the radius and molecular weight (Figure 5.5). According to this method the radius of the particles remained nearly constant, measured as 29.3 nm ($P22_{S39C}$-int) and 28.2 nm ($P22_{S39C}$-xAEMA), but the molecular weight increased on polymerization. Using the standard refractive index increment (dn/dc) for protein (0.185) and the published value for AEMA (0.153) [204] , the MALS data from the $P22_{S39C}$-int and $P22_{S39C}$-xAEMA samples were fitted to obtain molecular weights. The measured molecular weight for $P22_{S39C}$-int was 18.9 ± 0.2 MDa, consistent with the predicted value for the EX morphology of P22, but the $P22_{S39C}$-xAEMA had a combined molecular weight of 20.2 ± 0.6 MDa, with 18.7 ± 0.5 MDa contributed from the protein and 1.5 ± 0.4 MDa contributed from the polymer. This mass increase corresponds to the addition of 12,000 ± 3,000 AEMA monomers/VLP or 28 ± 7 AEMA monomers/subunit, on average.

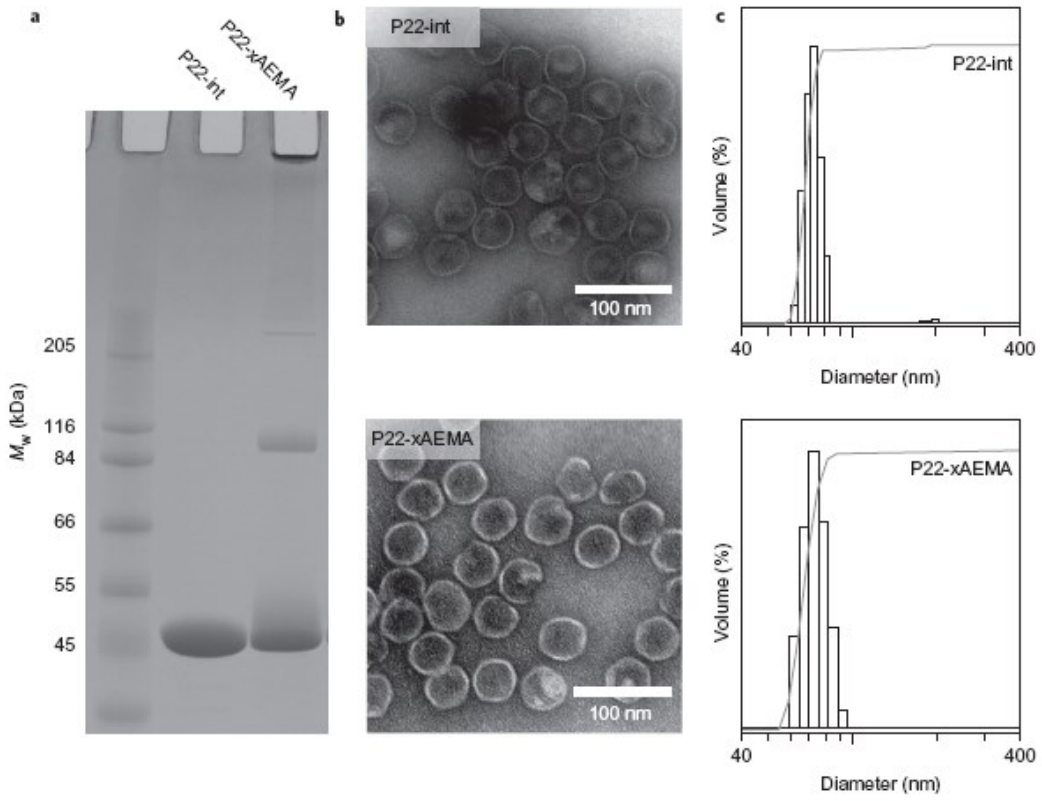

Figure 5.4: Size and morphological characterization of the $P22_{S39C}$-xAEMA composite and $P22_{S39C}$-int. A) Representative SDS-PAGE gel of $P22_{S39C}$-int and $P22_{S39C}$-xAEMA. The polymerized sample shows some streaking to higher Mw, which indicates the range of polymer chain lengths appended to the subunits as compared to the starting P22. In addition, highly cross-linked material can be observed in the well at the top of the gel. B) TEM images of $P22_{S39C}$-int (top) and $P22_{S39C}$-xAEMA (bottom) illustrate that the $P22_{S39C}$-xAEMA retains the size and shape homogeneity of the P22 capsid after the polymerization reaction. C) DLS of $P22_{S39C}$-int (top) and $P22_{S39C}$-xAEMA (bottom). The modified sample is monodisperse and has the same average diameter as that of the starting $P22_{S39C}$-int.

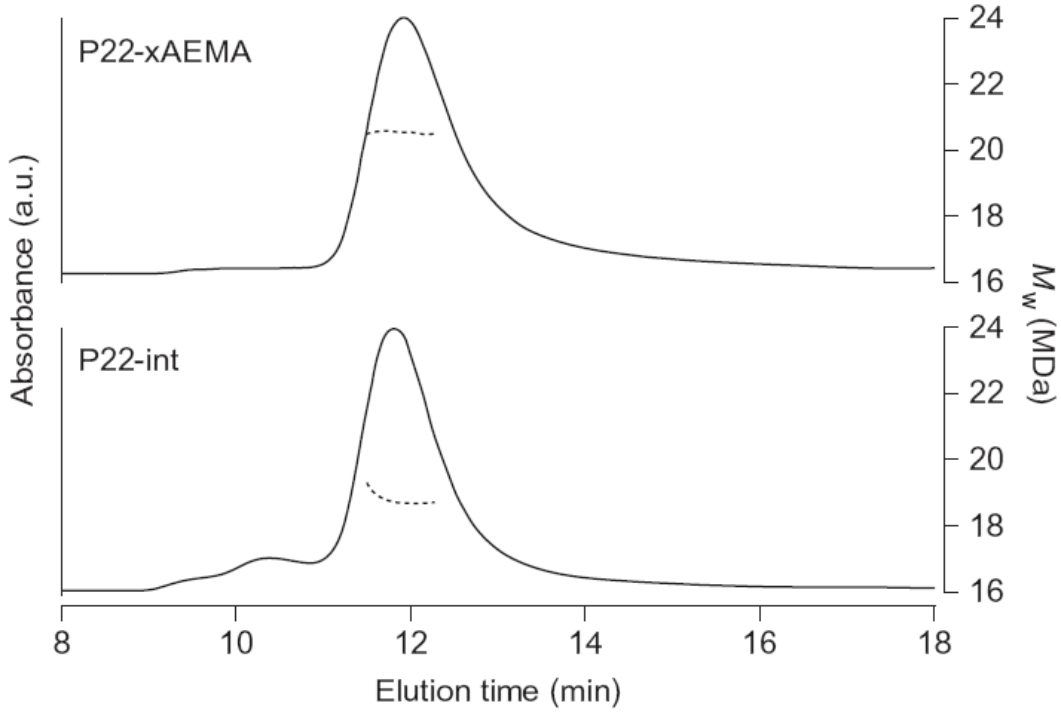

Figure 5.5: Molecular weight increase as a result of polymerization, monitored by MALS. Using size exclusion chromatography, both $P22_{S39C}$-xAEMA and $P22_{S39C}$-int exhibit the same elution time when monitored by absorbance (continuous line) at 280 nm, which indicates retention of the particle size. Fitting the MALS data across the elution profile reveals the molecular weight of the material (dashed line), which increases substantially for the $P22_{S39C}$-xAEMA (top) compared to the $P22_{S39C}$-int (bottom). a.u. = arbitrary units.

The internally directed $P22_{S39C}$-xAEMA polymerization resulted in the introduction of a large number of addressable amines sequestered within the protein cage. To demonstrate that the introduced amines on the poly(AEMA) inside the $P22_{S39C}$-xAEMA construct were addressable, FITC (2) was used as an amine -specific labeling agent. Both the $P22_{S39C}$-xAEMA and $P22_{S39C}$-int control were incubated with a 100 -fold excess of FITC per subunit to give $P22_{S39C}$-xAEMA-FITC and $P22_{S39C}$-int-FITC, respectively. Excess FITC was removed by pelleting the protein twice using

ultracentrifugation followed by resuspension before analysis. The difference in the degree of labeling between the $P22_{S39C}$-int-FITC and $P22_{S39C}$-xAEMA-FITC was significant enough to be readily discernible (Appendix C, Figure C10).

When the fluorescently labeled $P22_{S39C}$-xAEMA construct was analyzed using gel electrophoresis the fluorescein signal was observed to migrate with the protein. Under denaturing sodium dodecyl sulfate polyacrylamide gel electrophoresis (SDS–PAGE) conditions, the fluorescein migrated with the subunit and with the polymer-modified subunit, which indicates that the fluorescent dye was bound covalently to the construct and not just sorbed onto the protein–polymer composite (Appendix C, Figure C11). When analyzed by native agarose gel electrophoresis, a net shift in the electrophoretic mobility of the $P22_{S39C}$-xAEMA and $P22_{S39C}$xAEMA-FITC was observed, caused by the polymer and FITC altering the charge of the construct (Figure 5.6A). The observed shift indicates that the polymer and dye were associated tightly with the protein cage. The $P22_{S39C}$-xAEMA-FITC was labeled to the extent that the migration of a distribution of species was visible prior to staining under ambient light, but $P22_{S39C}$-int-FITC was observed only weakly (Figure 5.6B). In contrast, the emission signal of the $P22_{S39C}$xAEMA-FITC distribution was depressed in intensity compared to that of the much less heavily labeled $P22_{S39C}$-int-FITC (Figure 5.6C), which probably results from self-quenching of the fluorophore caused by the abundance of polymer-bound fluorescein in close proximity. This apparent loss of fluorescence intensity was confirmed by solution -phase analysis of the constructs, in which a greater than 95% reduction in fluorescence was observed in the $P22_{S39C}$-xAEMA-FITC compared to $P22_{S39C}$-int-FITC (Appendix C, Figure C12). Similar

quenching was shown in systems with high fluorophore concentrations, such as micelles, where derivatives of fluorescein can lose more than 98% of their fluorescence signal because of proximity and dimerization effects. [205; 206]

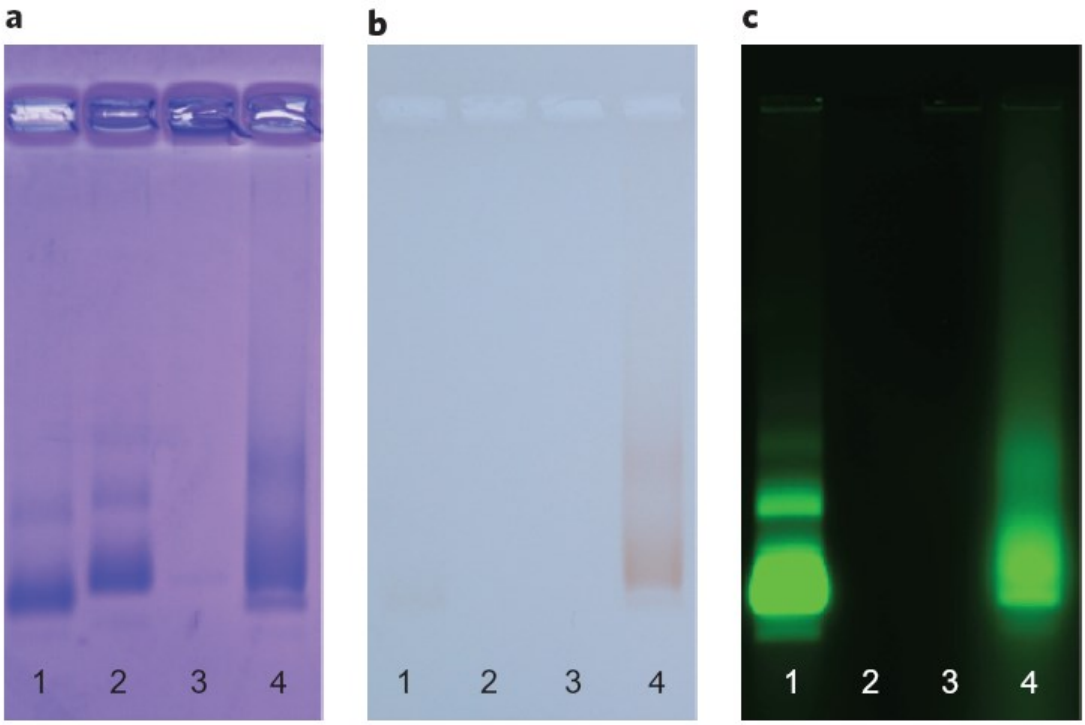

Figure 5.6: Polymer formation and covalent modification with FITC was verified by native agarose gel electrophoresis. (A-C) Three different views of the same native agarose gel with $P22_{S39C}$-int-FITC (lane 1), $P22_{S39C}$-int (lane 2), $P22_{S39C}$-xAEMA (lane 3), and $P22_{S39C}$-xAEMA-FITC (lane 4). A) The gel was stained with Coomassie to detect the protein component. The $P22_{S39C}$-xAEMA runs slightly out of the well in the opposite direction to the other proteins due to the net positive charge on the poly(AEMA) at the running-buffer pH. Labeling this construct with the negatively charged FITC reverses the effective net charge on the construct and results in a shift in migration direction. B) The unstained gel under ambient light. The $P22_{S39C}$-int-FITC sample is faintly visible and the $P22_{S39C}$-xAEMA-FITC sample is clearly visible, which signifies the relative degree of FITC labeling in each sample. C) The unstained gel illuminated with a laser at 488 nm and detected at 520 nm to highlight FITC. The $P22_{S39C}$-int-FITC is considerably brighter than the $P22_{S39C}$-xAEMA-FITC, which indicates the relative degree of fluorescence quenching in each sample.

After demonstrating polymerization within the P22 capsid and the postsynthetic modification of the functional groups, we explored the $P22_{S39C}$-xAEMA composite system as a potential T1 contrast agent through the attachment of Gd-DTPA-NCS (3) to the encapsulated polymer. Gd-DTPA-NCS was added, in a 100 -fold excess per subunit, to the $P22_{S39C}$-xAEMA or $P22_{S39C}$-int and allowed to react overnight, followed by pelleting by ultracentrifugation and resuspension of the protein twice in each of four experimental replicates. The resulting material ($P22_{S39C}$-xAEMA-Gd or $P22_{S39C}$-int-Gd) was analyzed for both sulfur and gadolinium content by inductively couple plasma mass spectrometry (ICP-MS) to determine both the Gd and protein concentrations. To rule out the possibility of simple electrostatic interaction between the polymer and Gd-DTPA, controls with both $P22_{S39C}$-xAEMA and $P22_{S39C}$-int were incubated and isolated, under the same conditions as above, with Magnevist (Gd-DTPA), which lacks the aminereactive isothiocyanate. When these constructs were analyzed by native agarose gel electrophoresis (Appendix C, C13), a net shift in the electrophoretic mobility of the $P22_{S39C}$-xAEMA-Gd was observed, caused by the polymer and Gd-DTPA-NCS altering the net charge of the construct, but the $P22_{S39C}$-xAEMAMagnevist sample retained the same low electrophoretic mobility as that of the $P22_{S39C}$-xAEMA, which provides evidence that there were no significant electrostatic interactions between $P22_{S39C}$-xAEMA and Gd-DTPA.

The Gd-DTPA loading per P22 was determined quantitatively for each of the constructs from the ICP-MS data. The $P22_{S39C}$-xAEMA-Gd contained 28 times more Gd/VLP than the $P22_{S39C}$-int-Gd control (320 Gd/VLP, <1 Gd/subunit), where

endogenous lysines were modified, which indicated that it is largely the polymer that is being labeled rather than the protein shell. The low reactivity of the endogenous P22 lysines was reported previously, with only a few of the 20 lysines per subunit observed to be reactive.[188] This minimal background reactivity is advantageous because it means that in the $P22_{S39C}$-xAEMA sample the vast majority (>95%) of the addressable sites are located on the encapsulated polymer. If necessary, endogenous lysines could be blocked chemically prior to polymerization.[51] The $P22_{S39C}$-xAEMA-Gd loading per cage was 9,100 ± 800 Gd/VLP (22 ± 2 Gd/subunit), which corresponds to an internal concentration of 150 mM Gd within the VLP. This is significantly more Gd, both on a per-cage and per-subunit basis, than that in previous reports using VLPs, with values that ranged from less than 1.0/subunit to 6.6/subunit (60/VLP to 650/VLP), and highlights the advantage of using the full capacity of the interior volume.[25; 26; 36; 43-45; 84; 106; 207]. In addition, both the $P22_{S39C}$-xAEMA and $P22_{S39C}$-int incubated with Magnevist (Gd-DTPA) contained Gd levels below the lower limit of quantification, which demonstrates that the Gd detected is attached covalently to the protein–polymer construct rather than associated via electrostatic interactions under the labeling reaction conditions.

To verify that the high loading observed was reasonable and occurred homogeneously across the population of P22 capsids, the particles were analyzed by analytical ultracentrifugation to investigate differences in sedimentation velocity (Figure 6.7). The measured sedimentation value of the $P22_{S39C}$-xAEMA (167 S) falls within the range observed for $P22_{S39C}$-int (142 S) and the scaffold protein-filled PC morphology (191 S), which indicates that the polymer content does not exceed the packing observed

in the naturally occurring self-assembled system. Covalent modification of polymer with Gd-DTPA-NCS to make $P22_{S39C}$-xAEMA-Gd resulted in a shift to a higher S value (227 S), which is consistent with the efficient incorporation of additional mass via Gd-DTPA-NCS to the interior of the VLP.

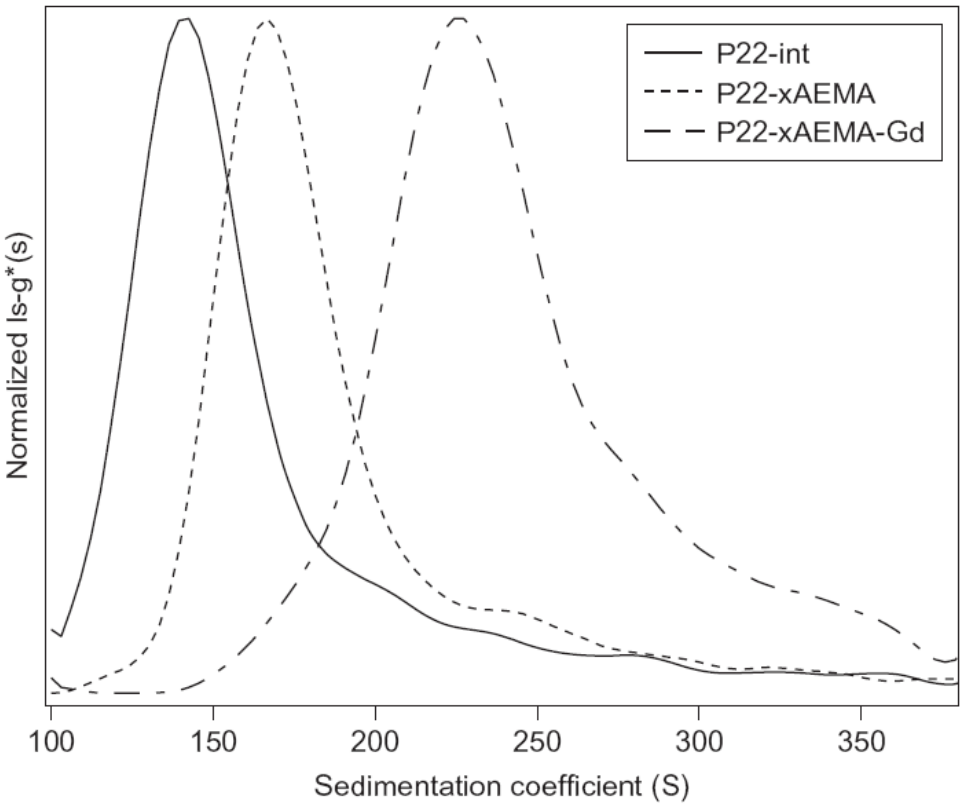

Figure 5.7: Analysis of sample population homogeneity by analytical ultracentrifugation. Samples were centrifuged at 5,000-7,000 rpm and absorbance data were acquired at 280 nm and modeled to calculate the apparent sedimentation coefficient distribution ls-g*(s) for each sample. The measured sedimentation value of the $P22_{S39C}$-xAEMA (167 S) shows an increase from that of $P22_{S39C}$-int (142 S) and covalent modification of polymer with Gd-DTPA-NCS to make $P22_{S39C}$-xAEMA-Gd resulted in a shift to a higher S value (227 S), consistent with the incorporation of additional mass via Gd-DTPA-NCS labeling of the polymer. These data indicate that there is a homogeneous shift in the entire population to higher S values with each modification.

The 1H relaxivity of water in the presence of these highly loaded $P22_{S39C}$-xAEMA-Gd particles and $P22_{S39C}$-int-Gd was measured at 60 MHz (1.4 T), using an inversion recovery -pulse sequence. The $P22_{S39C}$-xAEMA-Gd and $P22_{S39C}$-int-Gd had ionic relaxivities (r1) of 22.0 $mM^{-1}s^{-1}$ and 23.5 $mM^{-1}s^{-1}$, respectively. The observed improvement in r1 for both constructs is consistent with an enhancement over free Gd-DTPA (4.0 mM-1s-1) due to an increase in the rotational correlation time that arises from tethering the chelate to a large supramolecular particle.[25; 36] In addition, because the ionic relaxivity is enhanced similarly in both constructs it can be concluded that the polymer does not restrict water exchange significantly between the bulk and the interior of the $P22_{S39C}$-xAEMA-Gd composite, as water restriction would lessen the observed enhancement, as is seen in some micelles and liposomes.[39; 208]

In addition to the ionic relaxivity enhancement, each $P22_{S39C}$-xAEMA-Gd carries 9,100 ± 800 Gd/VLP, which leads to a per particle relaxivity of 200,000 $mM^{-1}s^{-1}$. The particle relaxivity of $P22_{S39C}$-xAEMA-Gd dramatically exceeds that of the $P22_{S39C}$-int-Gd control (7,500 $mM^{-1}s^{-1}$) and those in previous reports of VLP nanoparticle -based MRI contrast agents, with values that fall in the range of 103–104 $mM^{-1}s^{-1}$. [25; 26; 36; 43-45; 84; 106; 207] The particle relaxivity is also higher than those observed for many other macromolecular assemblies, such as micelles, liposomes and polymers, which places this construct comfortably in the upper end of observed macromolecular relaxivities for its size.[39; 208-211]

Conclusion

In summary, the application of ATRP for site-directed polymer formation inside a VLP results in an anchored network that is unparalleled for labeling purposes and utilizes the previously largely untapped interior volume of the VLP. The $P22_{S39C}$-based macroinitiator effectively directs polymer growth to the VLP interior, which results in a confined polymer growth because the protein shell acts as a barrier to unconstrained polymer growth, to leave only the protein shell exposed to the bulk solution. By selecting an appropriate macroinitiator and monomer, this new multimeric protein–polymer composite acts as a scaffold for the attachment of small molecules of interest, such as the fluorophore FITC or paramagnetic MRI contrast agents (here, Gd-DTPA-NCS). The introduced polymer scaffold results in a significantly increased number of labels per cage compared to those of other VLP -based systems. The improvement in labeling is important for the delivery of contrast agent on a per-particle basis as it allows for a high concentration delivery of contrast agent or other cargo molecules of interest. This material exhibits an order -of -magnitude improvement in relaxivity per particle over that of existing VLP systems. The use of this material as a targeted MRI contrast agent is particularly interesting because of the high relaxivity and is an application we are exploring further. As a consequence of the simplicity, modular nature and loading level of the ATRP -based approach taken to make these P22–polymer internal composites, currently this same method is being employed to make a range of novel VLP– polymer composites with biomedical and catalytic applications.

Experimental

All materials were analytical grade and purchased from either Sigma-Aldrich or Fisher Scientific and used as received unless otherwise noted. Dichloromethane was distilled over calcium hydride prior to use. All water was deionized using a NANOpure water purification system. Dynamic light scattering measurements were taken on a 90Plus particle size analyzer (Brookhaven).

Mutagenesis.

The P22(S39C) point mutation was made using established polymerase chain reaction protocols (Qiagen) using pET-11a based plasmids encoding genes for scaffolding and coat protein. The amplified DNA was transformed into E. coli strain BL21 (DE) and selected for ampicillin resistance.[187]

Protein Purification.

Transformed BL21 (DE3) *E. coli* were grown in 1L cultures inoculated with 1 mL starter culture at 37°C with vigorous shaking overnight. The bacteria were then centrifuged away from the media at 3700 g for 20 minutes. The cell pellets were resuspended in PBS pH 7.2 and were incubated with DNAse, RNAse, and lysozyme (all Sigma-Aldrich) for 30 minutes on ice. Cells were lysed further by sonication on ice. The cell debris was removed via centrifugation at 12,000 g for 45 minutes. The supernatant was then loaded on a 35% sucrose cushion and centrifuged at 48,000 rpm for 50 minutes in an ultra centrifuge (Sorvall). The resulting virus pellet was resuspended in PBS pH 7.0, spun at 17,000 rpm for 20 minutes to remove particulates and lipid providing 135 mg of

P22 procapsid (PC). Scaffold protein was extracted using 0.5 M guanidine-HCl in 4 repeated cycles. The P22 empty shells were then dialyzed against PBS pH 7.0 overnight resulting in 86 mg (64% yield) P22 empty shell (ES). The empty shell P22 was heat treated for 20 min at 65^{o}C to transform the protein into its expanded form as previously described and analyzed.[187] The heat treated samples were purified by pelleting as above, followed by resuspension into PBS pH 7.6 in preparation for protein labeling yielding 58 mg (68% yield form ES) of P22 expanded shell (EX) from 1L of initial *E. coli* culture.

Synthesis of 2-Bromoisobutyryl Aminoethyl Maleimide (**1**).

1 was synthesized by a modification of the procedures previously reported.[110; 203] N-2-aminoethyl-maleimide (250 mg, 0.98 mmol) was mixed on ice with triethylamine (300 μL, 2.2 mmol) in 5 mL dry dichloromethane. 2-bromo-2-methylpropionylbromide (200 μL, 1.6 mmol) was added dropwise. The reaction was allowed to warm to room temperature and was subsequently extracted 3 times from dichloromethane and water followed by drying over anhydrous sodium sulfate. The crude product was cleaned via column chromatography (silica gel, 10% ethyl acetate in dichloromethane) with a yield of 80%. ^{1}H NMR (500 MHz, $CDCl_3$) δ = 1.89 (s, 6H, CH_3); 3.46 (dd, J = 5.5, 5.5, 2H, NCH_2); 3.72 (dd, J = 5.0, 1.5, 2H, NCH_2); 6.71 (s, 2H, CH_{vinyl}), 6,97 (s, NH). ^{13}C δ = 32.54 (CH_3), 37.34 (NCH_2), 39.84 (NCH_2), 62.51 (C), 134.59(CH_{vinyl}), 170.96 (CO), 172.74 (CO). ESI-MS: *m/z* calculated 289.0188, 291.0167 (MH^+), found *m/z* 289.0192, 291.0179.

P22-int Macroinitiator Formation Conditions**.**

$P22_{S39C}$ in PBS, pH 7.6 (4 mL, 7.2 mg/mL) was infused with 156 µL of **1** (80 mM inDMSO, 10 fold excess per a subunit). The mixture was allowed to react for 3 hrs at room temperature. After 3 hrs the reaction was quenched with DTT (156 µL, 80 mM in water). To remove excess DTT and **1**, the protein was pelleted at 48,000 rpm for 50 minutes in an ultra centrifuge (Sorvall) followed by resuspension into PBS, pH 7.6. By subunit mass spectrometry >95% of the subunits were labeled. Yield: quantitative.

P22-AEMA Polymer Formation Conditions.

Each experimental replicate was made in a large crimp-top vial with the addition of 20 mL monomer solution (4 wt% 16:4 AEMA:bis-acrylamide in PBS, pH 8.0) and 11 mL buffer (PBS, pH 8.0) followed by pH adjustment with concentrated sodium hydroxide solution as needed back to pH 8.0. To this mixture, 6 mL of P22-int (8.0 mg/mL, 1.0 µmoles subunit, pH 8.0) was added followed by pump and back filling with Ar 4 times to deaerate the mixture. The metal catalyst solution was made in a second crimp vial where 19.2 mg CuBr (0.13 mmoles), 29.9 mg CuBr2 (0.13 mmoles), and 83.5 mg 2,2'-bipyridine (0.53 mmoles) followed by the addition of 10 mL deionized water which had been degassed by bubbling Ar through the liquid for 20 minutes. The vial was subsequently sonicated for 5 min to obtain a dark brown solution. To the monomer-protein vial, 3 mL of the metal catalyst solution was added and the vial was maintained at 23 ºC for the remaining duration of the experiment. After 3 hr the reaction was quenched by exposure to air and the protein-polymer composite was purified away from unreacted

monomer and the copper catalyst by pelleting and resupending the protein 2 times into 100 mM sodium carbonate with 50 mM NaCl buffer, pH 9.0. Yield: 38.7 mg (81%).

FITC (**2**) Labeling Conditions**.**

To 2.0 mL $P22_{S39C}$-xAEMA (0.086 μmoles subunit, carbonate buffer, pH 9.0) at 2 mg/mL, 343 μL FITC (8.6 mmoles, 25 mM in DMSO) was added dropwise while vortexing the protein solution. The mixture was allowed to sit overnight at 4 ºC followed by purification away from excess FITC by pelleting and resuspending (carbonate buffer, pH 9.0) the protein twice over.

Gd-DTPA-NCS (**3**) Labeling Conditions**.**

Gd-DTPA-NCS was made according to established procedures.[36] Briefly, 2.80 mg (4.31 μmoles) DTPA-NCS was dissolved in 40 μL of 1M sodium bicarbonate and 200 μL water. Once the DTPA-NCS was completely dissolved, 5.27 μL $GdCl_3$ (900 mM in water, 4.74 μmoles) was added to the solution and stirred for 3 hrs at room temperature. The solution was subsequently diluted to 10 mM with DMSO (186 μL) and added to the protein-polymer conjugate as follows. To 4.0 mL (0.17 μmoles subunit, 2 mg/mL carbonate buffer, pH 9.0) $P22_{S39C}$-AEMA, 1700 μL (17 μmoles) Gd-DTPA (10 mM in DMSO/H_2O) was added dropwise while vortexing the protein solution. The mixture was allowed to sit overnight at 4 ºC followed by purification away from excess Gd-DTPA by pelleting and resuspending the protein twice. Yield: 5.2 mg (65%).

Subunit Mass Spectrometry.

Subunit masses of the P22 coat and P22-int macroinitiators were analyzed by ESI-Q-TOF mass spectrometry (Q-TOF Premier, Waters) interfaced to a Waters Acquity UPLC and autosampler. [212] Samples were loaded onto a BioBasic-300 SEC column (5 μm, 250 L x 1.0 mm I.D., Thermo Scientific) and eluted with buffer containing 40% isoproanol, 59.9% water, and 0.1% formic acid isocratically with a rate of 25 μL/min. Mass spectra were acquired in the range of m/z 50-5000 and processed using the MaxEnt 1 algorithm for MassLynx version 4.1 to obtain deconvoluted average masses from multiple charge state distributions.

Transmission Electron Microscopy.

The P22-int macroinitiators and P22-polymer composites were imaged by transmission electron microscopy (Leo 912 AB) by negatively staining the sample with 1% uranyl acetate on formvar carbon coated grids. For the diameter measurements 200 particles were measured for each sample.

Denaturing Gel Assay.

P22-int macroinitiators and P22-polymer composites were analyzed using SDS-PAGE on 10-20% gradient Tris-glycine gels (Lonza). Fluorescence imaging of the gels was carried out on a Typhoon TRIO (GE Healthcare) gel scanner with excitation at 488 nm and detection at 526 nm. Protein was detected by staining with Coomassie blue.

Native Agarose Gel Assay.

P22-int macroinitiators and P22-polymer composites were analyzed on 0.8% native agarose gel using 40 mM Tris-base, 5 mM sodium acetate, 1 mM EDTA, pH 8.2 running buffer and were run for 3 hrs at 65 volts. Fluorescence imaging of the gels was carried out on a Typhoon TRIO (GE Healthcare) gel scanner with excitation at 488 nm and detection at 526 nm. Protein was detected by staining with Coomassie blue.

Multi-Angle Light Scattering.

P22-int and P22-xAEMA samples were separated over a WTC-0100S (Wyatt Technologies) size exclusion column at flow rate of 0.7 mL/min (Agilent 1200 HPLC) in 50 mM phosphate, 500 mM sodium chloride, pH 8.0. Each sample injection was 25 μL and the samples were run in triplicate. Elution profiles were for mass analysis were detected using a UV-Vis detector (Agilent), aWyatt HELEOS multi angle light scattering detector, and a Wyatt Optilab rEX differential refractometer. Using the elution profile data the number average molecular weight, Mn, was calculated with Astra 5.3.14 software (Wyatt Technologies) using a dn/dc for protein of 0.185 and a dn/dc for the polymer component of 0.153.[204]

Analytical Ultracentrifugation.

Sedimentation velocity experiments were performed in an XL-A ultracentrifuge (Beckman Coulter, Fullerton, CA) using a AN-60Ti rotor. Epon double-sector centerpieces were filled with 390 μL or 400 μL of sample and the corresponding reference buffer, respectively. The samples were centrifuged at 20°C and 5,000-7,000 rpm. Absorbance data were acquired at wavelength of 280nm. The raw data were

analyzed using SEDFIT software, implementing the ls-g*(s) model. Input parameters such as buffer density and viscosity were determined using Sednterp software.

Relaxivity Measurements.

T1 measurements were carried out on Anasazi FT-NMR 60MHz (1.41 T) spectrometer for all samples. Each P22-xAEMA-Gd (0.61 mM Gd, 1.3 mg/mL protein) experimental replicate was diluted with 67% D_2O in H_2O to yield a dilution series with concentrations of 0.20, 0.068, 0.023 mM Gd. The longitudinal relaxation rate constant (T1) at each dilution was measured using an inversion recovery pulse sequence (90º pulse width of 6.3 μs with 8 experiments of 1 scan) at 298 K, where the relaxation delay was set to six times the estimated T1 (Figure Appendix C, Figure C12A-C). To attain the actual T1 value, the following equation for T1 relaxation:

$$M_z = A(1-\exp(-t/T1))+B$$

was fit to the experimental data acquired at each dilution where A, B, and T1 were used as fitting parameters.{Mitchell, 2004 #171} The plot of inverse T1 versus Gd (mM) for the 3 dilutions was used to determine relaxivity values (r1), where relaxivity per Gd is equal to the slope of the line (Appendix C, Figure C12D) and relaxivity per VLP was calculated by multiplying the slope by Gd/VLP.

Protein and Gd Concentration.

The protein concentration was determined by analyzing samples for sulfur content and Gd concentration by inductively couple plasma mass spectrometry (ICP-MS) at Energy Labs (Billings, MT). Samples were submitted in triplicate and average

concentrations were reported. The protein concentration was obtained by subtracting from the detected sulfur concentration the Gd contribution due to sulfur in the DTPA-NCS chelator. The remaining sulfur content was converted to subunit concentration using a conversion factor of 13 thiols per a subunit (the initial Met in the P22 coat sequence is never present in the final protein according to mass spectrometry).

CHAPTER 6

MANGANESE (III) PORPHYRINS COMPLEXED WITH P22 VIRUS-LIKE PARTICLES AS T_1-ENHANCED CONTRAST AGENTS FOR MAGNETIC RESONANCE IMAGING (MRI)

Contributions of Authors and Co-Authors

Manuscript in Chapter 6

Author: Shefah Qazi

Contributions: Designed and carried out the experiments and wrote the manuscript.

Co-author: Masaki Uchida

Contributions: Assisted in experimental design.

Co-author: Robert Usselman

Contributions: Characterized the samples by NMR and analyzed the relaxivity data.

Co-author: Riley Shearer

Contributions: Polymerized samples for conjugation with Mn (III) porphyrin complexes.

Co-author: Ethan Edwards

Contributions: Synthesized initiator molecule used to label P22 for polymerization.

Co-author: Trevor Douglas

Contributions: Obtained funding, coordinated the project, and assisted with the design of the experiments. Discussed the results and edited the manuscript at all stages.

Manuscript Information Page

Authors: Shefah Qazi, Masaki Uchida, Robert Usselman, Riley Shearer, Ethan Edwards, and Trevor Douglas
Journal: Journal of Bioinorganic Chemistry
Status of the manuscript:
____ Prepared for submission to a peer-reviewed journal
____ Officially submitted to a peer-reviewed journal
____ Accepted by a peer-reviewed journal
_X__ Published in a peer-reviewed journal

Publisher: Springer Link
Date of Submission: 2014
Issue in which manuscript appears: Volume 19, 237-246

CHAPTER 6

MANGANESE (III) PORPHYRINS COMPLEXED WITH P22 VIRUS-LIKE PARTICLES AS T_1-ENHANCED CONTRAST AGENTS FOR MAGNETIC RESONANCE IMAGING (MRI)

Published: *Journal of Bioinorganic Chemistry*, **2014**, 19, 237-246.

Shefah Qazi,[†] Masaki Uchida,[†] Robert Usselman,[€] Riley Shearer,[†] Ethan Edwards,[†] and Trevor Douglas[†,§]

[†]Chemistry and Biochemistry Department, Montana State University, Bozeman, Montana, 59717, USA
[€]National Institute of Standards and Technology, Boulder, Colorado, 80305, USA
[§]Department of Chemistry, Indiana University, Bloomington, Indiana, 47405, USA

Abstract

Virus-like particles are powerful platforms for the development of functional hybrid materials. Here, we have grown a cross-linked polymer within the confines of the bacteriophage P22 capsid (P22-xAEMA) and functionalized the polymer with various loadings of paramagnetic manganese (III) protoporphyrin IX complexes (MnPP) for evaluation as a macromolecular MRI contrast agent. The resulting construct (P22-xAEMA-MnPP) has $r_{1,particle}$ = 7,098 mM $^{-1}$ · s $^{-1}$ at 298 K, 2.1 T (90 MHz) for a loading of 3,646 MnPP/capsid. The Solomon-Bloembergen-Morgan (SBM) theory for paramagnetic relaxivity predicts conjugating MnPP to P22, a supramolecular structure, would result in an enhancement in ionic relaxivity, however, all loadings experienced low ionic relaxivities ranging from $r_{1,ionic}$ = 1.45 mM $^{-1}$ · s $^{-1}$ to 3.66 mM $^{-1}$ · s $^{-1}$, similar to ionic relaxivity of free MnPP. We hypothesize that intermolecular interactions between neighboring MnPPs block water access to the metal site resulting in low $r_{1,ionic}$ relaxivities. We investigated the effect of MnPP interactions on relaxivity further by either blocking or exposing water binding sites on MnPP. Based on these results, future design strategies for enhanced $r_{1,ionic}$ relaxivity are suggested. The measured $r_{2,ionic}$ relaxivities demonstrated an inverse relationship between loading and relaxivity. This results in a loading dependent r_2/r_1 behavior of these materials indicating synthetic control over the relaxivity properties making them interesting alternatives to current MRI contrast agents.

Introduction

Paramagnetic metal ions, such as gadolinium, manganese, and iron, have been extensively studied as MRI contrast agents due to their ability to efficiently relax water protons. Gadolinium-based small molecules are predominantly used in medical imaging protocols as T_1-enhanced MRI contrast agents [37; 213], but free gadolinium (III) ions are highly toxic and can cause nephrogenic systemic fibrosis (NSF) in patients with renal failure [214; 215]. Thus, there are considerable efforts to develop effective alternative contrast agents, and manganese is a promising candidate [216], with limited toxicity at low concentrations. High metal/ligand complex stability is an important factor in contrast agent development to avoid metal-ion exchange or release and can be provided by macrocycles such as porphyrins [217].

Over the years, a variety of porphyrins chelated with manganese (III) ions have been investigated for their potential use as magnetic resonance (MR) contrast agents [218-222]. Recently, Winter et al. successfully engineered a heme protein, heme nitric oxide / oxygen-binding (H-NOX) protein to replace its native heme with manganese (III) protoporphyrin IX complexes (MnPP) [222]. The engineered H-NOX exhibited enhanced relaxivity ($r_{1,ionic}$ = 12.0 $mM^{-1} \cdot s^{-1}$) at 60 MHz compared to the protein containing its native heme ($r_{1,ionic}$ = 5.9 $mM^{-1} \cdot s^{-1}$) and commercially available manganese and gadolinium-based contrast agents ($r_{1,ionic}$ = 3.0 $mM^{-1} \cdot s^{-1}$ for both). Although engineering of a heme protein as a scaffold of MnPP is an elegant approach, the number of MnPP per protein is limited to the number of heme binding sites, i.e. one per protein in their paper. In order to progress towards clinical application, we aim to establish a well-

designed molecular system that has the capability to encapsulate such agents with much higher loading density, protect them from the external environment, and deliver them to a targeted tissue.

One approach has been to use covalent attachment of small-molecule contrast agents to macromolecular platforms [35; 177]. Various groups have explored dendrimers [178], liposomes [39; 179], protein cages [36; 51], and gold nanoparticles [180] as potential platforms for conjugation of small-molecule contrast agents. Virus-like particles (VLPs) derived from virus particles but devoid of their nucleic acid have an advantage over other systems because of their large macromolecular size and control over assembly, which allows for high loading density of desired cargo molecules. We, and others, have explored these systems, such as Cowpea chlorotic mottle virus (CCMV) [44], Tobacco mosaic virus (TMV) [223], Cowpea mosaic virus (CPMV) [45], bacteriophages Qβ [106], MS2 [26; 43] and P22 [108; 224; 225] as macromolecular platforms for contrast-agent development. Although this research has resulted in the successful development of VLP-based MRI contrast agents, most of them utilized only the capsid surface to anchor imaging probes, not taking full advantage of the large interior cavity of the capsids.

Recently, we have successfully exploited the interior cavity of the P22 viral capsid and developed Gd-based MRI contrast agents with significantly high ionic (per Gd ion) and particle (per P22 capsid) relaxivities. In those studies, organic polymers were synthesized in the confined environment of the interior cavity of P22 VLPs either by a series of azide-alkyne 'click" reactions[108] or by atom-transfer radical polymerization (ATRP),[225] and were used as a scaffold to conjugate imaging molecules *via* a reactive

functional group on the polymer. This resulted in a significant increase in loading capacity of the cargo by taking full advantage of the capsid volume. Here, we explore the use of manganese (III) protoporphyrin IX (MnPP) complexed with P22 VLP-polymer hybrids (P22-xAEMA) as potential MRI contrast agents. MnPP was conjugated to P22-xAEMA *via* a coupling reaction between carboxyl groups of the porphyrin and pendant amine groups of the P22-xAEMA (Figure 6.1) resulting in a high per-particle relaxivity for efficient T_1-enhanced MRI contrast-agent development. Furthermore, as ionic relaxivities of these constructs were lower than expected, we investigated MnPP aggregation, which we hypothesize is due to intermolecular interactions between neighboring MnPP that can potentially block water access to the metal site, and discuss potential solutions.

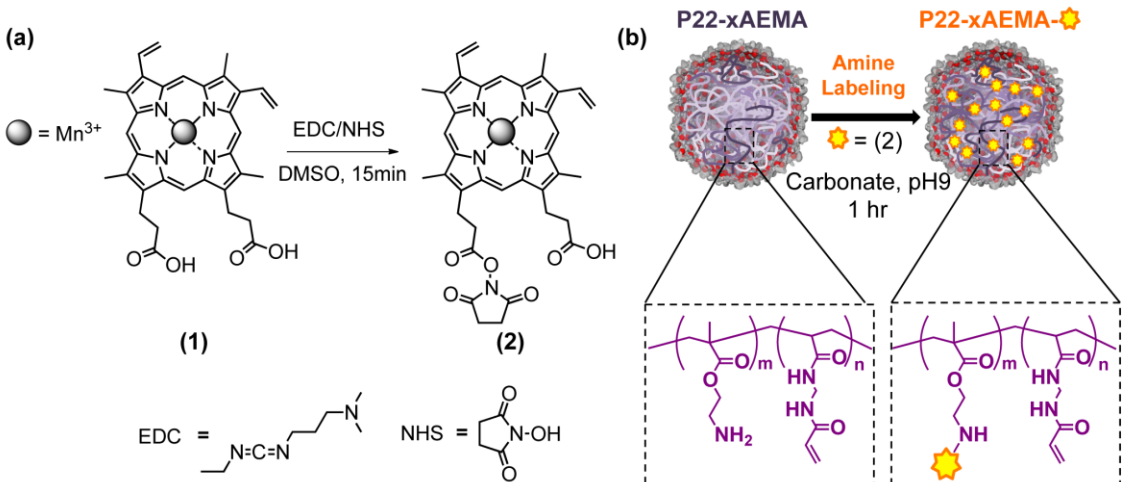

Figure 6.1: (a) Manganese (III) protoporphyrin IX MnPP (1) was reacted with EDC/NHS for 15 min in DMSO to create an activated species (2). (b) The resulting product (2) was reacted with P22-xAEMA for 1 hr in carbonate pH 9 buffer to couple MnPP to reactive amine groups on the P22-xAEMA polymer.

Results and Discussion

Synthesis

Manganese (III) protoporphyrin IX (MnPP) was attached to P22-xAEMA with various loadings by means of a simple coupling reaction.[121] The carboxylate groups of MnPP were activated with EDC/NHS and reacted with the amine functional groups of the P22-xAEMA polymer, encapsulated on the interior of the P22 capsid (Figure 6.1). MnPP has two carboxyl groups and both could be coupled with the amine groups of the P22-xAEMA polymer. It is difficult to differentiate between the numbers of singly labeled carboxyl groups versus doubly labeled, and so, to minimize activation of both carboxyl groups on MnPP, a 1:1 molar ratio of EDC:NHS was added per MnPP. To investigate MnPP conjugation to the surface of P22 capsid, the reaction was also conducted on unpolymerized P22. After removal of excess MnPP and coupling agents, the concentration of protein and attached MnPP of the resulting materials (P22-xAEMA-MnPP or P22-MnPP) was determined by UV-VIS spectroscopy using known molar absorbtivities.

To determine the extent of non-covalent interactions between MnPP and the polymer and/or P22, both P22 and P22-xAEMA were incubated with MnPP (100x MnPP/subunit P22) in the absence of EDC/NHS. Successful attachment of the MnPP *via* EDC/NHS coupling was clear from the visible characteristics of the samples (Figure 6.2a) and confirmed spectroscopically when compared to the non-covalent interaction controls (Figure 6.2b, c). After purification by spin column, the P22-xAEMA-MnPP sample exhibited a UV-VIS spectrum (Figure 6.2c) in which the expected peaks for

MnPP at 365, 472, and 562 nm [222] were clearly visible, confirming the formation of P22-xAEMA-MnPP.

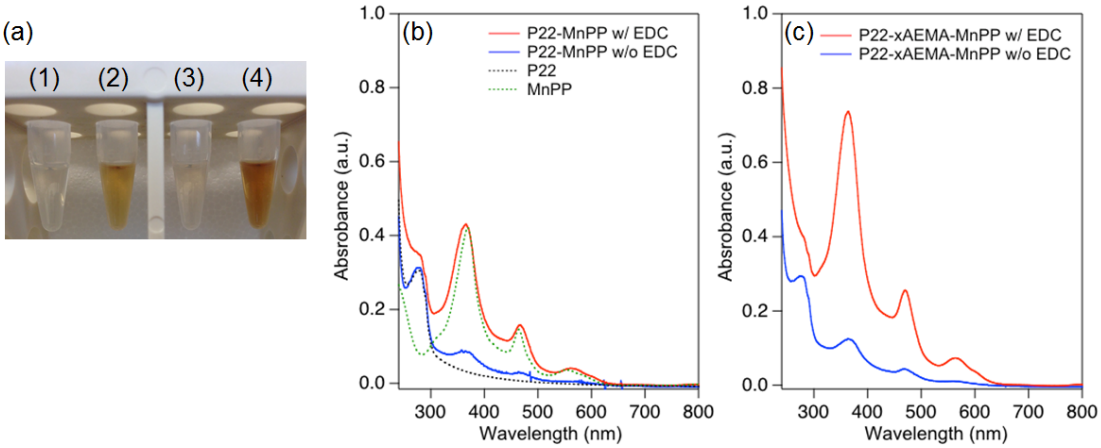

Figure 6.2: (a) Photos of each samples: (1) P22-MnPP w/o EDC, (2) P22-MnPP w/ EDC, (3) P22-xAEMA-MnPP w/o EDC and (4) P22-xAEMA-MnPP w/ EDC (1,200 MnPP/capsid). All 4 samples were incubated with 100x MnPP/subunit P22. Purification was performed using spin columns (twice) to remove unreacted manganese porphyrin from P22 and P22-xAEMA treated without (no color) and with (reddish color) EDC/NHS. UV-Visible spectra of (b) P22-MnPP w/ (red) and w/o (blue) EDC or (c) P22-xAEMA-MnPP w/ (red) and w/o (blue) EDC. Appearance of expected peaks for MnPP (green, dotted) show up at 365, 462, and 562 nm for both P22-MnPP and P22-xAEMA-MnPP with EDC/NHS (red) while peaks are less prevalent for controls without EDC/NHS (blue), and not at all for P22 (black, dotted).

Characterization

The MnPP loading per P22 capsid was determined for each of the constructs from their UV-VIS spectra. As shown in Appendix D, Table D1, the MnPP loading per capsid in the P22-xAEMA-MnPP ranged from 121 MnPP/capsid to 3,646 MnPP/capsid and was tunable based on molar excess of MnPP added per capsid during the reaction**.** Unpolymerized P22-MnPP resulted in 778 MnPP/capsid, the result of labeling endogenous lysines in the P22 capsid. There was some evidence of non-covalent

interactions between MnPP and P22, with loadings of 155 MnPP/capsid and 90 MnPP/capsid for P22-xAEMA-MnPP w/o EDC and P22-MnPP w/o EDC, respectively. All of the following characterization was done on 1,200 MnPP/capsid loading as a representative sample of P22-xAEMA-MnPP.

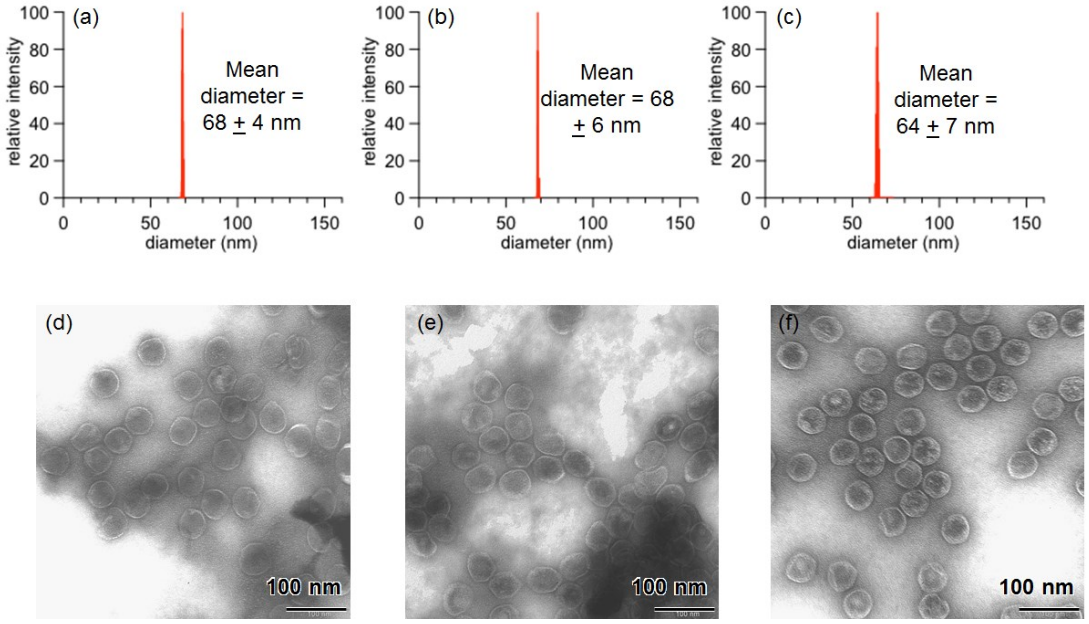

Figure 6.3: (a-c) Average diameters by dynamic light-scattering for P22 (a), P22-xAEMA (b), and P22-xAEMA-MnPP (1,200 MnPP/capsid) (c). The P22-xAEMA-MnPP construct retains its size, indicative of monodisperse population after conjugation of manganese (III) protoporphyrin IX. (d-f) Transmission electron microscopy images of P22 (a), P22-xAEMA (e), and P22-xAEMA-MnPP (1,200 MnPP/capsid) (f) shows that P22 maintains its overall morphology after conjugation to MnPP.

To confirm that the reaction with MnPP/EDC/NHS did not alter the morphology of the P22 *via* inter-particle cross-linking after EDC activation or aggregation, the size of the P22-xAEMA-MnPP was characterized. The hydrodynamic diameter, as measured by dynamic light scattering (DLS), remained essentially unchanged for the covalently-linked

MnPP samples (Figure 6.3a-c). Particle diameters 68 ± 6 nm (P22-xAEMA) and 64 ± 7 nm (P22-xAEMA-MnPP) were observed as compared to the unmodified P22 sample of 68 ± 4 nm, suggesting there was no inter-particle cross-linking mediated by the EDC reaction. When the particles were visualized by transmission electron microscopy (TEM), the morphology of the P22 appeared unchanged before and after the MnPP conjugation reaction (Figure 6.3d-f), further confirming that the cage-like structure of the P22 VLPs was unaffected by the coupling reaction. Analysis by SDS-PAGE (Figure 6.4) showed no appearance of new bands before (lane 3) and after (lane 4) modification of P22-xAEMA with MnPP. The streaking and appearance of higher molecular weight bands for P22-xAEMA (lane 3) compared to P22 (lane 2) is expected and indicative of formation of intra-particle subunit-subunit coupling due to polymer cross-linking on the interior of the capsid. Together these data suggest that the overall P22 morphology was unaffected after conjugation with MnPP.

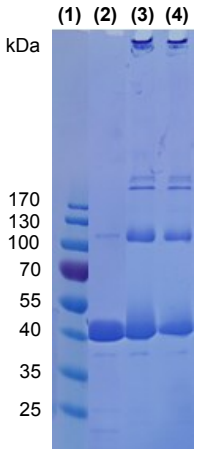

Figure 6.4: SDS-PAGE gel with marker (1), P22 (2), P22-xAEMA (3), and P22-xAEMA-MnPP (1,200 MnPP/capsid) (4).

NMR and (T_1 and T_2) Relaxivity

We investigated T_1 relaxivity as a function of MnPP loading on a per Mn basis ($r_{1,ionic}$) and per P22 capsid basis ($r_{1,particle}$), over a range of loadings from 90 to 3,646 MnPP/capsid at 2.1 Tesla (90 MHz). The loading factor appeared to have almost no impact on $r_{1,ionic}$ relaxivity, which remained below 5 $mM^{-1} \cdot s^{-1}$ across the range of loadings (Figure 6.5a). However, the $r_{1,particle}$ increased with loading factor and the high loading capacity of the MnPP/capsid compensates for lower ionic relaxivities, with the highest observed $r_{1,particle}$ = 7,100 $mM^{-1} \cdot s^{-1}$ for this system (Figure 6.5b).

The $r_{2,ionic}$ relaxivity was also evaluated for this system and was observed to have an inverse relationship with the MnPP loading factor (Figure 6.5a). The $r_{2,ionic}$ relaxivity decreased significantly with increasing MnPP loading factor at lower loading and gradually leveled off at higher loading. A similar phenomenon has been reported in an investigation of $r_{2,ionic}$ relaxivity at the initial stages of iron uptake in ferritin [226]. In this paper, it is proposed that $r_{2,ionic}$ relaxivity decreases with increasing Fe loading factor due to the formation of antiferromagnetically coupled clusters. Similarly in our P22 system there may be more MnPP clusters at higher loading factors that can couple antiferromagnetically and which decrease the overall $r_{2,ionic}$ relaxivity of the sample. The negative impact of antiferromagnetic coupling could also affect $r_{1,ionic}$ relaxivity [227], but we did not see a corresponding decrease in $r_{1,ionic}$ relaxivity across the MnPP loading range we examined. This phenomenon could be interesting to explore further in the future.

At lower loadings, the sample exhibits high r_2/r_1 (see Appendix D, Table D1), suggesting that this system could potentially be used as a T_2-enhanced contrast agent. However, at higher loadings, r_2/r_1 approaches 1, thus shifting toward a T_1-enhanced contrast agent. Therefore, P22-xAEMA loaded with MnPP can be tuned to be either a T_1 or T_2 contrast agent by controlling the loading factor.

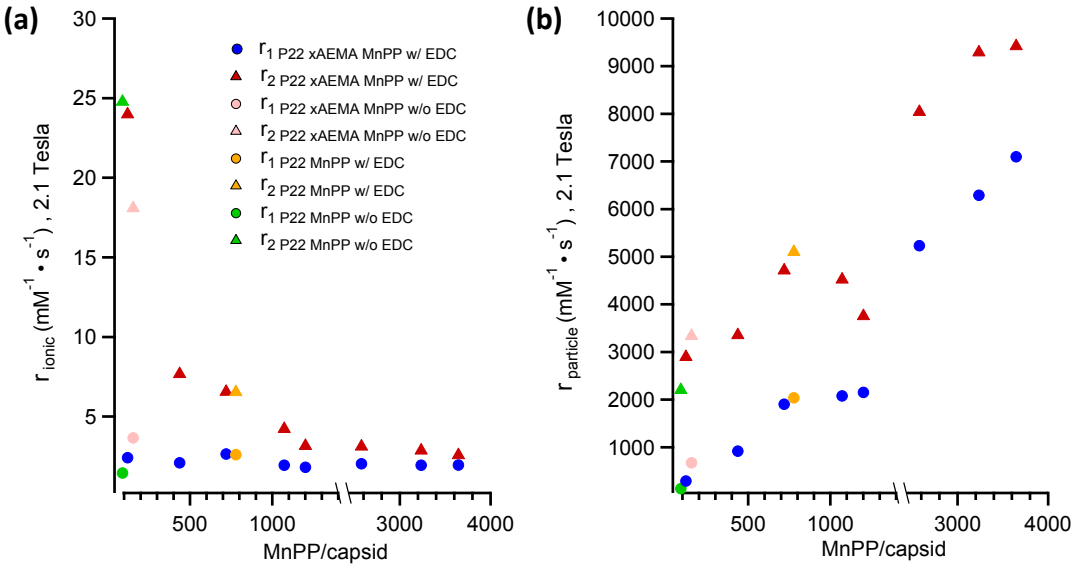

Figure 6.5: Ionic (a) and particle (b) relaxivities r_1 (blue circles) and r_2 (red triangles) of P22-xAEMA-MnPP at different loadings of MnPP, ranging from 121 to 3,646 MnPP/capsid, with P22-xAEMA-MnPP w/o EDC (155 MnPP/capsid) represented in pink, P22-MnPP w/ EDC (778 MnPP/capsid) represented in orange, and P22-MnPP w/o EDC (90 represented in green. Loading has no impact on $r_{1,ionic}$, which remains below 5 $mM^{-1} \cdot s^{-1}$, while $r_{2,ionic}$ dramatically decreases as loading increases.

Based on the Solomon−Bloembergen−Morgan (SBM) analytical model for understanding paramagnetic relaxivity [183; 184; 228-230] we expected that the $r_{1,ionic}$ relaxivity would be enhanced after conjugation of MnPP to the macromolecular P22 capsid [108; 225; 231]. But contrary to expectations we did not observe an enhancement. The SBM model

predicts that the relaxivity is dominated by three important parameters: the number of metal-bound water molecules (q), the mean residence lifetime for metal-bound water (τ_M), and the rotational correlation time (τ_R). We, and others, have effectively used this model to predict and design new contrast agents that optimize these important parameters [25; 51; 108]. Both τ_R and τ_M of free MnPP (τ_R = 50 - 80 ps, τ_M = 10 ns) [232] are comparable to free Gd-DTPA (τ_R = 70 ps, τ_M = 16 ns) [108]. We have shown previously that conjugating a Gd-DTPA to a similar P22-polymer system does not alter τ_M of the small molecule contrast agent [108] significantly, but does dramatically alter τ_R. Thus, we assumed the same τ_R for the P22-xAEMA-MnPP system and assumed that τ_M would be similar to that of free MnPP. The nuclear magnetic dispersion profile (NMRD) for MnPP conjugated to a large particle, such as the P22-xAEMA particle (τ_R around 10 ns) [51; 108], is predicted to have enhanced relaxivity at low field (20 MHz) [115]. Thus, the ionic relaxivity of P22-xAEMA-MnPP (see Appendix D, Table D1), was measured at 0.45, 2.1, and 7 Tesla (19, 90, and 300 MHz) (Figure 6.6) with the expectation that we would see a relaxivity enhancement, particularly at 0.45 T (19 MHz). For comparison, the relaxivity of free MnPP at 14.5mM was also measured. The concentration of free MnPP was based on local concentration of MnPP in the P22-xAEMA capsid, i.e. the volume of the spherical 64 nm P22 and number of Mn encapsulated as the P22-xAEMA-MnPP construct (1,200 MnPP / capsid). The results show that the relaxivity changes only slightly across field strengths, and not as significantly as expected based on NMRD profiles of other macromolecular Mn-complexes [115; 233] and our previous work with macromolecular Gd-based agents [108].

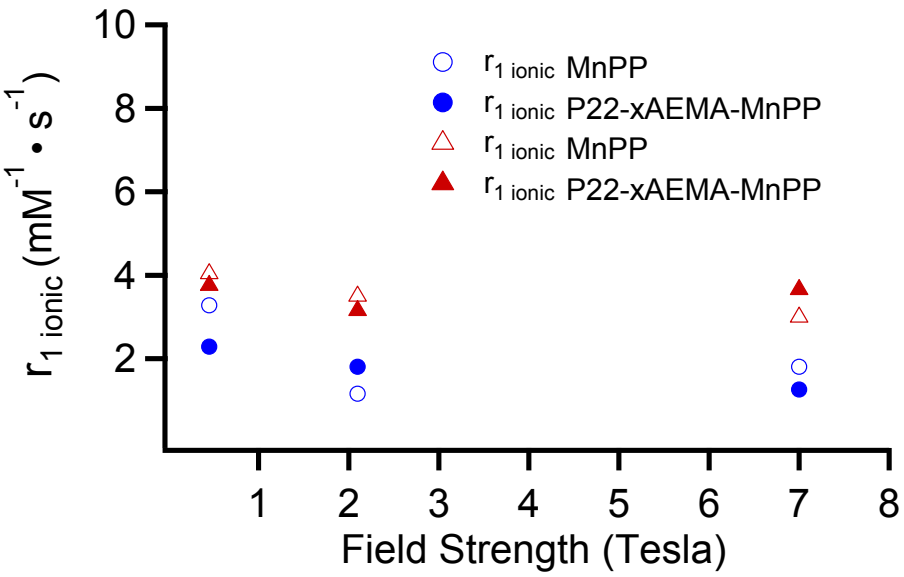

Figure 6.6: Ionic relaxivities r_1 (blue circles) and r_2 (red triangles) of P22-xAEMA-MnPP at 1,200 MnPP/capsid (closed) and free MnPP (open) at 14.5 mM (the same local concentration of its P22-xAEMA-MnPP counterpart, see Appendix D, Table D1) at three different field strengths of 0.45, 2.1, and 7 Tesla. The trend shows relatively small changes in relaxivity across field strengths.

In order to understand why no increase in $r_{1,ionic}$ relaxivity was observed for MnPP after conjugation to P22 VLPs as compared to free MnPP, we explored interactions between MnPPs further. The presence of intermolecular MnPP interactions could structurally block water access to the manganese ion, resulting in a lower effective q and thus a diminished $r_{1,ionic}$ relaxivity [232]. This clustering of MnPPs could account for the observed lack of $r_{1,ionic}$ relaxivity enhancement for P22-xAEMA-MnPP, when compared to free MnPP. We conducted the following two experiments to explore this possibility.

Imidazole Titration Experiments

To probe the effects of water access to the Mn ion on the relaxivity, we titrated free MnPP with imidazole, which is expected to bind the axial sites in MnPP and compete for water access. This competitive binding experiment was monitored by both changes in the optical spectrum and changes in the ionic relaxivity. Figure 6.7A and Appendix D, Figure D2 show the changes in the UV-VIS spectrum of MnPP upon titration with imidazole [234]. At 640 μM MnPP, imidazole was added at a in a range up to 1000 molar excess per MnPP. The UV-VIS spectrum shows an emerging peak at 482 nm, which increased with increasing imidazole, clearly indicating interactions between the imidazole and the MnPP complex (Appendix D, Figure D2). We further investigated the effects of imidazole binding to MnPP by measuring the ^{1}H relaxivity at 2.1 T (90 MHz) at a range of added imidazole concentrations. We found an inverse relationship between the change in absorbance at 482 nm (imidazole binding to MnPP) and the measured relaxivity (Figure 6.7B). This is consistent with imidazole binding to both axial sites on the MnPP at high imidazole concentrations, where these sites are essentially saturated and the effective value of q approaches 0. Thus, imidazole appears to influence intermolecular MnPP interactions and blocks water access, which has a clear, dominant influence on the relaxivity.

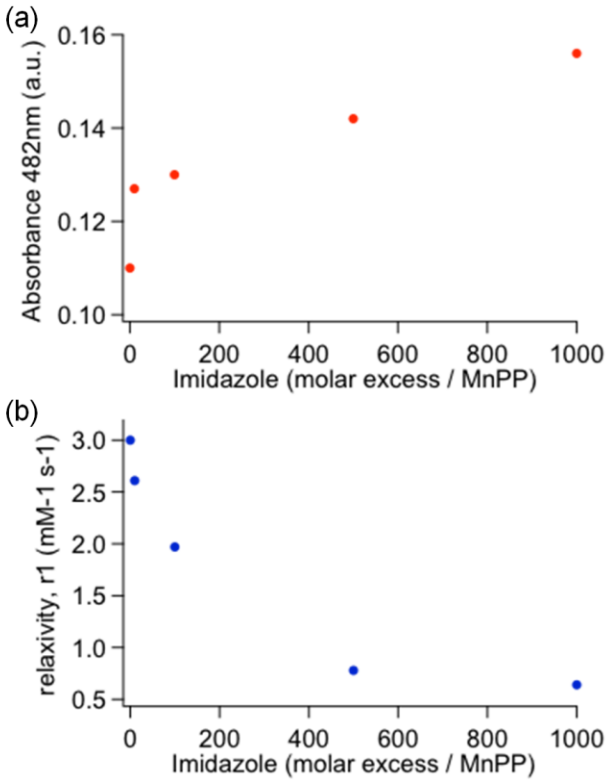

Figure 6.7: UV-VIS, absorbance at 482 nm (a) and $r_{1,ionic}$ relaxivity at 2.1 Tesla (90 MHz) (b) measurements were taken at 0, 10, 100, 500, and 1000 equivalents of added imidazole to 640 μM MnPP. There is an inverse relationship between increase in absorbance at 482 nm due to imidazole binding to MnPP and decrease in relaxivity. Even at 10 equivalents of imidazole a significant difference in relaxivity was observed.

D6-Acetone

In an attempt to disrupt intermolecular interactions between neighboring MnPPs and potentially increase water access and therefore the number of bound and exchangeable waters (q), we investigated the effects of adding acetone on the $r_{1,ionic}$ relaxivity of free MnPP at concentrations based on the same local concentration of MnPP in our P22-xAEMA-MnPP system. First, $r_{1,ionic}$ relaxivity of MnPP and P22-xAEMA-MnPP were investigated at 2.1 Tesla (90 MHz). MnPP and P22-xAEMA-MnPP exhibited

similar $r_{1,ionic}$ values at all concentrations, with free MnPP having slightly smaller $r_{1,ionic}$ values than P22-xAEMA-MnPP (Figure 6.8). Second, $r_{1,ionic}$ relaxivity of MnPP in the presence of 20 % or 60 % D6-acetone was measured. These experiments were conducted only as a proof of concept, as acetone is neither a suitable solvent for protein stability nor for *in-vivo* applications. The free MnPP was treated with D6-acetone to disperse the MnPPs and observe the impact on relaxivity (Figure 6.8). After treating free MnPP with 20 % D6-acetone, the ionic relaxivities did not show significant change, with only slight increase in relaxivity at the lower MnPP concentrations. However, with 60 % D6-acetone, a dramatic increase in ionic relaxivity was observed at all concentrations, with a trend toward highest increase in relaxivity for the lowest concentration of MnPP. This data correlates well with published data [232] and indicates that the acetone disrupts intermolecular MnPP interactions, resulting in a greater water exchange at the manganese centers and an increase in the effective value of q. Extrapolation from these data suggest that the high local concentrations of MnPP inside the P22-xAEMA-MnPP probably results in strong intermolecular interactions between neighboring MnPPs, resulting in a lower observed ionic relaxivity compared to when the interactions are disrupted, as in the case of free MnPP in the presence of acetone. This result implies that we could increase ionic relaxivity of MnPP by disrupting inter-molecular interactions between MnPPs. For example, modification of the porphyrin moiety, in a manner analogous to the designed picket-fence porphyrins [235], could minimize MnPP interaction.

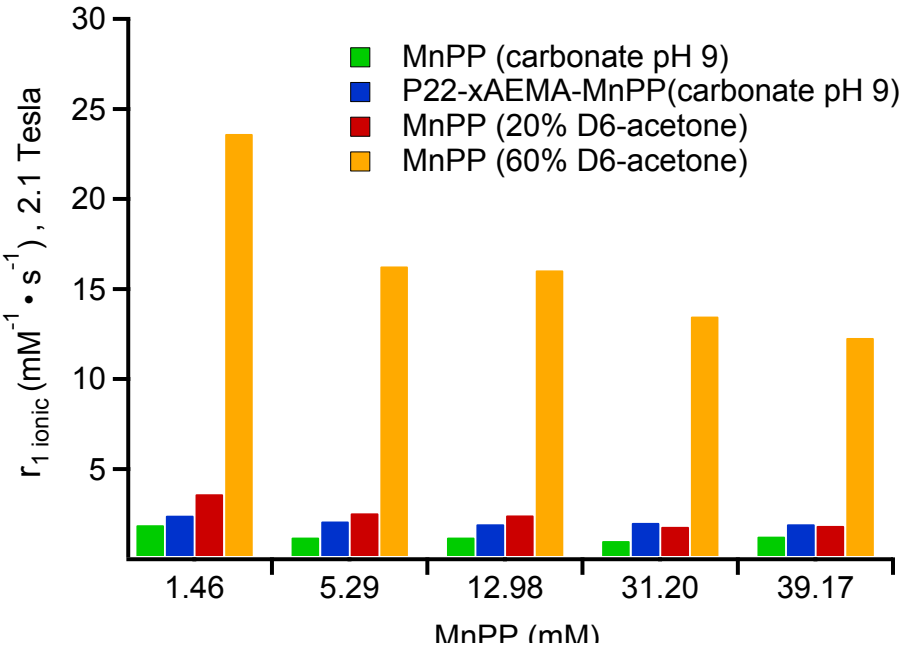

Figure 6.8: Ionic relaxivities at different concentrations of free MnPP compared to P22-xAEMA-MnPP in carbonate pH 9 buffer (See Table S1 for corresponding loading factors). The free MnPP was further treated with either 20% or 60% D6-acetone to try to disperse MnPPs and see impact of acetone on relaxivity. MnPP (green) at same local concentrations of MnPP for P22-xAEMA-MnPP (blue) exhibit similar $r_{1,ionic}$ values, with free being slightly smaller P22-xAEMA-MnPP. After treating free MnPP with 20% D6-acetone (red), the ionic relaxivities did not change much, only increasing slightly for the lower concentrations. At 60% D6-acetone (orange), a dramatic increase in ionic relaxivity was observed at all concentrations, with a trend toward highest increase in relaxivity for lowest concentration of MnPP.

Conclusion

In summary, we have covalently encapsulated a large number of MnPP inside P22 VLP-polymer hybrids and demonstrated potential for this construct as a tunable MRI contrast agent. This system could be a good alternative to gadolinium-based contrast agents, which are known to be linked to nephrogenic systemic fibrosis. We can conjugate more MnPP to P22-xAEMA versus P22 alone, using simple EDC/NHS to chemically introduce MnPP to the P22 capsid up to 3,646 MnPP/capsid. The improvement in

labeling is important for the delivery of contrast agents on a per-particle basis, allowing for high concentration delivery of the contrast agent. Although we do not see an improvement in $r_{1,ionic}$ relaxivity, the high per-particle relaxivity of the P22-xAEMA-MnPP, resulting from high loading density, could be beneficial when these particles are imparted with targeting cell capabilities. Our results suggest that we could also increase $r_{1,ionic}$ relaxivity of MnPP by disrupting inter-molecular interactions between MnPPs. In future design iterations of these hybrid materials we might overcome intermolecular interactions of MnPPs by altering the porphyrin moiety to minimize MnPP interactions [235]. Alternatively, incorporation of other Mn-porphyrins, which have larger $r_{1,ionic}$ relaxivity, such as Mn-TPPS, [232; 236; 237], may enable us to more fully utilize the advantages of the P22-polymer platform.

Experimental

All materials were analytical grade and purchased from either Sigma-Aldrich or Fisher Scientific and used as received unless otherwise noted. All water was deionized by use of a NANOpure water purification system. All protein samples that have been chemically modified were analyzed *via* UV-VIS (UV-Vis; Model 8453, Agilent, Santa Clara, CA) and dynamic light-scattering (DLS; 90Plus particle-size analyzer, Brookhaven Instrument, Holtsville, NY). The synthesis of 2-bromoisobutyryl aminoethyl maleimide has been reported [225]. The manganese (III) protoporphyrin IX chloride was purchased from Frontier Scientific.

Mutagenesis, Protein Purification,
and P22-xAEMA Formation

The P22 (S39C) point mutation was made with established polymerase chain-reaction protocols (Agilent) with pET-11a-based plasmids encoding genes for scaffolding and coat protein. The amplified DNA was transformed into *E. coli* strain BL21 (DE3) and selected for ampicillin resistance [225]. P22 (S39C) procapsid (PC), made up of 420 subunits, was produced by a heterologous expression system in *E. coli.* and purified by a previously described procedure [108]. The resulting virus pellet, after purification, was resuspended in 100 mM sodium phosphate, 50 mM NaCl, pH 7.0, and spun at 17,000 rpm for 20 minutes to remove particulates and lipid. The PC was heat treated for 20 min at 65 ˚C to transform the protein into its expanded (EX) form as previously described and analyzed [83]. The EX samples were purified by pelleting *via* centrifugation at 45,000 rpm for 50 minutes in an ultra-centrifuge (Sorvall), followed by resuspension into 100 mM sodium phosphate, 50 mM NaCl, pH 7.6 in preparation for protein labeling. The EX was labeled with an ATRP initiator molecule and cross-linked AEMA polymer (P22-xAEMA) was synthesized inside the P22 VLP cavity, as previously described [238]. P22 procapsid (PC), expanded (EX), and polymerized (P22-xAEMA) samples were characterized with SDS-PAGE, transmission electron microscopy (TEM, Leo 912 AB), and dynamic light scattering (DLS, Brookhaven 90Plus, Brookhaven, NY) [225]. The protein concentration was determined by absorbance at 280 nm where an extinction coefficient (65,920 M^{-1} cm^{-1}, subunit P22) was used. As described above, EX form of P22 was exclusively used for P22-xAEMA formation, and hereafter, we will refer to unpolymerized EX form of P22 as P22 and polymerized P22 as P22-xAEMA. All further

labeling experiments with P22 and P22-xAEMA and sample analysis were conducted in sodium bicarbonate buffer (100 mM sodium bicarbonate, 50 mM NaCl, pH 9.0) because MnPP is more soluble in this buffer than in phosphate buffer at neutral pH.

Manganese (III) Protoporphyrin IX Labeling
Conditions (MnPP) – without EDC/NHS

P22 and P22-xAEMA were labeled with MnPP without the presence of 1-ethyl-3-(3-dimethylaminopropyl)carbodiimide (EDC) and N-hydroxysuccinimide (NHS). First, a 30 mM stock solution of MnPP was made up in DMSO and vortexed until completely dissolved. From the 30 mM MnPP stock solution, 72 μL (1.40 mg, 2.14 μmoles) MnPP was diluted with 144 μL water. Next, to 284 μL of P22 or P22-xAEMA (0.0214 μmoles subunit, 3.5 mg/mL, 100 mM sodium carbonate buffer, 50 mM NaCl, pH 9.0), 216 μL of diluted MnPP was added dropwise (100x MnPP/subunit of P22, i.e. 42,000x MnPP/capsid of P22) while vortexing the protein solution. The mixture was allowed to react for 1 hr at room temperature followed by purification away from excess MnPP/EDC/NHS with a Micro Bio-Spin column (Bio-Rad, Hercules, CA) twice, resulting in 90 MnPP/capsid (67.7 % yield) and 184 MnPP/capsid (71.8 % yield), respectively.

Manganese (III) Protoporphyrin IX Labeling
Conditions (MnPP) – with EDC/NHS

Various loadings of MnPP per P22-xAEMA (121 to 3,646 MnPP/capsid) were achieved by using ranging molar excess from 1 to 100 MnPP/subunit P22. The following describes preparation of 100 molar excess MnPP/subunit P22. To prepare P22-MnPP and P22-xAEMA-MnPP with EDC/NHS, a 1:1:1 molar ratio of MnPP:EDC:NHS was made

by adding 72 μL (30 mM in DMSO, 1.40 mg, 2.14 μmoles) MnPP to a solution of 72 μL EDC (30 mM in water, 0.25 mg, 2.14 μmoles) and 72 μL NHS (30 mM in water, 0.41 mg, 2.14 μmoles) and stirred for 15 min at room temperature to activate carboxyl groups on MnPP. To 284 μL P22 or P22-xAEMA (0.0214 μmoles subunit, 3.5 mg/mL, 100mM sodium carbonate buffer, 50 mM NaCl, pH 9.0), 216 μL of MnPP/EDC/NHS mixture was added dropwise while vortexing the protein solution. The mixture was allowed to react for 1 hr at room temperature followed by purification away from excess MnPP/EDC/NHS by use of a spin column twice, resulting in 780 MnPP/capsid (82.0 % yield) and 1,200 MnPP/capsid (92.3 % yield), respectively. It should be noted that amount of labeling varies when experiment is repeated at same molar excess (i.e for molar excess of 100 MnPP/subunit P22, labeling ranges from 1,200-3,646 MnPP/capsid). All NMR data is based on the output, which is labeling amount of MnPP/capsid.

Sample Analysis

P22 and P22-xAEMA samples and those with MnPP were analyzed by a variety of methods aimed at interrogating the purity, morphology, and composition of the samples. P22, P22-xAEMA, and P22-xAEMA-MnPP were imaged by transmission electron microscopy (Leo 912 AB, 100 kV) by negatively staining the sample with 1 % uranyl acetate on Formvar carbon coated grids. These samples were also analyzed with SDS-PAGE on 10-20 % gradient Tris-glycine gels (Lonza). Protein was detected by staining with Coomassie blue.

Protein and Manganese Concentration

Protein concentrations of P22 and P22-xAEMA samples were determined by absorbance at 280 nm (extinction coefficient: 65490 $M^{-1} \cdot cm^{-1}$, subunit P22). The protein concentration for P22-xAEMA-MnPP samples was determined by absorbance at 280 nm after the contribution from manganese porphyrin (extinction coefficient: 19.82 $mM^{-1} \cdot cm^{-1}$) was subtracted. The amount of MnPP conjugated with P22 VLPs was determined using an extinction coefficient of 25 $mM^{-1} \cdot cm^{-1}$ at 462 nm [239].

Relaxivity Measurements

T_1 and T_2 measurements were carried out on a broadband 19 MHz (0.447 T) vertical NMR spectroscopy system, Anasazi FT-NMR 90 MHz (2.1 T) and Bruker DPX 300 MHz (7.0 T) spectrometers. Each P22-xAEMA-MnPP sample was diluted with 67 % D_2O in H_2O to yield a dilution series. The longitudinal relaxation rate constant (T_1) was measured at each dilution by use of an inversion recovery pulse sequence and the transversal relaxation rate constant (T_2) was measured by use of a Carr-Purcell-Meiboom-Gill (CPMG) sequence at 298 K, where the relaxation delay was set to six times the estimated T_1 or T_2. For 19 MHz (0.447 T), recovery times of 30 s were used for T_1 relaxation times. Figure D1 shows a plot of $1/T_1$ versus [Mn] (mM) for the 3 dilutions which was used to determine relaxivity values ($r_{1,ionic}$), where ionic relaxivity (relaxivity per Mn) is equal to the slope of the line, and particle relaxivity (relaxivity per P22) was calculated by multiplying the slope by Mn/capsid. Similarly, a plot of $1/T_2$ versus [Mn] (mM) was used to determine and $r_{2,ionic}$ relaxivity values.

Imidazole Titration Experiments
to Block Water Access to MnPP

In order to assess the influence of water accessibility on $r_{1,ionic}$ relaxivity of MnPP, we titrated free MnPP with imidazole. Imidazole was dissolved in carbonate buffer (100 mM sodium carbonate, 50 mM NaCl, pH 9.0) to create a stock solution of 10 M, which was added to 640 μM free MnPP in molar equivalents of 0, 10, 100, 500, or 1000 excess to give a final manganese concentration of 390 μM. Samples were further characterized *via* UV-VIS spectrometer with a 40x dilution. T_1 relaxivity of the samples was measured as described above.

Addition of Acetone to Disrupt
Inter-Molecular Interactions of Free MnPP

In order to evaluate the potential effect of MnPP aggregation within P22 capsid on $r_{1,ionic}$ relaxivity, we compared free MnPP in solution versus MnPP conjugated to P22-xAEMA at the same concentration. The concentration of free MnPP was based on local concentration of MnPP in the P22-xAEMA capsid, i.e. the volume of the spherical 64 nm P22 and number of Mn encapsulated as the P22-xAEMA-MnPP construct. Free MnPP was prepared in different concentrations, from 1.46 - 39.17 mM MnPP for P22-xAEMA-MnPP at loadings ranging from 121-3646 MnPP/capsid (100 mM sodium carbonate, 50 mM NaCl, pH 9.0). In addition, in order to evaluate the effect of disrupting inter-particle interactions between MnPPs, we treated free MnPPs with two different concentrations of acetone, and measured $r_{1,ionic}$ relaxivity. At all concentrations of MnPP, deuterated acetone was added to achieve a final matrix of 60 % D6-acetone, 33.33 % H2O and 6.67 % D2O or 20 % D6-acetone, 33.3 3% H2O and 46.67 % D2O. For 60 % D6-acetone, 252

μL deuterated acetone (99.5 %-d) was added to 140 μL of MnPP and 28 μL of D2O. For 20 % D6-acetone, 84 μL deuterated acetone (99.5 %-d) was added to 140 μL of MnPP and 196 μL of D2O. This was further diluted with corresponding matrix to yield a dilution series of 1:3, 1:9, and 1:27. T_1 relaxivity was measured as described above in the relaxivity measurements section.

CHAPTER 7

EXPRESSION AND BIOPHYSICAL CHARACTERIZATION OF RGD TARGETING PEPTIDE ON SURFACE OF P22 VIA C-TERMINUS EXTENSION OF DEC AND P22 COAT PROTEIN

Contributions of Authors and Co-Authors

Manuscript in Chapter 7

Author: Shefah Qazi

Contributions: Designed and carried out the experiments and wrote the manuscript.

Co-author: Masaki Uchida

Contributions: Designed and carried out the experiments and wrote the manuscript.

Co-author: Hisanori Kosuge

Contributions: Conducted in-vivo mouse experiments.

Co-author: Michael V. McConnell

Contributions: Obtained funding, coordinated the project, and assisted with the design of the experiments.

Co-author: Trevor Douglas

Contributions: Obtained funding, coordinated the project, and assisted with the design of the experiments. Discussed the results and edited the manuscript at all stages.

Manuscript Information Page

Authors: Shefah Qazi, Masaki Uchida, Hisanori Kosuge, Michael V. McConnell, and Trevor Douglas
Journal: X
Status of the manuscript:
_X_ Prepared for submission to a peer-reviewed journal
____ Officially submitted to a peer-reviewed journal
____ Accepted by a peer-reviewed journal
____ Published in a peer-reviewed journal

Publisher X

CHAPTER 7

EXPRESSION AND BIOPHYSICAL CHARACTERIZATION OF RGD TARGETING PEPTIDE ON SURFACE OF P22 VIA C-TERMINUS EXTENSION OF DEC AND P22 COAT PROTEIN

Published: *in process*, **2014**, x, x-x.

Shefah Qazi,[†] Masaki Uchida,[†] Hisanori Kosuge,[€] Michael V. McConnell,[€] and Trevor Douglas[†,§]

[†]Chemistry and Biochemistry Department, Montana State University, Bozeman, Montana, 59717, USA
[€]Division of Cardiovascular Medicine, Stanford University School of Medicine, Stanford, California, 94305, USA
[§]Department of Chemistry, Indiana University, Bloomington, Indiana, 47405, USA

Abstract

Targeting peptides for integrins expressed on cell surfaces or for specific cellular compartments have been extensively used to direct the location of protein cage platforms. Targeting allows for the localization of an imaging agent or drug. In recent years, it has become evident that understanding the biological activity of plaque formation provides insight into disease progression. Novel multifunctional molecular imaging probes that target macrophage-rich atherosclerotic plaque have potential for translation into clinically usable agents. RGD-based peptides have been shown to bind to the murine and human integrin αvβ3, which is upregulated in activated macrophages and angiogenic endothelial cells. Two different approaches have been explored for incorporating RGD peptides on the surface of P22 virus-like particles (VLPs). The first approach is expression of the peptide (GGGRGDGGG) onto a phage decoration protein (Dec), which has recently been shown to have a high binding affinity to P22 coat protein. The second approach is to insert RGD as an extension to the C-terminus of coat protein (CP) of P22 VLPs, which we are able to modify without disrupting capsid assembly or stability. Here, we show successful expression of the RGD peptide in our two proposed methods along with biophysical characterization of the two constructs. The ability to deliver targeted agents to the vessel wall will significantly enhance sensitivity of imaging, lower dosage of imaging probe to reduce toxicity, and result in earlier diagnosis and treatment of disease.

Introduction

Atherosclerosis, or "hardening of the arteries," occurs when cholesterol and scar tissue build up, forming a substance called plaque inside the arteries that narrows and clogs the arteries, causing decreased blood flow. Because atherosclerosis is a systemic disease, people are likely to have blocked arteries in multiple areas of the body. These people are at increased risk for heart disease, aortic aneurysm, peripheral arterial disease, stroke, renal hypertension, and kidney failure. Atherosclerosis, the main contributor to cardiovascular disease, is the leading cause of death world-wide [240; 241]. In recent years, it has become evident that understanding the biological activity of plaque formation provides insight into disease progression.[242; 243] Novel multifunctional molecular imaging probes that target macrophage-rich atherosclerotic plaque, developed for *in vivo* mouse model systems, have potential for translation into clinically usable agents.[244-246]

RGD-based peptides have been shown to bind to the murine and human integrin αvβ3, which is upregulated in activated macrophages and angiogenic endothelial cells.[247-250] Two different approaches have been explored for incorporating RGD peptides on the surface of P22 virus-like particles (VLPs). The first approach is expression of the peptide (GGGRGDGGG) onto a phage decoration protein (Dec), which has recently been shown to have a high binding affinity to P22 coat protein.[251] The second approach is to insert RGD as an extension to the C-terminus of coat protein (CP) of P22 VLPs, which we are able to modify without disrupting capsid assembly or stability (Figure 7.1).

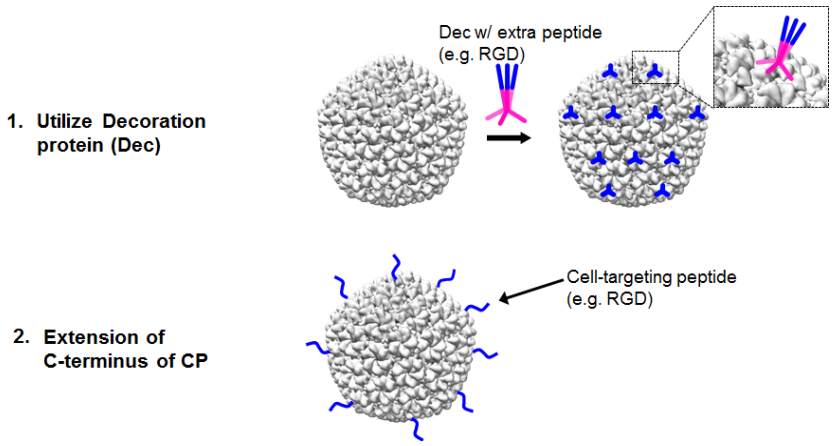

Figure 7.1: Two methods for incorporation of targeting peptide to exterior surface of P22.

A common feature in the assembly process of several virus particles is the presence of proteins that "decorate" their coat protein shell.[70] Decoration proteins are small semi- or non-essential proteins that bind to the surface of mature virus coat protein shells, often times to stabilize those shells. P22 bacteriophage does not have any intrinsic decoration proteins, however, bacteriophage L, a close relative of P22 bacteriophage,[252] has a gene which encodes for a decoration protein, termed Dec. Dec is a homotrimeric decoration protein complex which is present on the surface of bacteriophage L in about 180 molecules/capsid.[253]

It has been shown that Dec binds similarly to mature P22 virions (also applicable to P22 expanded and wiffleball capsid) in a highly symmetric fashion at the quasi three-fold sites, generating several hundred new binding sites on the surface of P22 bacteriophage. [253; 254] To determine the location of both termini of Dec, the protein was modified with a hexa-histidine tag at either N- or C-terminus and bound to P22 wiffleball, and further labeled with gold beads. Icosahedrally-averaged cryo-reconstructions were computed from images of P22 bound to Dec along with difference

map analysis. The image of the bound gold beads revealed location of N- and C- terminus of Dec, showing that the c-terminus of Dec is an ideal location for insertion of a targeting peptide. It was found that Dec trimers bind to 60 sites at the quasi-three-fold axis, between the hexons, providing a total of 180 binding sites for cargo (Figure 7.2). [251]

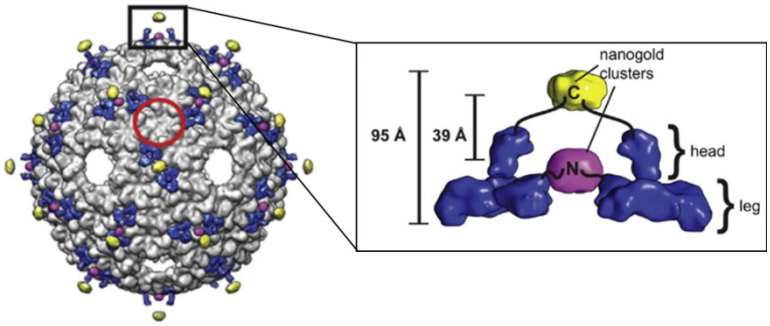

Figure 7.2: P22 wiffleball was labeled with Dec-N-his and Dec-C-his (His 6x-tag), bound to gold beads (nanogold nanoclusters). The location of N- and C-terminus of Dec was determined via icosahedral-averaged cryo-reconstructions along with difference map analysis. P22 wiffleball with Dec trimers bound at the quasi-three-fold-axis (black box) and not at the strict-three-fold-axis (red circle). Although, at high molar excess (30 M Dec), it has been shown that about 20 Dec trimers bind to the strict-three-fold-axis at low binding affinity. Black box: zoom in of Dec trimers showing N- (purple) at leg of Dec, close to capsid surface and C- (yellow) terminus at head of Dec, exposed about 96 A away from surface of capsid. Image adapted from Parent et. al (2012).[251]

Existing cryo-electron microscopy-based models suggest that the C-terminus of the bacteriophage P22 coat protein (CP) extends toward the capsid exterior. [76; 77] Biochemical analysis through genetic manipulations of the C-terminus supports the model where the CP C-terminus is exposed on the exterior of the P22 capsid. Capsids displaying a 6xHis tag appended to the CP C-terminus bind to a Ni affinity column, and the addition of positively or negatively charged coiled coil peptides to the capsid results in association of these capsids upon mixing. Additionally, a single cysteine appended to the CP C-terminus results in the formation of intercapsid disulfide bonds and can serve as

a site for chemical modifications.[255] Thus, the C-terminus is a powerful location for multivalent display of peptides.

An additional advantage of modifying P22 C-terminal for targeting peptide expression is that we will have a way to add multiple targeting ligands to P22 VLPs in a controlled manner, one via C-terminal expression and another via Dec binding. This gives us room to play with different combinations of targeting ligands and their effects *in-vitro* and *in-vivo*. The ability to deliver targeted agents to the vessel wall will enhance our ability to image atherosclerotic plaque regions, and ultimately lower contrast agent dosage administration reducing the risk of toxicity associated with gadolinium (i.e. NSF).

Results and Discussion

Characterization of Dec-RGD and P22 (S39C) C-terminal RGD

Two mutants, Dec-RGD and P22 (S39C) C-terminal RGD were successfully engineered for this study by introducing the RGD-2C peptide (CRGDCG) to the C-terminus of wt. Dec (Dec-RGD) and to the C-terminus of P22 (S39C). Both mutants as well as wt. Dec were heterologously expressed in *E. coli*. Wt. Dec and Dec-RGD were secreted extracellularly. Therefore they were purified from cell culture supernatant with a Ni-NTA column (Appendix E, Figure E1). Typical yield of wt. Dec and its mutants were about 20 mg from 300 mL of cell culture supernatant. Denaturing sodium dodecyl sulfate polyacrylamide gel electrophoresis (SDS-PAGE) assay of the purified proteins showed stained bands consistent with expected molecular weight of Dec proteins without any other visible impurity bands (Figure 7.3a). Similarly, bands for coat protein and truncated

scaffold protein of P22 (S39C) C-terminal RGD were consistent with expected molecular weights (Appendix E, Figure E2a). Additionally, the procpasid of P22 (S39C) C-terminal RGD was heat treated to 65C and 75C to produce expanded shell and wiffleball morphologies. A native agarose gel showed bands shifted for heat treated constructs, indicative of successful transformation (Appendix E, Figure E2b).

Further characterization with mass spectrometry observed subunit mass of wt. Dec and Dec-RGD to be 15565.7 Da and 16413.9 Da, which matched well with the predicted mass of 15565.92 Da and 16415.83 Da, respectively (Figure 7.3b). It should be noted that despite Dec-RGD possesses two cysteine residues in its RGD-2C peptide sequence, it exhibited only minor peak of subunit dimmer even without adding TCEP, suggesting that most of the protein forms inter subunit disulfide bond and the RGD-2C peptide is cyclized. Mass spectrometry analysis of P22 (S39C) C-terminal RGD showed an observed mass of 47486.2 Da, which matched closely with the predicted mass of 47486.6 Da (Appendix E, Figure E2c).

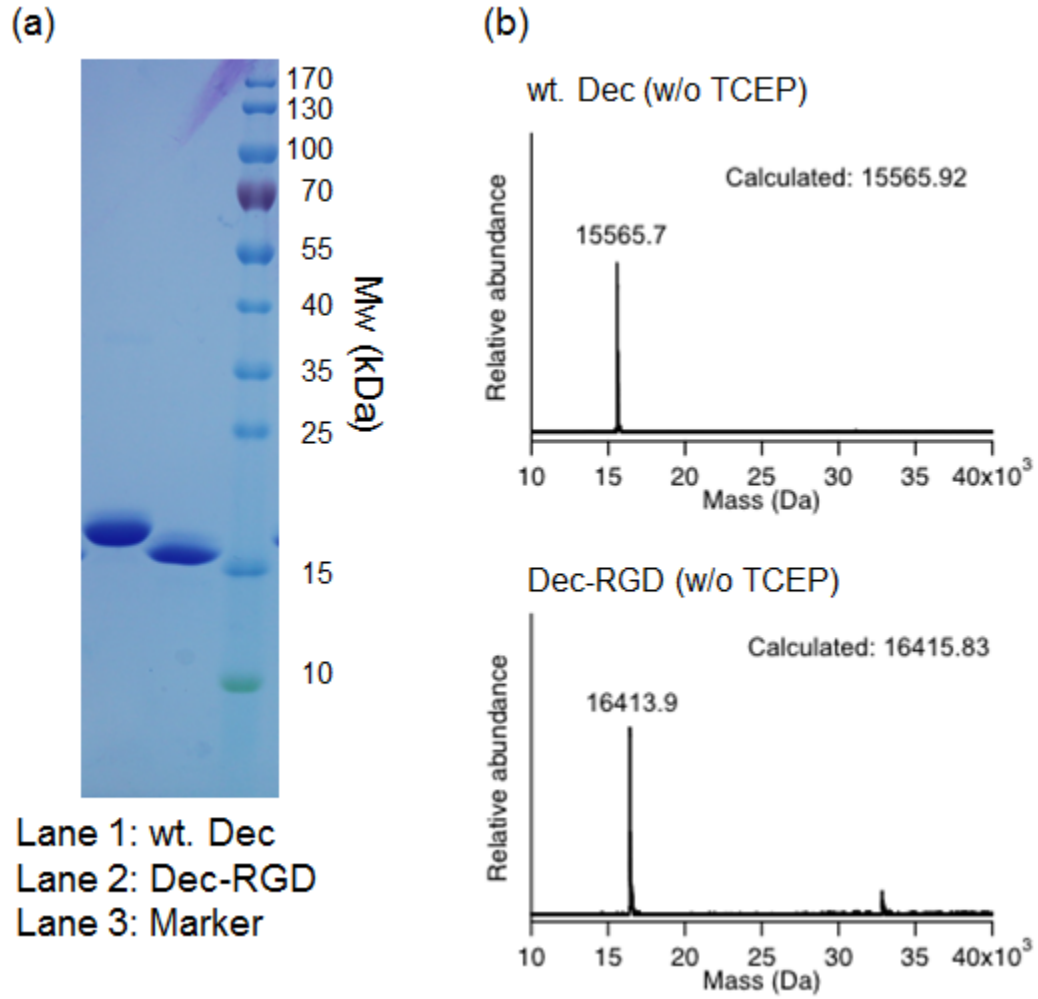

Figure 7.3: Characterization of wt. Dec and Dec-RGD. (a) denaturing SDS-PAGE gel shows bands at expected molecular weights for wt. Dec and Dec-RGD. (b) Subunit mass spectrometry analysis of wt. Dec and Dec-RGD confirm correct mass of both constructs.

Binding of Engineered Dec to P22 VLP and P22-xAEMA

P22 VLP associated with wt. Dec and Dec-RGD were run on SDS-PAGE after removal of unbound Dec proteins. Co-existence of stained bands corresponding to P22 coat protein (46.6 kDa) and Dec-RGD in each sample indicates that the engineered Dec proteins as well as wt. Dec are able to bind with expanded form of P22 VLP (Figure 7.4).

In addition, it is confirmed that the Dec proteins bind with a polymer encapsulated P22 VLP, i.e. P22-xAEMA as well as empty P22 (Appendix E, Figure E3). According to the DLS analysis of P22 VLPs with Dec proteins, all samples showed similar hydrodynamic diameters with highly monodispersed size distribution (Appendix E, Figure E4). The result indicates that the Dec-RGD do not induce significant aggregation of P22 VLP.

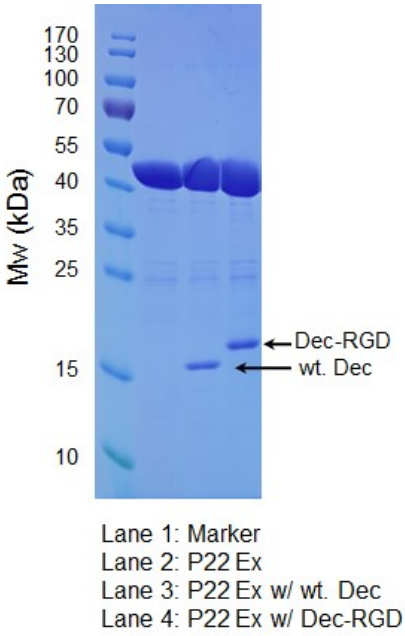

Figure 7.4: SDS-PAGE of Dec-RGD and wt. Dec.

Cell Viability Assay

Cytotoxicity of P22-xAEMA-Gd and those associated with Dec proteins were assessed in concentration of 30 μM and 100 μM Gd using a cell counting kit-8 (WST-8 assay). Viability of C32 cells incubated with P22-xAEMA-Gd or those with various Dec proteins did not decrease with either Gd, whereas viability of the cells with free Gd decreased significantly. This result demonstrates that P22 VLP and Dec proteins does not

have significant toxicity (Appendix E, Figure E5). In addition, Gd encapsulated in P22 VLP is tightly chelated as a form of Gd-DTPA, therefore P22-xAEMA-Gd does not exhibit significant toxicity similar to FDA approved Magnevist does not.

Cell Targeting Capability of P22 VLP
with Engineered Dec and C-terminal of P22

Cell targeting abilities of P22 VLP with the engineered Dec proteins and c-terminal of P22 were first evaluated with FACS. C32 melanoma cell were used to investigate Dec-RGD and P22 (S39C) C-terminal RGD, because C32 cell overexpress integrin $\alpha_v\beta_3$, a receptor for RGD-2C peptide. C32 cells incubated with Dec-RGD possessing P22 exhibit a geometric (geo.) mean fluorescence intensity of 597 (Figure 7.5). This value is more than two times higher that geo. mean of cells incubated with P22 (256) and cells incubated with wt. Dec possessing P22 (261) and more than three times higher than autofluorescence of the cells (geo. mean of 185). C32 cells incubated with P22 (S39C) C-terminal RGD exhibit a geometric (geo.) mean fluorescence intensity of 238.5 (Appendix E, Figure E6). This value is more than three times higher that geo. mean of cells incubated with P22 (66.9) and more than six times higher than autofluorescence of the cells (geo. mean of 39.7).

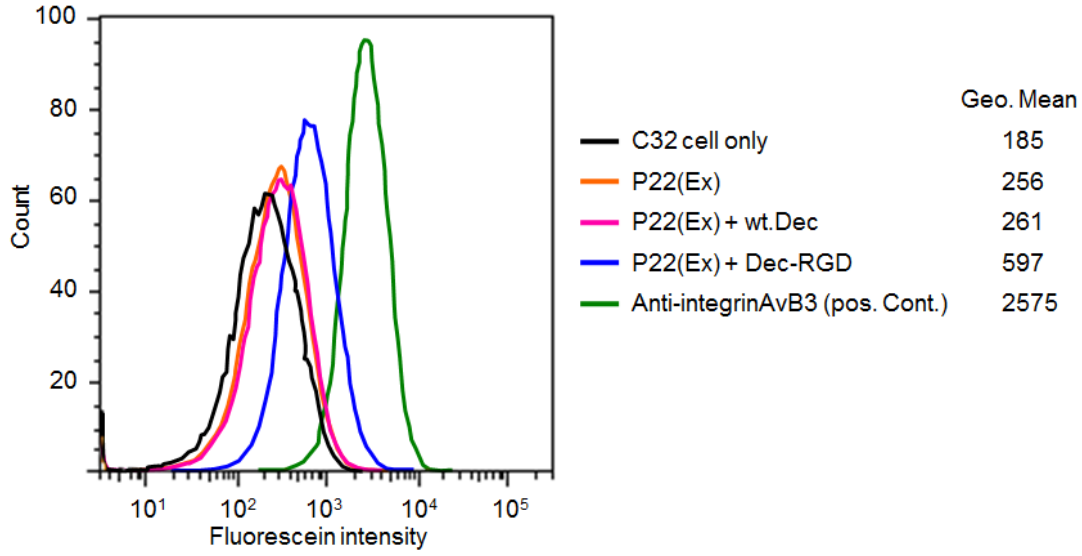

Figure 7.5: FACS analysis of Dec-RGD versus wt. Dec.

In Vitro MRI

In order to evaluate benefit of association of cell-targeting Dec protein on the P22 based MRI contrast agent we have developed, C32 cells were incubated with P22-xAEMA-Gd or Dec possessing P22-xAEMA-Gd and then subjected to MRI. C32 cells incubated with P22-xAEMA-Gd or that associating with wt. Dec exhibited higher contrast than cells incubated with Magnevist likely due to much higher r_1 relaxivity of P22-xAEMA-Gd than Magnevist (Figure 7.6). More importantly, cells incubated P22-xAEMA-Gd associating with Dec-RGD exhibited the highest signal-to-noise ratio among the conditions (Figure 7.6). This result clearly demonstrates that decoration of P22-xAEMA-Gd with cell targeting Dec protein could further improve cellular imaging capability of the contrast agent due to cell specific delivery of the agent.

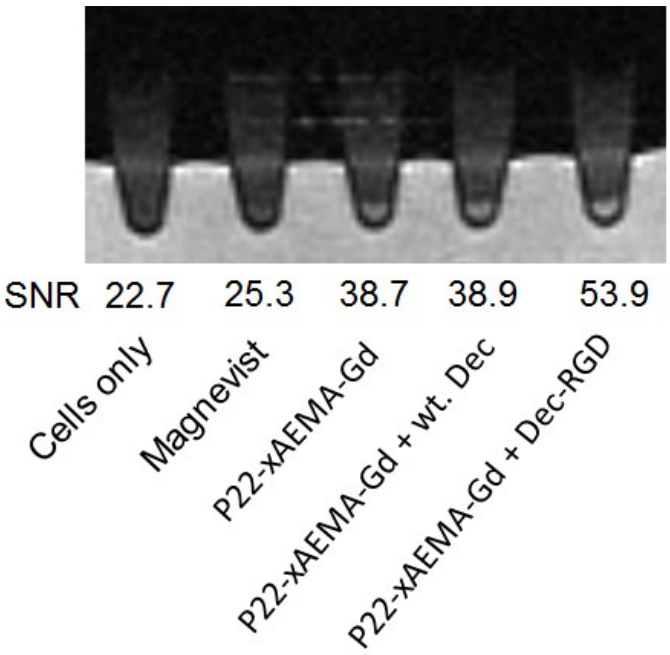

Figure 7.6: A T1-weighted image of P22 with Dec-RGD. Targeted construct shows highest signal to noise (SNR) ratio, indicating enhanced contrast over non-targeted counterparts.

Conclusion

In summary, we have shown the successful incorporation of RGD peptides on the surface of P22 VLPs via two methods, either on the c-terminal of phage decoration protein (Dec) or c-terminal of coat protein of P22. Biophysical characterization of the constructs showed correct assembly of capsids. Furthermore, FACS showed both constructs target C32 melanoma cells compared to their non-RGD counterparts, showing compartivie binding to positive control integrin αvβ3, which is upregulated in activated macrophages and angiogenic endothelial cells. The ability to deliver targeted agents to the vessel wall could have applications in imaging atherosclerotic plaque regions, and

ultimately lower contrast agent dosage administration reducing the risk of toxicity associated with gadolinium (i.e. NSF).

Experimental

Materials

All chemical reagents used in this study were analytical grade and purchased from either Sigma-Aldrich or Fisher Scientific and used as received unless otherwise noted. All water was deionized using a NANOpure water purification system (Thermo Scientific).

Purification of P22 Capsid

A cysteine residue was genetically introduced to serine 39 position of P22 coat protein, which is expected to be located on the surface of the interior cavity of the P22 capsid [76; 77]. In this study, the cysteine residue was utilized as a reaction site to conjugate a fluorescence molecule or an initiator molecule for polymer formation inside of the cavity as described later [225; 256]. The point mutation was made by an established QuickChange method (Agilent Technologies, Santa Clara, CA) using pET-11a based plasmids encoding genes for scaffolding and coat protein [225; 256]. P22 S39C VLP was produced by a heterologous expression system in *E. coli* and purified by a previously described procedure [187; 225; 256].

P22 procapsid was heat treated at 65˚C for 20 min to transform the protein into its expanded (EX) form as previously described [82; 83]. The heat-treated sample was purified by pelleting via centrifugation at 45,000 rpm for 50 minutes in an ultra centrifuge

(Sorvall, WX Ultracentrifuge), followed by resuspension into a (conc, salt) phosphate buffer, pH 7.0.

Mutagenesis and Purification of Dec Proteins and P22 (S39C) C-terminal RGD

The Dec gene was cloned into the pETDuet-1 vector (Novagen) as follows. The Dec gene was amplified by polymerase chain reaction (PCR). The PCR product was then cloned into the *Bam*HI and *Sac*I restriction sites of the pETDuet-1 vector. The resulting plasmid encoding wild-type Dec (wt. Dec) expresses N-terminally histidine-tagged Dec protein. Subsequently, a Dec mutant was engineered from the plasmid encoding wt. Dec protein- RGD-2C peptide (CRGDCG) was incorporated into C-terminus of the wt. Dec (Dec-RGD). To incorporate the RGD-2C peptide sequence onto the C-terminus of the Dec, a corresponding gene was amplified by PCR using a pair of primers. Four amino acids residues (GSGG) were inserted between C-terminus of Dec and RGD-2C peptide as a linker. The PCR product was cloned into the *Bam*HI and *Sac*I restriction sites of the pETDuet-1 vector. The P22 (S39C) C-terminal RGD was prepared similarly. The same RGD-2C peptide sequence was incorporated onto the C-terminal on coat protein of P22 (S39C) using PCR. The PCR product was cloned at *NdeI* and *XhoI* restriction sites of the pETDuet-1 vector.

Each plasmid was transformed into *E. coli* strain BL21 (DE3), and cells were grown in LB medium at 37 °C with 100 mg/L ampicillin. Expression of Dec and P22 was induced by IPTG (0.3 mM) when the culture reached optical density at 600 nm, around 0.6, and cells were cultured for an additional 12 h. After the incubation, cells were

collected by centrifugation. P22 (S39C) C-terminal RGD was purified as previously described for P22 (S39C).[225] Interestingly, we found that wt. Dec and Dec-RGD proteins exist not only in the cell pellet but also in their supernatants suggesting these proteins were excluded out from the cells. Therefore, we purified the proteins from supernatants as follows. The supernatant was filtered with a 0.4 μm pore membrane to remove particulates and dust, then purified by passing over a column filled with Ni-NTA superflow resin (Qiagen) that was connected to a fast protein liquid chromatography (Bio-Rad, Hercules, CA). The bounded proteins were eluted by a gradient of 0 to 500 mM imidazole with 500 mM NaCl, 20 mM sodium phosphate, pH 7.4. A typical chromatography profile is shown in Appendix E, Figure E1. About 20 mg of Dec protein or its mutants were obtained from 300 mL of cell culture supernatant.

Conjugation of Fluorescence
Molecule to P22 S39C

P22 VLP was labeled with fluorescein-5-maleimide (Anaspec, Fremont, CA) via cysteine 39 for in vitro fluorescence-activated cell sorting (FACS). P22 VLP was treated with 1 mM DTT for 4h to reduce all the reactive cysteine residues, followed by purification by pelleting via centrifugation and resuspension into 100mM NaCl, 50mM sodium phasphate, pH 7.0. The P22 protein (2 mg/mL) was mixed with 0.5 molar equivalent per subunit of fluorescein at room temperature for 5 h. The protein was purified away from unreacted dye by pelleting and resuspending in either NaCl 100 mM, sodium phosphate 50 mM, pH7.0 or Dulbecco's phosphate buffer saline (DPBS).

P22-xAEMA Polymer Formation

Cross-linked AEMA polymer (xAEMA) was synthesized inside the P22 VLP cavity by a procedure described in a previous report [225]. Briefly, first 2-bromoisobutyryl aminoethyl maleimide (Nint), which serves as a radical initiator for ATRP, was synthesized in dichloromethane by a modification of the procedures previously reported [203]and the molecule was introduced inside of P22 at the cysteine 39 position. Second, cross-linked AEMA polymer (xAEMA) was synthesized inside the P22 VLP cavity. P22-Nint (100mM sodium phosphate, 50 mM sodium chloride, pH 7.6) was added to 2-aminoethyl methacrylate (AEMA) / bis-acrylamide solution (100mM sodium phosphate, 50 mM sodium chloride pH 8.0) in a crimp-top vial. The vial was vacuum pumped and back filled with Ar four times to deaerate the mixture. A metal catalyst solution which was composed of CuBr, $CuBr_2$ and 2,2'-bipyridine at a molar ratio of 1:1:4 and was added to the monomer-protein vial, which was maintained at 23 ºC for the remaining duration of the experiment. After 3 h the reaction was quenched by exposure to air and the protein-polymer composite was purified away from unreacted monomer and the copper catalyst by pelleting and resupending the protein 2 times into 100 mM sodium carbonate, 50 mM NaCl buffer, pH 9.0. Yield of P22 after the polymerization reaction was 52% from a starting amount P22 EX.

Conjugation of Gd-DTPA to P22-xAEMA

P22-xAEMA was labeled with Gd-DTPA according to established procedures and applied for contrast agent of in vitro MRI of cells [36; 225]. Briefly, 55.74mg of p-SCN-Bn-DTPA (Macrocyclics, Dallas, TX) was dissolved in 2.74mL H2O and 762uL sodium

bicarbonate buffer (900mM, pH 9.0) as a concentration of 26 mM. 3.36 mL of p-SCN-Bn-DTPA was mixed with 95.3 μL of $GdCl_3$ solution (900 mM in water) and stirred at room temperature for 3 h. The solution was subsequently diluted to 20 mM of p-SCN-Bn-DTPA with DMSO and then added to the P22-xAEMA (40 mg in 100 mM sodium bicarbonate, 50 mM NaCl, pH 9.0). The mixture was allowed to react at 4 °C overnight followed by purification away from unreacted p-SCN-Bn-DTPA-Gd by pelleting down and resuspending the protein in DPBS.

Dec Binding to P22 VLP

P22 VLP, fluorescently labeled P22 or P22-xAEMA was mixed with wt. Dec or Dec-RGD to decorate the exterior surface of P22 with Dec protein. Typically 4 mg of P22 VLP (0.2 nmol as cage) was mixed with 160 excess of Dec (as trimer) / P22 cage (i.e. 2 times excess Dec / Dec binding site of P22 VLP) in 50 mM sodium phosphate, 100 mM NaCl buffer, pH 7.0 and incubated at room temperature for 2 h with gentle rotation. The P22 VLP decorated with Dec was purified away from unbound Dec by pelleting down P22 VLP via centrifugation at 45,000 rpm for 50 minutes in an ultra centrifuge and resuspending in DPBS, followed by spinning down with a table top centrifuge at 13,300 rpm to remove any aggregate.

Cell Culture Condition

Human amelanotic melanoma cell line, C32 (ATCC CRL-1585) was purchased from the American Type Culture Collection. The C32 cells were cultured in Eagle's Minimum Essential Medium (EMEM, ATTC 30-2003) supplemented with 10 % fetal

bovine serum (Atlanta Biologicals, Norcross, GA), 100 units/ml of penicillin and 100 μg/ml of streptomycin at 37°C in 5% CO_2 atmosphere.

General Analysis of Samples

The P22 VLP, Dec and all modified constructs were analyzed with UV-Vis spectroscopy (UV-Vis; Model 8453, Agilent, Santa Clara, CA), dynamic light scattering (DLS; 90Plus particle size analyzer, Brookhaven Instrument, Holtsville, NY), and transmission electron microscopy (TEM: LEO 912AB). For TEM observation, samples were transformed to formvar coated copper grids and were imaged with a 1 % uranyl acetate stain. The samples were also analyzed using SDS-PAGE on 20% gradient Tris-glycine gels.

Fluorescence Activated Cell Sorting (FACS) Analysis

The cell targeting capability of P22 VLPs decorated with Dec derivatives and P22 (S39C) C-terminal RGD were assessed with FACS. C32 cells, which overexpress integrins a_vb_3 were used to evaluate P22 (S39C) decorated with Dec-RGD and P22 (S39C) C-terminal RGD. In order to perform the analysis, cells were washed with PBS (without Ca^{2+} and Mg^{2+}) followed by detaching cells from the dishes using Accutase (Sigma) before further experiments. The cells were harvested by centrifuge at 1000 rpm for 5 min and then suspended in DPBS (with Ca^{2+} and Mg^{2+}) at a concentration of 5 x 10^6 cells /mL. Subsequently the cells were incubated with fluorescein-conjugated P22 VLP or those decorated with Dec proteins on ice for 30 min under normalized fluorescein concentration (2 μM). After the incubation, the cells were washed 2 times with DPBS

(with Ca^{2+} and Mg^{2+}) and then resuspended in DPBS (with Ca^{2+} and Mg^{2+}). For the assessment of integrins $\alpha_v\beta_3$ targeting, fluorescein-conjugated anti-integrin $\alpha_v\beta_3$ mAb (Millipore, MAB1976F) was used as a positive control. Flow cytometry was performed on a FACSCanto, (BD Biosciences) and analyzed using FlowJo (Tree Star, Inc.).

In Vitro MRI of C32 Cells
Labeled with P22-xAEMA-Gd

MR imaging capability of P22-xAEMA-Gd decorated with Dec proteins was investigated. For this assessment, C32 cells were seeded into 6 cm cell culture dish at the concentration of 9 x 10^6 cells/dish. After 48 h of incubation, cell culture medium was exchanged to 3 mL of fresh medium and various P22-xAEMA-Gd samples (with or without Dec proteins) were added to each dish under normalized Gd concentration of 100 μM. The cells were further incubated at 37°C in 5% CO_2 atmosphere for 24 h. After incubation, the solution was aspirated and the cells gently washed with DPBS followed by harvesting cells using Accutase. The cells were suspended in DPBS and number of viable cells was determined by trypan blue exclusion assay and counting using a hemocytometer. Subsequently, 1 x 10^6 cells incubated with each sample were transferred in a PCR tubes and pelleted down by centrifuge at 1000 rpm for 5 min.

Cell Viability Assessment

Cytotoxicity of P22-xAEMA-Gd and those decorated with Dec proteins were evaluated by cell viability assay using a cell counting kit-8 (Dojindo, Rockville, MD). For this assessment, 6 x 10^3 cells /well of C32 cell were seeded in 96-well plate and cultured as described in the previous section. After 48 h, the cell culture medium was

removed from each well and then 100 μL of fresh cell culture medium supplemented with various P22-xAEMA-Gd samples under normalized Gd concentration (30 or 100 μM). After 24 h of incubation, the culture medium was exchanged to 100 μL of fresh medium and 10 μL of cell counting kit-8 solution was added to each well. After 3 h of incubation at 37°C in 5% CO_2 atmosphere, absorbance at 450 nm of the solution in each well was measured with a microplate reader.

CHAPTER 8

CONCLUSION

The bacteriophage P22 is a remarkable protein container. The assembly process is well defined, leading to precise T=7 capsids that are easily modified genetically or chemically. The capsids are malleable and three additional morphologies are accessible for nanomaterial design. The research described in this thesis has been inspired by the unique properties of nanoparticles which make them desirable for biomedical applications, specifically in the design of T_1-enhanced MRI contrast agents from virus-like particles. In this and other work, protein cages have been used to make a variety of protein-based composite materials. Often these synthetic materials are made with a biomimetic approach using mild reaction conditions in an aqueous environment. As this field has expanded the potential applications of these materials has become more diverse to include materials aimed toward energy, electronics, and medical applications. While much of the field is application driven, these studies also serve to improve our understanding of the native protein behavior and processes.

In Chapter 3, we have shown that VLPs derived from the bacteriophage Qβ can serve as a platform for controlled radical polymerization to produce polymer-coated protein nanoparticles. The size and surface properties of Qβ can be significantly altered through ATRP, while still retaining the low polydispersities associated with VLPs. Furthermore, the polymer-coated particles are accessible to bioconjugation at both the chain termini and suitably derivatized polymer sidechains. The platform allows for both

conjugation of small-molecule imaging agents and chemotherapeutics. The the exterior surface of Qβ has been modified via two different bioconjugation techniques, Cu (I) catalyzed “click” chemistry (AACC) and atom transfer radical polymerization (ATRP). The ATRP polymer was subsequently functionalized with a small molecule contrast agent, Gd-DOTA. This construct had high loading capacity, and consequently had high ionic and particle relaxivities.

In Chapter 4, AACC approach of step-wise polymerization was extended to a larger virus-like particle, P22, up to generation 4.5. Instead of modifying the exterior surface, as was done with Qβ, the polymer was constrained to the interior surface of the capsid, such that the exterior surface was available for attachment of targeting ligands. We have synthesized a branched oligomer conjugated to multiple DTPA-Gd complexes inside of P22 ‘wiffleball’ viral capsids. This resulted in one of the highest reported particle relaxivities for viral-capsid based systems and a significant improvement in ionic relaxivity over free DTPA-Gd. The rotational correlation time has been optimized for this system, while conjugation of different chelator-Gd complexes has been suggested for improvement of the mean residence lifetime. By using a larger particle, the loading capacity was increased leading to higher ionic and particle relaxivities than with Qβ.

The use of ATRP made possible the internally confined grafted-from polymer described in Chapter 5. This primary amine rich polymer begins to take advantage of the previously largely untapped interior volume of the P22, where internal occupancy otherwise relied on genetic modification of the scaffold protein. The use of AEMA to form the polymer results in a scaffold, which can be subsequently labeled with molecules

of interest such as fluorophores or MRI contrast agents in such a manner that the same approach could be applied to other protein-based systems. The labeled P22-polymer composite in chapter 5 had an order-of-magnitude improvement in relaxivity on a particle basis over other VLP based contrast agents and was competitive with other macromolecular MRI contrast agent vehicles, but was more monodisperse. Due to the promising medical applications of this material work to make further improvements in the MRI contrast agent carrier through targeting the construct to specific tissues is ongoing.

In Chapter 6, manganese porphyrins were conjugated to P22-ATRP in high payload. Manganese was explored as a T_1-enhanced contrast agent as an alternative to gadolinium based contrast agents, due to associated toxicity with gadolinium. We covalently encapsulated a large number of MnPP inside P22 VLP-polymer hybrids and demonstrated potential for this construct as a tunable MRI contrast agent. Although we did not see an improvement in $r_{1,ionic}$ relaxivity, the high per-particle relaxivity of the P22-xAEMA-MnPP, resulting from high loading density, could be beneficial when these particles are imparted with targeting cell capabilities.

Chapter 7 detailed the display of targeting peptides on P22 capsids and the successful application of the C-terminal location of Dec and P22 for targeting of avB3 integrins. Predicting the responses generated based upon the protein cage structure and structural modifications continues to be an intriguing challenge, and studies here have revealed that the local environment at the site of administration plays a role in the response. This information can continue to be exploited in combination with genetic

engineering to display antigens on the P22 capsids in a way that closely mirrors the presentation of antigenic epitopes on pathogens.

In conclusion, bacteriophage P22 virus-like particles, among others, have been used as a platform for developing MRI contrast agents. High loading, targeting ability, and slow molecular tumbling all lead to an enhanced imaging agent. These next generation contrast agents can ultimately lower dosage and reduce risk of toxicity associated with Gd-based contrast agents.

APPENDICES

APPENDIX A

SUPPORTING INFORMATION FOR CHAPTER 3

Supporting Information

Reagents.

Methanesulfonyl chloride (99.5%), sodium azide (99%), triphenylphosphine (99%), propargyl bromide (80 wt% in toluene), 2-bromo-2-methylpropionyl bromide (98%), and tetraethylene glycol (99.5%) were purchased from Acros Organics. Triethylamine (99+%) was purchased from Alfa-Aesar. Sodium hydride (95%) was purchased from Sigma-Aldrich. Di-*tert*-butyl dicarbonate was purchased from Oakwood Products, and trifluoroacetic acid was purchased from Halocarbon. Octa(ethylene glycol) methacrylate (6, Mn = 526) was purchased from Sigma-Aldrich. Tetrahydrofuran (THF) was dried over sodium benzophenone ketyl.

Dichloromethane (CH2Cl2) was dried over molecular sieves.

Instrumentation.

^{1}H and ^{13}C NMR spectra were recorded on either a Bruker AV-400 or a Varian AM200 spectrometer in CDCl3. Routine mass spectra were obtained using an Agilent 1100 (G1946D) ESI MSD with mobile phase composed of 9:1 CD3CN:H2O containing 0.1% CF3CO2H. Attenuated total reflectance (ATR) –FTIR spectra were obtained using a Nicolet 6700 spectrometer using a ZnSe crystal. Size exclusion chromatography was performed on an AKTA explorer (GE Life Sciences) equipped with a superose 6 column (0.4 mL/min, 0.1 M KPO4 elution buffer). Dynamic light scattering (DLS) measurements were taken on a Dynapro plate reader (Wyatt Technology) fitted with a glass-bottomed optical 384-well plate (Greiner). Values represent the average of 10 independent

measurements where 10 individual acquisitions were taken per measurement. Fluorescence measurements of Doxorubicin-loaded particles were collected in triplicate in black 96-well plates using a Thermo VarioSkan plate reader (excitation: 480 nm, emission: 598 nm).

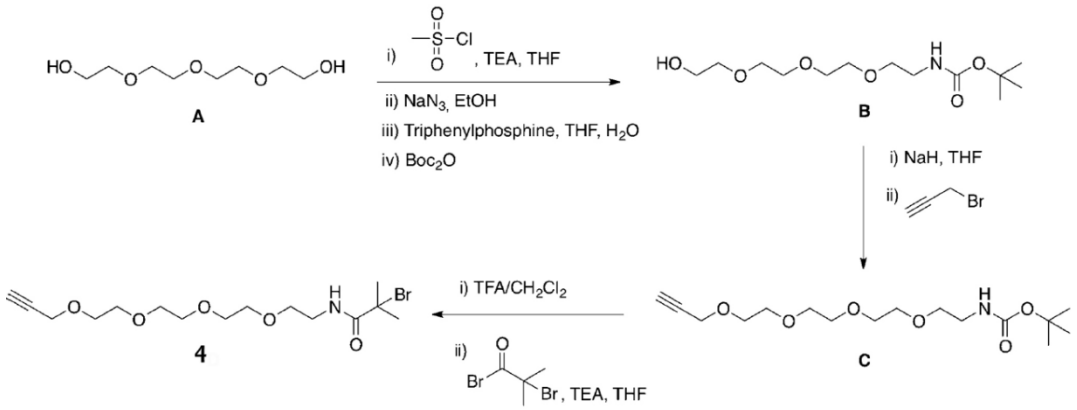

Figure A1: Synthesis of alkyne-functionalized ATRP initiator 4.

Syntheses.

Synthesis of α-hydroxyl, ω-amino(Boc) Tetraethylene Glycol (B) – Tetraethylene glycol (A) (50.0 g, 257.4 mmol) was dissolved in anhydrous THF (250 mL) under a nitrogen atmosphere and cooled to 0oC using an ice-water bath. Methanesulfonyl chloride (5.00 mL, 64.4 mmol) was added by syringe in one portion, and triethylamine (9.0 mL, 64.4 mmol) was subsequently added by syringe over approx. 20 minutes. After triethylamine addition was complete, the ice bath was removed and the reaction was allowed to stir at room temperature overnight under a nitrogen atmosphere.

The reaction mixture was concentrated and dissolved in ethanol (250 mL). Sodium azide (20.9 g, 322.0 mmol) was added as a solid, and the reaction was heated to

reflux for 6 hr. After cooling to room temperature, the contents were concentrated and dissolved in deionized water. The product was extracted with CH2Cl2 (6x), and the combined organic fractions were dried over magnesium sulfate, filtered, and concentrated to a light yellow oil.

The oil was subsequently dissolved in THF (200 mL), and triphenylphosphine (18.6 g, 70.8 mmol) was added as a solid. Once a homogeneous solution had been obtained, deionized water (20 mL) was added, and the contents were stirred at room temperature, open to air, for 2 hours. Di-*tert*-butyl dicarbonate (17.6 g, 80.5 mmol) was added as a solid in one portion, and the reaction mixture was stirred overnight at room temperature, open to air. The mixture was concentrated, dissolved in diethyl ether (100 mL) and placed in the freezer (-20°C) overnight. Crystalline triphenylphosphine oxide was removed by filtration, the filtrate was concentrated, and the product was purified by column chromatography (silica) eluting with 98/2 → 95/5 CH2Cl2/MeOH to yield 4.3 g (23% overall yield) of a light yellow, viscous liquid. ^{1}H NMR (CDCl3) δ 5.64 (br s, 1H), 3.57 - 3.75 (br, complex m, 12H), 3.52 (t, 2H), 3.29 (m, 2H), 1.42 (s, 9H) ppm; 13C NMR (CDCl3) δ 156.4, 79.2, 72.8, 70.8, 70.6, 70.4, 70.2, 61.8, 40.5, 28.6 ppm. ATR-FTIR 3358, 2870, 1693, 1518, 1454, 1391, 1365, 1276, 1249, 1170, 1099, 937, 864, 781 cm^{-1}.

Synthesis of α-propargyl, ω-amino(Boc) Tetraethylene Glycol (C) – α-hydroxyl, ω-amino(Boc) tetraethylene glycol (B) (4.1 g, 14.0 mmol) was dissolved in anhydrous THF (100 mL) under a nitrogen atmosphere. Sodium hydride (0.38 g, 16.0 mmol) was added in one portion as a solid, and the reaction was stirred for 20 min at room

temperature at which time a nearly homogenous solution was obtained. The reaction was cooled to 0 °C using an ice-water bath, and propargyl bromide (1.5 mL, 21.0 mmol) was added by syringe over approx. 10 min. After 1 hr, the ice bath was removed, and the contents were allowed to stir overnight at room temperature under nitrogen. The reaction mixture was concentrated, suspended in CH2Cl2, and washed once with brine and then once with deionized water. The organic fraction was dried over magnesium sulfate, filtered, and concentrated. The product was purified by column chromatography (silica) eluting with 50/50 → 60/40 ethyl acetate/hexane to yield 3.3 g (71% yield) of a light yellow, viscous liquid. 1H NMR (CDCl3) δ 5.05 (br s, 1H), 4.18 (d, 2H) 3.57 - 3.75 (br, complex m, 12H), 3.52 (t, 2H), 3.29 (m, 2H), 2.41 (t, 1H), 1.42 (s, 9H) ppm; 13C NMR (CDCl3) δ 156.2, 79.8, 79.3, 74.7, 72.8, 70.8, 70.7, 70.7, 70.6, 70.4, 69.2, 58.5, 40.5, 28.6 ppm. ATR-FTIR 3249, 2869, 1707, 1511, 1455, 1391, 1365, 1248, 1170, 1095, 1035, 863, 781 cm^{-1}.

Synthesis of α-propargyl, ω-isobutyryl Bromide Tetraethylene Glycol (4) – α-propargyl, ω-amino(Boc) tetraethylene glycol (C) (1.5 g, 4.5 mmol) was dissolved in CH2Cl2 (10 mL), and trifluoroacetic acid (TFA, 10 mL) was added. The mixture was stirred at room temperature, open to air, for 1.5 hrs. The reaction contents were concentrated and dissolved in deionized water. The pH was adjusted to 14 by addition of 2.0 M NaOH (aq), and the product was extracted 4X with CH2Cl2. The combined organic fractions were dried over magnesium sulfate, filtered, and concentrated to yield 1.0 g (96% yield) of a light yellow oil.

The deprotected α-propargyl, ω-amino tetraethylene glycol (1.0 g, 4.3 mmol) was immediately dissolved in anhydrous THF (25 mL) and cooled to 0 oC using an ice-water bath. Triethylamine (0.72 mL, 5.2 mmol) was added by syringe, followed by 2-bromo-2-methylpropionyl bromide (0.64 mL, 5.2 mL). After approx. 30 min, the ice bath was removed and the reaction was allowed to stir at room temperature overnight under a nitrogen atmosphere. The mixture was concentrated, dissolved in CH2Cl2, washed once with 1M HCl (aq) and then once with brine. The organic fraction was dried over magnesium sulfate, filtered, and concentrated. The product was purified by column chromatography (silica) eluting with a 50/50 → 60/40 ethyl acetate/hexane to yield 1.3 g (80% yield) of 4 as a light yellow, viscous liquid. 1H NMR (CDCl3) δ 7.12 (br s, 1H), 4.18 (d, 2H) 3.60 - 3.75 (br, complex m, 12H), 3.57 (t, 2H), 3.45 (m, 2H), 2.42 (t, 1H), 1.93 (s, 6H) ppm; 13C NMR (CDCl3) δ 172.1, 79.7, 74.7, 72.8, 70.7, 70.7, 70.6, 70.5, 70.5, 69.5, 69.2, 62.7, 58.5, 40.2, 32.6 ppm. ATR-FTIR 3246, 2867, 1661, 1520, 1460, 1349, 1288, 1190, 1096, 1033, 920, 866, 842, cm^{-1}.

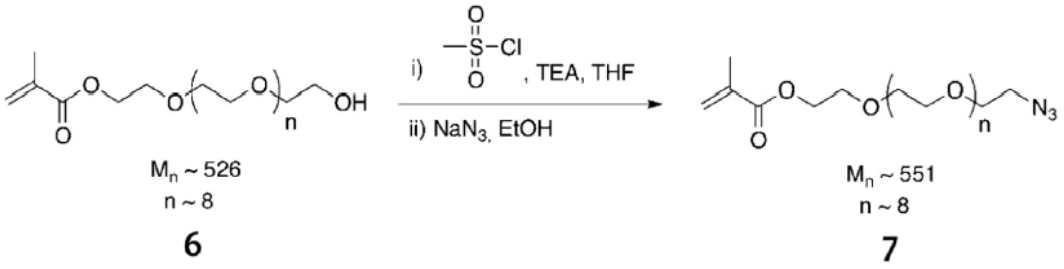

Figure A2: Synthesis of azidofunctionalized octa(ethylene glycol) methacrylate (OEGMA-N3).

The oligomeric ethylene(glycol) methacrylate 6 was purchased and purified by column chromatography (silica) eluting with 70/20/10 CH2Cl2/acetone/MeOH before

use. The resulting material was found to be largely the octaethylene glycol structure shown. This compound (4.8 g, 11.0 mmol) was dissolved in anhydrous THF (75 mL) under a nitrogen atmosphere and cooled to 0 °C using an ice-water bath. Methanesulfonyl chloride (1.1 mL, 13.7 mmol) was added by syringe in one portion, followed by triethylamine (2.0 mL, 14.0 mmol). After approx. 30 min, the ice bath was removed, and the reaction was allowed to stir at room temperature overnight under a nitrogen atmosphere.

The contents were concentrated and dissolved in ethanol (100 mL). Sodium azide (3.6 g, 55.0 mmol) was added, and the suspension was heated to reflux for 6 hrs. After cooling, the mixture was concentrated and dissolved in deionized water. The product was extracted 6X with CH2Cl2, and the combined organic fractions were dried over magnesium sulfate, filtered, and concentrated to a light, yellow oil. The product was purified by column chromatography (silica) eluting with a 70/28/2 CH2Cl2/acetone/MeOH to yield 7 (1.2 g, 25% yield) as a light yellow, viscous liquid. ^{1}H NMR (CDCl3) δ 6.09 (m, 1H), 5.54 (m, 1H), 4.26 (t, 2H), 3.50 - 3.75 (br, complex m, 104H), 3.35 (t, 2H), 1.91 (m, 3H) ppm. 13C NMR (CDCl3) δ 125.9, 70.8, 70.8, 70.7, 70.6, 70.1, 69.2, 64.0, 50.8, 18.4 ppm. ATR-FTIR 2866, 2099, 1717, 1453, 1349, 1296, 1097, 1038, 944, 850, 732 cm^{-1}.

Synthetic Manipulations
of Virus-Like Particles

Synthesis of Qβ Macroinitiator (5) *N*-hydroxysuccinimide ester 2 (37 mg, 120 μmol) was dissolved in 2 mL of DMSO and slowly added to 6.5 mL of 0.1M KPO4 pre-

chilled in an ice bath. WT-Qβ (1, 21 mg, 8 nmol particle, 1.5 μmol subunits, 6.0 μmol reactive amine groups) in 2 mL 0.1M KPO_4 was added to this solution to initiate reaction. The reaction proceeded for 6 hours on a rotisserie shaker at room temperature. The resulting Qβ-N3 particles (3) were purified by sucrose density gradient centrifugation (10-40% gradient, SW28 rotor, 28K, 4 hours). The band corresponding to intact particles was pulled from the gradient (~5 mL per tube) and the product pelleted for a minimum of 2 hours to recover the protein (70K rpm, 70.1 Ti rotor). Protein pellets were resuspended in phosphate buffered saline (pH 7.4, 10 mM KPO_4, 150 mM NaCl). Protein concentrations were then assessed using a Coomassie plus protein quantification kit (Thermo) and BSA standards.

Qβ-N3 particles (3) (10 mg, 4 nmol particle, 0.9 μmol theoretical reactive azides) were diluted to a final concentration of ~2 mg/mL with 0.1M KPO_4 (pH 7.4). A solution of ATRP initiator 4 in deionized (MilliQ purified) H_2O was added to the particle solution (10 mg/mL, 550 μL, 15 μmol). The following solutions were added to the reaction mixture in order: a pre-mixed solution of CuSO4 (10 μL, 50 mM) and THPTA (50 μL, 50 mM), amino guanidine (100 μL, 100 mM), and sodium ascorbate (100 μL, 100 mM). The reaction was allowed to proceed for 2 hours at room temperature, and the product was purified as described for the acylation step. Figure B3 shows the dynamic light scattering analyses of the starting, intermediate, and final products of this sequence.

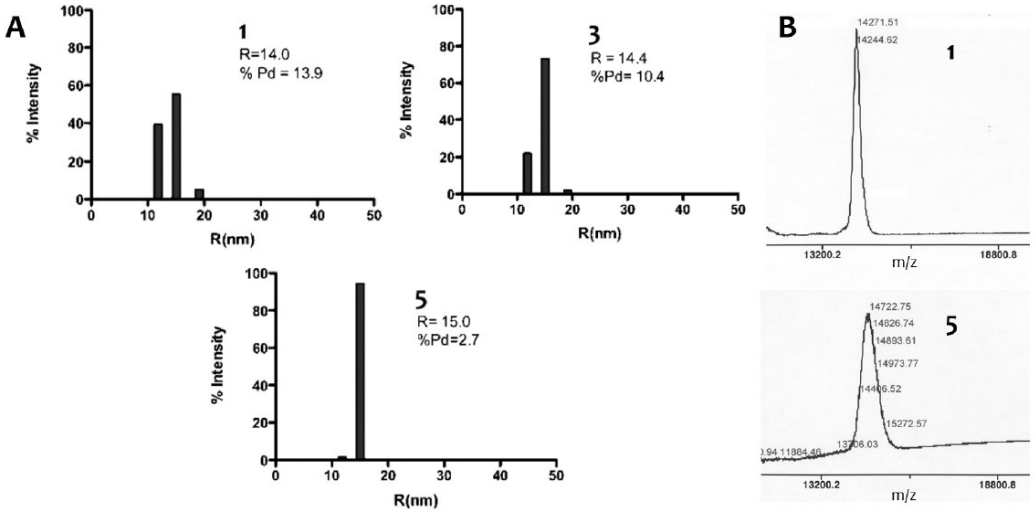

Figure A3: (A) Dynamic light scattering histograms of particles 1, 3, and 5. (B) MALDI-MS of denatured wild-type (1, top) and macroinitiator (5, bottom) particles. In this preparation, the central mass of the peaks correspond to a loading of 150 initiator sites per particle; other preparations ranged from this value to 210 per particle.

Polymerization from Qβ Macroinitiator Particles (5) A typical polymerization reaction was performed as follows. Qβ macroinitiator 3 (4.5 mg, 0.4 μmol initiator sites) was diluted with MilliQ water to a final concentration of 1mg/mL in protein. Monomer 6 or 7 (325 μmol) was then added to the protein solution. Additionally, a stock solution of $CuBr_2$ (6 mg, 27 μmol) and 2,2'-bipyridine (16.7 mg, 107 μmol) was made in H_2O (10 mL). Both solutions were thoroughly degassed, either by N2 bubbling (minimum 45 min) or freeze pump thaw cycles (minimum 3 cycles). Solid CuBr (3.8 mg, 27 μmol) was added to the copper stock solution under nitrogen atmoshphere and sonicated to promote dissolution. The resultant copper stock solution (1 mL) was added to the protein-monomer mixture to initiate polymerization. Polymerizations were allowed to proceed at room temperature under N2 atmosphere for 16 hours. Reactions were subsequently

quenched by exposure to air and addition of 0.5M EDTA (50 μL). Purification was carried out via sucrose density gradient centrifugation (10-40%) and ultrapelleting.

End Labeling of Qβ-OEGMA Particles (8) with AlexaFluor488 Qβ-poly(OEGMA) (8) (1 mg, 88 nmol theoretical polymer chains) was diluted to a working concentration of 2 mg/mL with 0.1M KPO4 (500 μL total volume). Sodium azide (2 mg, 31 μmol) in 50 μL DMSO was added. The reaction proceeded for 24 hours on a rotisserie at room temperature. The resulting Qβ-poly(OEGMA)-N3 particles were purified by ultrapelleting at 70K rpm. The recovered protein (0.75 mg) was resuspended in 500 μL of 0.1M KPO4 buffer, to which was added the following components in order: AlexaFluor488-alkyne (20 μL, 1 mM), a pre-mixed solution of CuSO4 (2.5 μL, 50 mM) and THPTA (12.5 μL, 50 mM), amino guanidine (25 μL, 100 mM), and sodium ascorbate (25 μL, 100 mM). The reaction was allowed to proceed for 1.5 hours at room temperature and the product was purified by sucrose gradient centrifugation (10-40%) and ultrapelleting. Dye loading was calculated by comparing the molar concentration of dye to that of protein as determined by UV absorbance spectroscopy and Bradford assays, respectively.

Gd(DOTA) Conjugation to Qβ-PEG-N3 Particles (9) Qβ-polyOEGMA-N3 particles (9) (2 mg protein, 0.8 nmol VLP, 500 μL PBS) were mixed with Gd-DOTAAlkyne (12) (5 mg, 8 μmol) dissolved in 400 μL H2O. The following solutions were added to the reaction mixture in order: a pre-mixed solution of CuSO4 (5 μL, 50 mM) and THPTA (25 μL, 50 mM), amino guanidine (50 μL, 100 mM), and sodium

ascorbate (50 μL, 100 mM). Reactions proceeded on the bench top for ~24 hours with additional aliquots of sodium ascorbate added at 2 hours and 4 hours to promote reduction of the Cu species to Cu(I). Following the reaction, particles were purified by sucrose density gradient centrifugation (10-40%) followed by ultrapelleting. Gd loading per particle was assessed by comparing protein concentration determined by Coomassie plus assay to ICP values obtained for Gd concentrations.

Doxorubicin Conjugation to Qβ-PEG-N3 Particles Doxorubicin-alkyne (13) (2 mg, 2.6 μmol) was added to 250 μL PBS buffer, leaving a significant portion of the material insoluble. This was removed by centrifugation and the saturated solution was added to a solution of Qβ-poly(OEGMA-N3) particles 9 (3 mg protein, 1.2 nmol VLP) in 600 μL PBS. The following solutions were added to the reaction mixture in order: a pre-mixed solution of CuSO4 (10 μL, 50 mM) and THPTA (50 μL, 50 mM), amino guanidine (100 μL, 100 mM), and sodium ascorbate (100 μL, 100 mM). Reactions proceeded on the bench top for ~18 hours. Following the reaction, particles were purified by sucrose density gradient centrifugation (10-40%) followed by ultrapelleting. Doxorubicin loading per particle was assessed by comparing protein concentration determined by Coomassie plus assay to doxorubicin concentrations assessed by UV spectroscopy.

Cell Viability Studies

HeLa cells were grown in advanced Dulbecco's Modified Eagle Medium (DMEM) supplemented with 5% NCS, and were maintained at 37 °C with 5% CO2 and

95% air. Cells were plated in 96-well plates (7.5 x 103 cells/well) 24 hours prior to treatment with doxorubicin conjugates. Cells were then incubated with the indicated doxorubicin preparation at varying concentrations for 8 hours. Following incubation, the media was removed, wells were washed once with DMEM, and fresh media was added to the plate (100 μL/well). After 24 hours, MTT (5 mg/mL, 50 μL/well) was added to each individual well and incubated at 37 °C for 3 hours. Media was carefully aspirated and DMSO was added (200 uL/well) to dissolve the purple MTTformazan crystals. Absorbance of the dissolved formazan was quantified at 570 nm using a UV-Vis plate reader and cell viability was determined as a fraction of absorbance relative to untreated control wells. Data are presented as average values +/- standard deviation. Figure B4 shows the results from the same treatment with the precursor particles not bearing doxorubicin, showing no toxicity throughout the relevant concentration range.

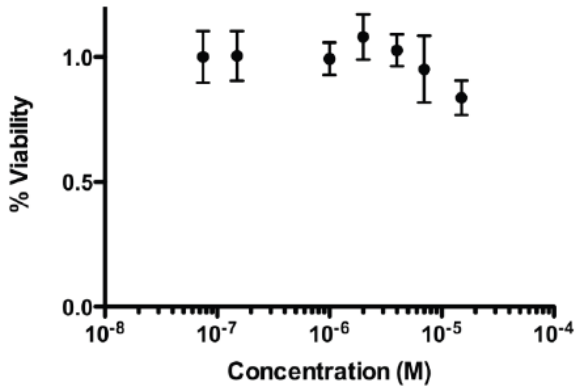

Figure A4: Cytotoxicity of Qβ-PEG-N3 particle (9).

Relaxivity Measurements

T_1 measurements were carried out on Anasazi FT-NMR 60 MHz (1.41 T) and 90 MHz (2.11 T) spectrometers for all samples. Samples 15 (0.24 mM Gd) and 17 (0.14 mM Gd) were diluted twice with phosphate buffer to yield two additional data points in the plot of inverse T_1 vs. Gd concentration. The longitudinal relaxation rate constant (T_1) for each sample was measured using an inversion recovery pulse sequence at 298 K, where the relaxation delay was set to six times the T_1. All measurements were taken in triplicates. The following equation for T_1 relaxation was fit to the experimental data where A, B and T1 were used as fitting parameters.

$$f(t) = A*(1-\exp(-t/T_1))+B$$

The plot of inverse T_1 versus Gd (mM) was used to determine relaxivity values (r_1), where relaxivity per Gd is equal to the slope of the line and relaxivity per VLP was calculated by multiplying the slope by Gd/VLP. An example of a typical plot and determination of relaxivity values is shown in Figure B5.

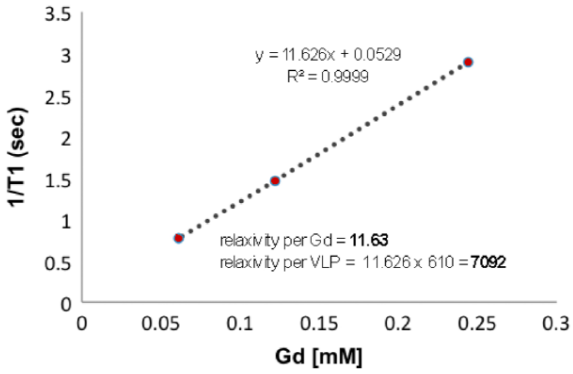

Figure A5: T_1 measurements collected on 60 MHz NMR for sample 15 (610 Gd/VLP). Shown is a plot of $1/T_1$ for 100%, 50%, and 25% of original concentration of gadolinium (mM) in sample 15.

APPENDIX B

SUPPORTING INFORMATION FOR CHAPTER 4

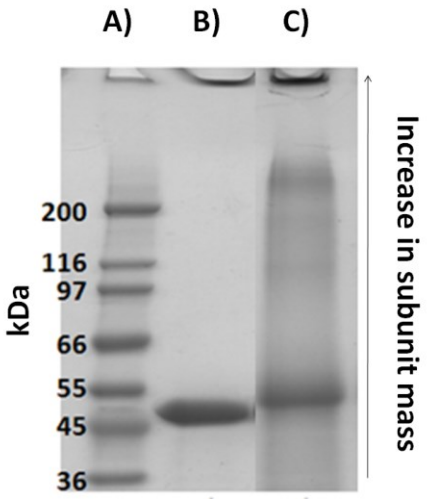

Figure B1: SDS-PAGE gel shows evidence of mass increase after modification. A) SigmaMarker Wide Ladder (MW 6,500-200,000 Da). B) P22 WB migrates at ~46.6kDa. C) P22-AACC-Gd migrates at ~49kDa). Higher molecular weight species are suggestive of inter-subunit cross-linking within the P22 capsid.

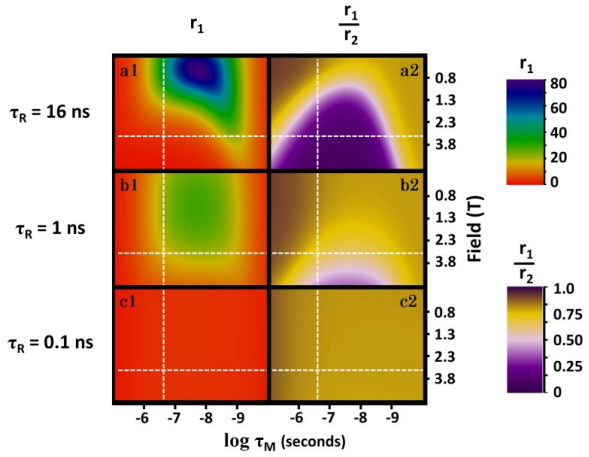

Figure B2: Contour plots of relaxivity for P22-AACC-Gd at variable field strengths and log τ_M values. The "intersection point" of the horizontal and vertical white lines represents a field strength of 3T and τ_M = 533ns (the established value for P22-AACC-Gd). The system was evaluated at three different τ_R values. a1-2) r_1 (a1) and r_1/r_2 (a2) contour plots for τ_R = 16ns (the established value for P22-AACC-Gd). b1-2) r_1 (b1) and r_1/r_2 (b2) contour plots for τ_R = 1ns. c1-2) r_1 (a1) and r_1/r_2 (a2) contour plots for τ_R = 0.1ns. The 2D plots reveal optimal performance of this system for the given "intersection point" occurs when τ_R = 1ns, with r_1 = 13.0$mM^{-1}sec^{-1}$, r_1/r_2 = 0.78.

Eqn. B1 (Relaxivity Equations):[36]

Analytical equation containing the decay constant, T_1, for the recovery of the net nuclear spin magnetization for a sample placed in a magnetic field which has be tilted out of equilibrium:

$$M_z(t) = M_{z\ Equilibrium}\left(1 - e^{\frac{-t}{T_1}}\right)$$

- $M_z(t)$ nuclear spin magnetization in the z axis at time t in units of seconds
- $M_{z\ Equilibrium}$ equilibrium state of the nuclear spin magnetization in the z axis (maximum magnetization)
- T_1 decay constant for the recovery of spin in units of seconds

Observed T_1 of a specific sample type with a contrast agent present:

$$T_{1\ Observed} = \left[\frac{1}{T_{1\ Sample}} + (r_1)[Contrast\ Agent]\right]^{-1}$$

- r_1 relaxivity of a contrast agent in units of mM^{-1} $seconds^{-1}$
- $[Contrast\ Agent]$ concentration of the contrast agent in units of mM

Solomon-Bloembergen-Morgan (SBM) model for PRE:

Relaxivity of contrast agent including the dipolar, scalar and Currie relaxation mechanisms:

$$r_1 = \frac{q \cdot [Contrast\ Agent]}{[Water]} \left[\frac{1}{T_{1M} + \tau_M}\right]$$

$$r_1 = \frac{q \cdot [Contrast\ Agent]}{[Water]} \left[\frac{1}{\left(\frac{1}{T_{1M}^{dipolar}} + \frac{1}{T_{1M}^{scalar}} + \frac{1}{T_{1M}^{currie}}\right) + \tau_M}\right]$$

$[Water] = 55.6 Molar$	concentration of water in units of (moles / liter), (fixed value)
q	number of inner sphere waters that bind to the Gd ion, (fitting parameter)
$T_{1M}^{dipolar}$	dipolar contribution to the relaxation time
T_{1M}^{scalar}	scalar contribution to the relaxation time
T_{1M}^{currie}	Currie contribution to the relaxation time
τ_M	residence time for the Gd bound water molecule, (fitting parameter)

Relaxivity of contrast agent considering only the dipolar relaxation mechanism (the dipolar mechanism was only considered in the fitting of the NMRD profiles in this work):

$$r_1 = \frac{q \cdot [Contrast\ Agent]}{[Water]} \left[\frac{1}{T_{1M}^{dipolar} + \tau_M}\right]$$

SBM analytical description of the dipolar relaxation time:

$$T_{1M}^{dipolar} = \frac{2C_{dd}}{15r_{1s}^6}[3J(\omega_1, \tau_{d1}) + 7J(\omega_s, \tau_{d2})]$$

Prefactor for relaxation:

$$C_{dd} = \gamma_I^2 \gamma_S^2 \hbar^2 S(S+1)\left(\frac{\mu_0}{4\pi}\right)^2$$

$\gamma_I = 2.675 \cdot 10^8$ nuclear gyromagnetic ratio (second^{-1} Tesla^{-1})

$\gamma_S = -1.760859778 \cdot 10^{11}$ electromagnetic gyromagnetic ratio (second^{-1} Tesla^{-1})

$\hbar = 1.054571628 \cdot 10^{-34}$ Plank's constant (Joules · second)

$S = 7/2$ spin quantum number for the Gd ion

$\mu_0 = 4\pi \cdot 10^{-7}$ magnetic permeability of free space (Newton · Amps^{-2})

$r_{1s}^6 = 3 \cdot 10^{-10}$ distance between the nuclear and the electronic spin (meters),(fixed value)

Spectral density function:

$$J(\omega, \tau) = \frac{\tau}{1 + \omega^2 \tau^2}$$

ω Larmor frequency of nuclear or electric spin

τ correlation time where τ is either τ_{d1} or τ_{d2}

Correlation times in units of seconds:

$$\tau_{d1} = \left(\frac{1}{\tau_R} + \frac{1}{\tau_M} + \frac{1}{T_{1e}}\right)^{-1}$$

and

$$\tau_{d2} = \left(\frac{1}{\tau_R} + \frac{1}{\tau_M} + \frac{1}{T_{2e}}\right)^{-1}$$

τ_R rotational correlation time for the Gd ion, (fitting parameter)

T_{1e} longitudinal electronic relaxation rate

T_{2e} transverse electronic relaxation rate

Electronic relaxation time (longitudinal and transverse) in units of seconds:

$$T_{1e} = \left[\frac{2\Delta^2}{50}(4S(S+1) - 3)\left(\frac{\tau_v}{1 + \omega_S^2\tau_v^2} + \frac{4\tau_v}{1 + 4\omega_S^2\tau_v^2}\right)\right]^{-1}$$

and

$$T_{2e} = \left[\frac{\Delta^2}{50}(4S(S+1) - 3)\left(3\tau_v + \frac{5\tau_v}{1 + \omega_S^2\tau_v^2} + \frac{2\tau_v}{1 + 4\omega_S^2\tau_v^2}\right)\right]^{-1}$$

$\tau_v = 1.4 \cdot 10^{-11}$ correlation time for instantaneous distortions of the metal complex polyhedron in units of seconds, (fixed value in the SBM fit)

$\Delta^2 = 9 \cdot 10^{18}$ mean square fluctuation of the zero-field splitting in units of seconds^{-2}, (fixed value in the SBM fit)

APPENDIX C

SUPPORTING INFORMATION FOR CHAPTER 5

Supplemental Information

Mutagenesis.

The P22(S39C) point mutation was made using established polymerase chain reaction protocols (Qiagen) using pET-11a based plasmids encoding genes for scaffolding and coat protein. The amplified DNA was transformed into E. coli strain BL21 (DE) and selected for ampicillin resistance.[187]

Protein Purification.

Transformed BL21 (DE3) E. coli were grown in 1L cultures inoculated with 1 mL starter culture at 37°C with vigorous shaking overnight. The bacteria were then centrifuged away from the media at 3700 g for 20 minutes. The cell pellets were resuspended in PBS pH 7.2 and were incubated with DNAse, RNAse, and lysozyme (all Sigma-Aldrich) for 30 minutes on ice. Cells were lysed further by sonication on ice. The cell debris was removed via centrifugation at 12,000 g for 45 minutes. The supernatant was then loaded on a 35% sucrose cushion and centrifuged at 48,000 rpm for 50 minutes in an ultra centrifuge (Sorvall). The resulting virus pellet was resuspended in PBS pH 7.0, spun at 17,000 rpm for 20 minutes to remove particulates and lipid providing 135 mg of P22 procapsid (PC). Scaffold protein was extracted using 0.5 M guanidine-HCl in 4 repeated cycles. The P22 empty shells were then dialyzed against PBS pH 7.0 overnight resulting in 86 mg (64% yield) P22 empty shell (ES). The empty shell P22 was heat treated for 20 min at 65^{o}C to transform the protein into its expanded form as previously described and analyzed.[187] The heat treated samples were purified by pelleting as above,

followed by resuspension into PBS pH 7.6 in preparation for protein labeling yielding 58 mg (68% yield form ES) of P22 expanded shell (EX) from 1L of initial E. coli culture.

Subunit Mass Spectrometry.

Subunit masses of the P22 coat and P22-int macroinitiators were analyzed by ESI-Q-TOF mass spectrometry (Q-TOF Premier, Waters) interfaced to a Waters Acquity UPLC and autosampler.[257] Samples were loaded onto a BioBasic-300 SEC column (5 μm, 250 L x 1.0 mm I.D., Thermo Scientific) and eluted with buffer containing 40% isoproanol, 59.9% water, and 0.1% formic acid isocratically with a rate of 25 μL/min. Mass spectra were acquired in the range of m/z 50-5000 and processed using the MaxEnt 1 algorithm for MassLynx version 4.1 to obtain deconvoluted average masses from multiple charge state distributions.

Transmission Electron Microscopy.

The P22-int macroinitiators and P22-polymer composites were imaged by transmission electron microscopy (Leo 912 AB) by negatively staining the sample with 1% uranyl acetate on formvar carbon coated grids. For the diameter measurements 200 particles were measured for each sample.

Denaturing Gel Assay.

P22-int macroinitiators and P22-polymer composites were analyzed using SDS-PAGE on 10-20% gradient Tris-glycine gels (Lonza). Fluorescence imaging of the gels was carried out on a Typhoon TRIO (GE Healthcare) gel scanner with excitation at 488 nm and detection at 526 nm. Protein was detected by staining with Coomassie blue.

Native Agarose Gel Assay.

P22-int macroinitiators and P22-polymer composites were analyzed on 0.8% native agarose gel using 40 mM Tris-base, 5 mM sodium acetate, 1 mM EDTA, pH 8.2 running buffer and were run for 3 hrs at 65 volts. Fluorescence imaging of the gels was carried out on a Typhoon TRIO (GE Healthcare) gel scanner with excitation at 488 nm and detection at 526 nm. Protein was detected by staining with Coomassie blue.

Analytical Ultracentrifugation.

Sedimentation velocity experiments were performed in an XL-A ultracentrifuge (Beckman Coulter, Fullerton, CA) using a AN-60Ti rotor. Epon double-sector centerpieces were filled with 390 μL or 400 μL of sample and the corresponding reference buffer, respectively. The samples were centrifuged at 20°C and 5,000-7,000 rpm. Absorbance data were acquired at wavelength of 280nm. The raw data were analyzed using SEDFIT software, implementing the ls-g*(s) model. Input parameters such as buffer density and viscosity were determined using Sednterp software.

Relaxivity Measurements.

T1 measurements were carried out on Anasazi FT-NMR 60MHz (1.41 T) spectrometer for all samples. Each P22-xAEMA-Gd (0.61 mM Gd, 1.3 mg/mL protein) experimental replicate was diluted with 67% D2O in H2O to yield a dilution series with concentrations of 0.20, 0.068, 0.023 mM Gd. The longitudinal relaxation rate constant (T1) at each dilution was measured using an inversion recovery pulse sequence (90º pulse width of 6.3 μs with 8 experiments of 1 scan) at 298 K, where the relaxation delay was

set to six times the estimated T1 (Figure C12 A-C). To attain the actual T1 value, the following equation for T1 relaxation:

$$Mz = A(1-\exp(-t/T1))+B$$

was fit to the experimental data acquired at each dilution where A, B, and T1 were used as fitting parameters.{Mitchell, 2004 #171} The plot of inverse T1 versus Gd (mM) for the 3 dilutions was used to determine relaxivity values (r1), where relaxivity per Gd is equal to the slope of the line (Figure C12 D) and relaxivity per VLP was calculated by multiplying the slope by Gd/VLP.

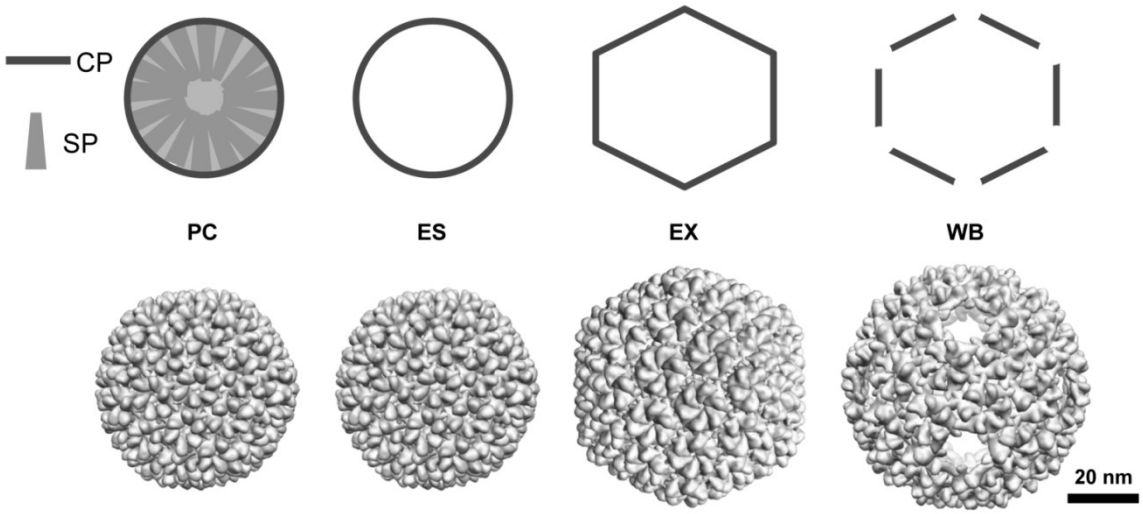

Figure C1: Four unique morphological forms of P22. The coat protein (CP) and scaffold protein (SP) are expressed in *E. coli*. The purified protein architecture is in the procapsid state (PC) containing both CP and SP. After extraction with guanidine•HCl only CP remains in the empty shell (ES) state. If the VLP is heated to 65 ºC the shell enlarges to form the expanded shell (EX) state used in this paper. If instead the ES is heated to 75 ºC the wiffleball (WB) state can be made, where pentons are missing from the icosahedral vertices. PDB ID 3IYI, 2XYZ, 3IYH.

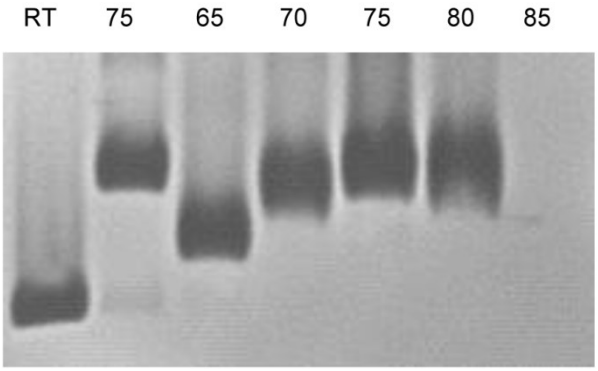

Figure C2: Agarose gel of $P22_{S39C}$-ES heated at different temperatures. Gel labels are heating temperatures in ºC. The states at 65 ºC and 75 ºC correspond to the EX and WB states, respectively. Precipitation occurred while heating at 85 ºC resulting in complete loss of protein.

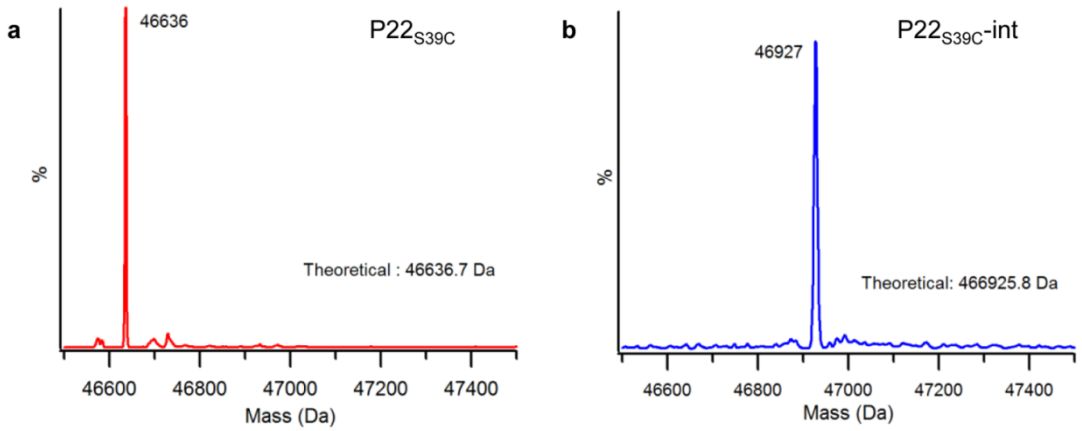

Figure C3: Subunit mass spectrometry characterization of the $P22_{S39C}$ macroinitiator. A) The mass observed is in agreement with the expected mass of the $P22_{S39C}$ mutant B) The only mass observed corresponds to the $P22_{S39C}$-int indicating that all of the subunits have reacted and that there is no significant multiple labeling of the subunits.

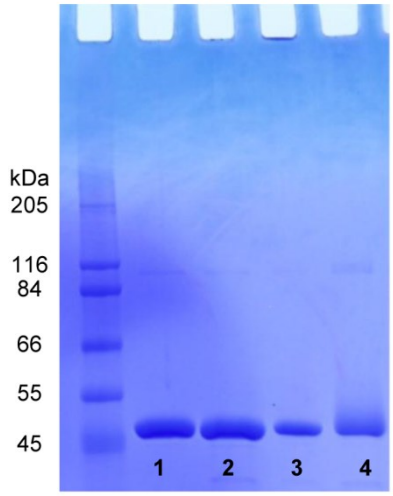

Figure C4: Denaturing gel electrophoresis of P22-polymer samples made with varying amounts of metal catalyst. The amount of catalyst per protein subunit ranged from 0 eq. (lane 1), 10 eq. (lane 2), 40 eq. (lane 3), to 100 eq. (lane 4). Based on this gel 100 eq was determined to be the most effective of these tested conditions.

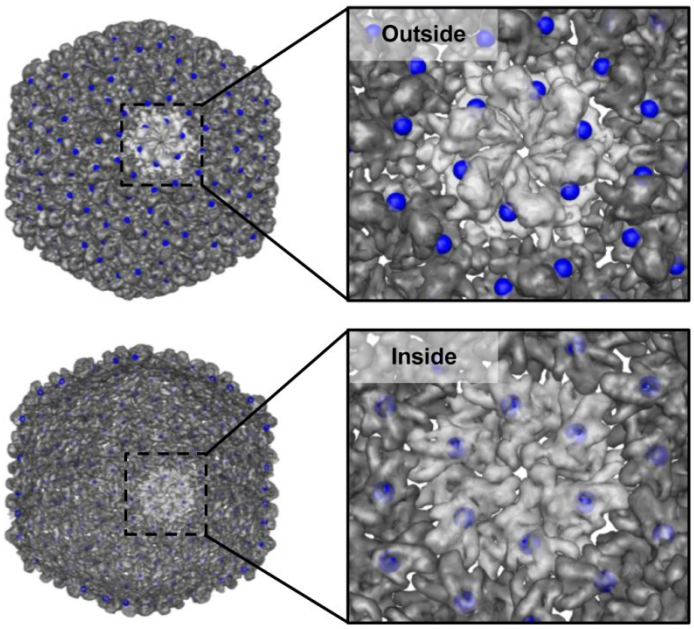

Figure C5: Structural model of the P22 capsid expanded morphology showing the location of the K118C mutation. Location of the modified residue, K118C (in blue), derived from the structural model of P22 using coordination data deposited as PDB file 2XYZ. Both a view of the exterior of the capsid (top) and a half shell cut-away view revealing the interior (bottom) are shown, to illustrate the location of the mutation site.

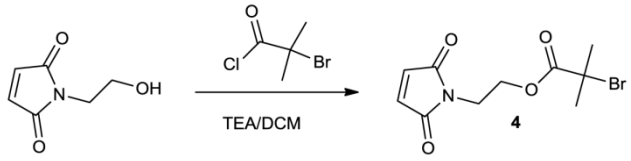

Figure C6: Synthesis of 2-bromoisobutyrate ethoxy maleimide (4). 4 was synthesized by a modification of the procedures previously reported.[110; 203]

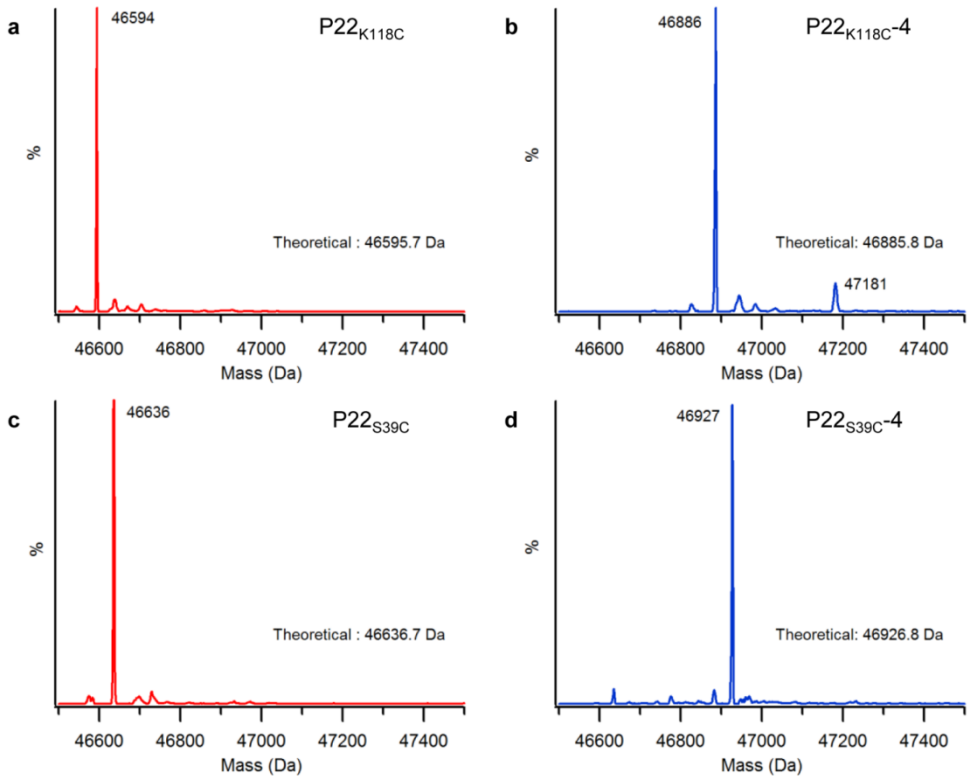

Figure C7: Subunit mass spectrometry characterization of the $P22_{S39C}$-4 and $P22_{K118C}$-4 macroinitiators. A) The mass observed is in agreement with the expected mass of the $P22_{K118C}$ mutant. B) The majority mass observed corresponds to the $P22_{K118C}$-4 indicating that most of the subunits have reacted and that there is less than 5% double labeling (47181 Da) of the subunits. C) The mass observed is in agreement with the expected mass of the $P22_{S39C}$ mutant D) The only mass observed corresponds to the $P22_{S39C}$-4 indicating that all of the subunits have reacted and that there is no significant multiple labeling of the subunits.

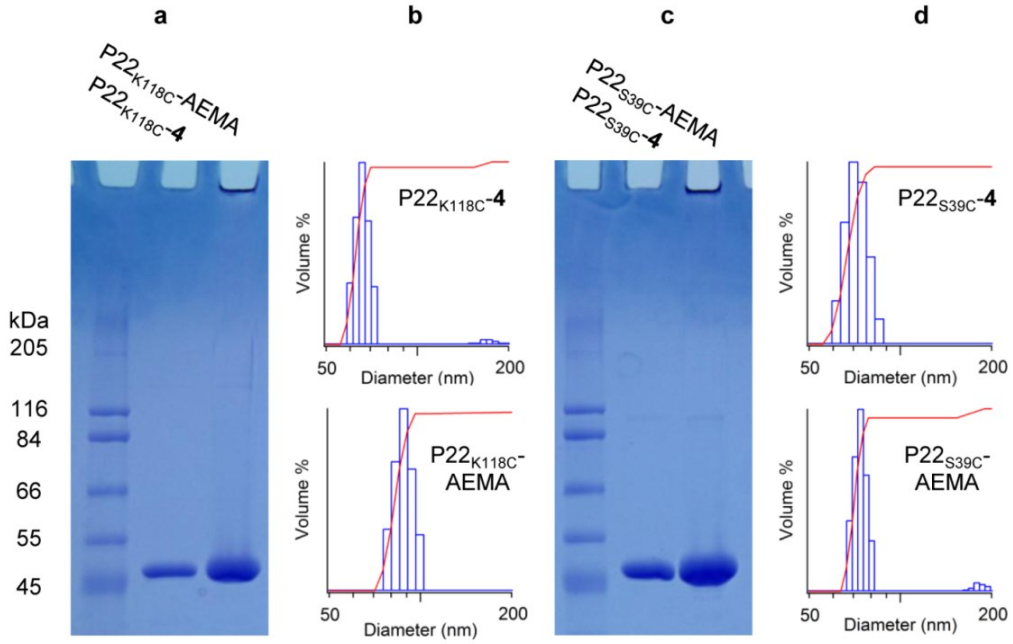

Figure C8: Basic analysis of $P22_{K118C}$-AEMA and $P22_{S39C}$-AEMA. The $P22_{K118C}$-AEMA composite exhibits increased subunit mass, but concomitantly increases in diameter, while the $P22_{S39C}$-AEMA retains its initial diameter. A) $P22_{K118C}$-AEMA analyzed by SDS-PAGE. B) Dynamic light scattering of $P22_{K118C}$-AEMA indicates that at least some of the polymer is on the exterior of the cage through the increase in diameter from 60 ± 3 nm to 81 ± 4 nm. C) $P22_{S39C}$-AEMA analyzed by SDS-PAGE. B) Dynamic light scattering of $P22_{S39C}$-AEMA indicates that the polymer is on the interior of the cage through retention of diameter changing from 72 ± 5 nm to 68 ± 4 nm.

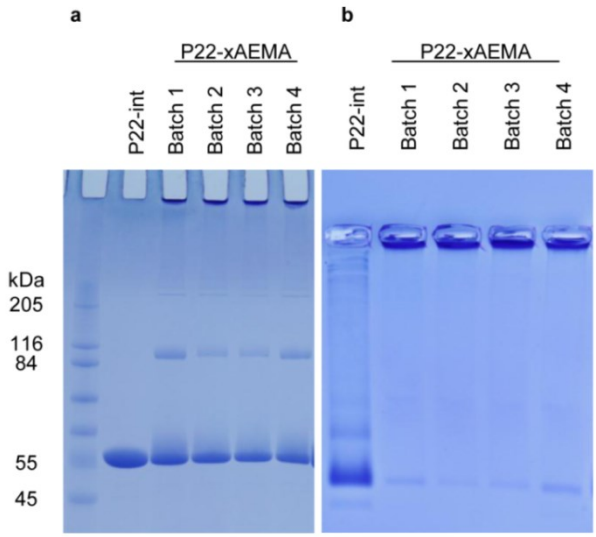

Figure C9: Gel analysis comparison of 4 experimental replicates of the $P22_{S39C}$-xAEMA synthesis. A) When subjected to denaturing gel condition a streak to higher molecular mass and the appearance of dimer due to subunit crosslinking is observed indicating the growth of crosslinked polymer chains on the subunits in each batch. B) When each batch is analyzed by native agarose gel conditions a uniform shift in mobility compared to $P22_{S39C}$-int is observed.

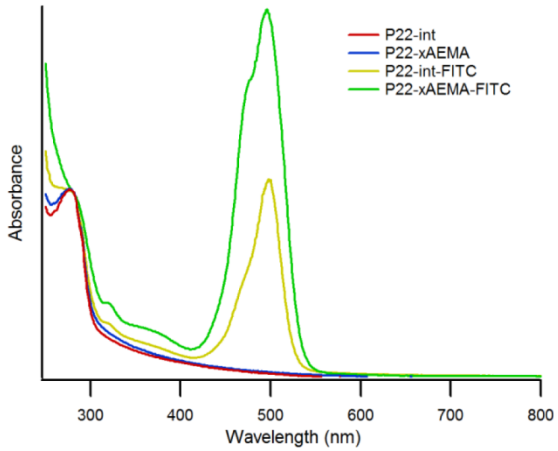

Figure C10: Representative absorbance profiles of the $P22_{S39C}$-int, $P22_{S39C}$-xAEMA, $P22_{S39C}$-int-FITC, and $P22_{S39C}$-xAEMA-FITC. The $P22_{S39C}$-int-FITC is labeled on the intrinsic lysine residues of the protein, while the $P22_{S39C}$-xAEMA-FITC has labeling both on the lysines and the AEMA introduced primary amines. FITC is the contributor to the absorbance at 495 nm, while both the protein-polymer composite and FITC absorb at 280 nm.

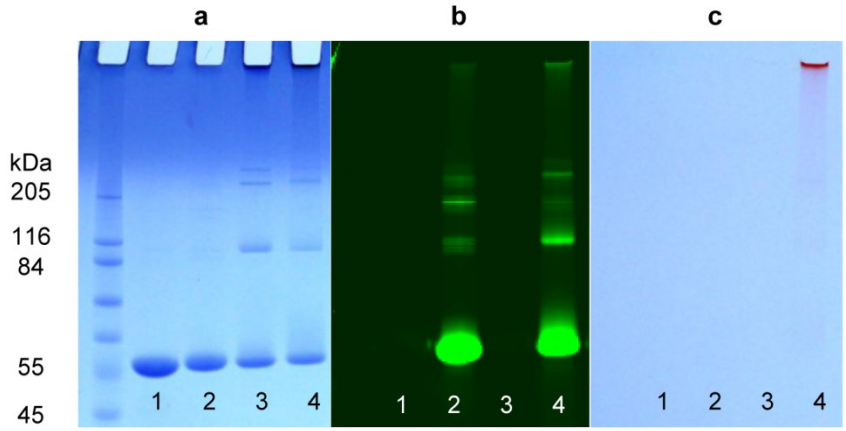

Figure C11: Verification of FITC covalent attachment by denaturing gel electrophoresis. Three different views of the same SDS-PAGE denaturing gel electrophoresis of $P22_{S39C}$-int (lane 1), $P22_{S39C}$-int-FITC (lane 2), $P22_{S39C}$-xAEMA (lane 3), and $P22_{S39C}$-xAEMA-FITC (lane 4). A) The gel after Coomassie staining highlighting the protein component of the samples with the unmodified subunit appearing at about 46 kDa and the modified subunits (lanes 3 and 4) streaking to higher molecular weights. B) Both the $P22_{S39C}$-int-FITC and $P22_{S39C}$-xAEMA-FITC subunits are visible when the fluorescent signal from the FITC is visualized. C) The gel under ambient light. Only the $P22_{S39C}$-xAEMA-FITC is visible as orange streak.

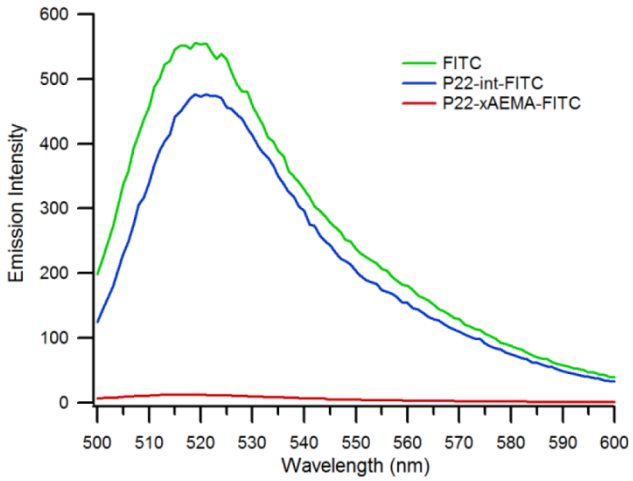

Figure C12: Representative fluorescence emission profiles for FITC labeled samples. In this dataset $P22_{S39C}$-int-FITC and $P22_{S39C}$-xAEMA-FITC compared to free FITC. Each sample had equivalent absorbance at 495 nm and was measured in pH 9.0 buffer. The excitation wavelength was 488 nm and fluorescence emission was detected over the charted range.

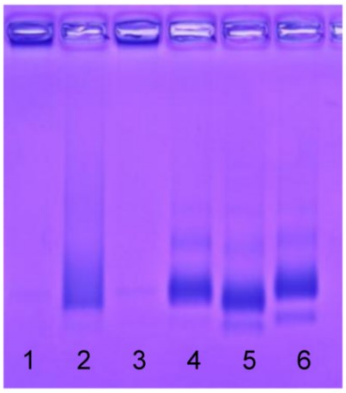

Figure C13: Covalent attachment of Gd-DTPA-NCS monitored by native agarose gel electrophoresis. Native agarose gel analysis of $P22_{S39C}$-xAEMA (lane 1), $P22_{S39C}$-xAEMA-Gd (lane 2), $P22_{S39C}$-xAEMA-magnevist (lane 3), $P22_{S39C}$-int (lane 4), $P22_{S39C}$-int-Gd (lane 5), and $P22_{S39C}$-int-magnevist (lane 6). The attachment of Gd-ATPA-NCS to the polymerized sample has the same effect on electrophoretic mobility as observed in the FITC labeled sample described in Figure 6.

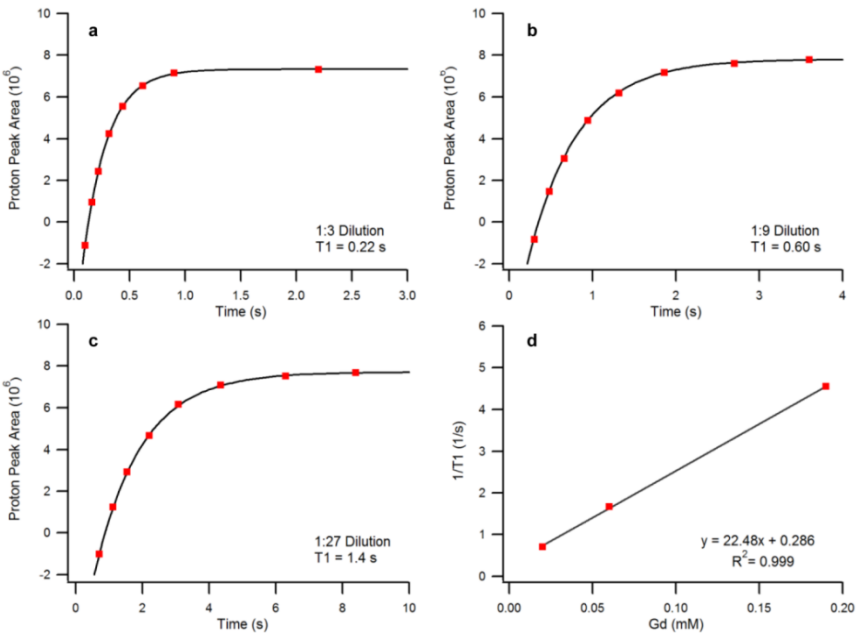

Figure C14: Representative $P22_{S39C}$-xAEMA-Gd data used for relaxivity calculations. A) Raw relaxivity data for the 1:3 dilution sample fit to find T1 at 0.20 mM Gd. B) Raw relaxivity data for the 1:9 dilution sample fit to find T1 at 0.068 mM Gd. C) Raw relaxivity data for the 1:27 dilution sample fit to find T1 at 0.023 mM Gd. D) Plot of 1/T1 values determined in panels A-C fit to determine the ionic relaxivity (r1).

APPENDIX D

SUPPORTING INFORMATION FOR CHAPTER 6

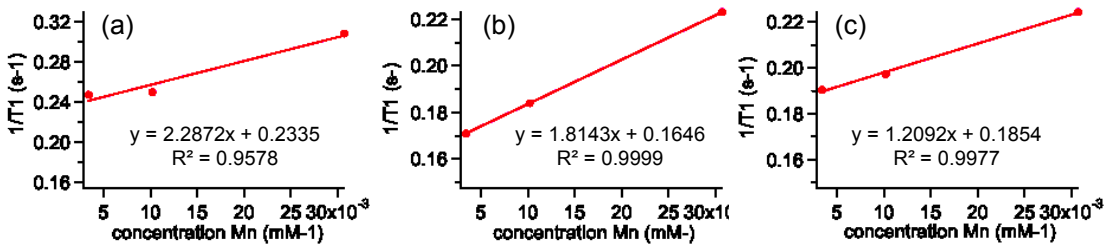

Figure D1: NMR T_1-measurements for P22-xAEMA-MnPP (1,200 MnPP/capsid) at 19 MHz (a), 90 MHz (b), and 300 MHz (c) showing R^2 value close to 1 indicating a good fit, with slope equal to ionic relaxivity.

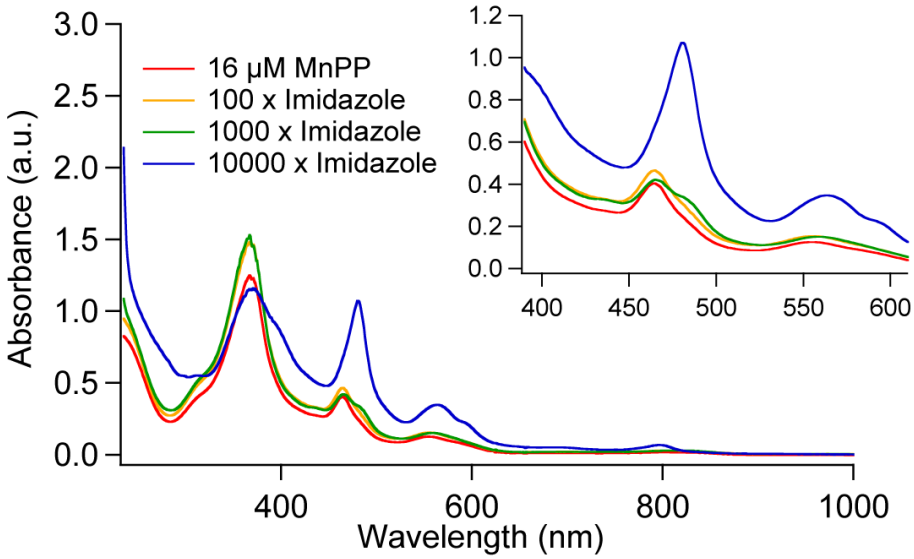

Figure D2: UV-VIS spectrum of imidazole added to free MnPP (red) at molar excess 100 (orange), 1000 (green), and 10000 (blue) excess. Inset: The appearance of the peak at 482 nm indicates binding of imidazole to MnPP

MnPP/capsid	Conc. MnPP inside capsid (mM)	$r_{2,ionic}$ / $r_{1,ionic}$
90	1.09	17.09
121	1.46	9.91
155	1.88	4.94
437	5.29	3.65
719	8.70	2.48
778	9.42	2.51
1,072	13.0	2.18
1,201	14.5	1.75
2,578	31.2	1.54
3,236	39.2	1.48
3,646	44.1	1.32

Green = P22-MnPP w/o EDC, Pink = P22-xAEMA-MnPP w/o EDC,
Orange = P22-MnPP w/EDC, White = P22-xAEMA-MnPP w/EDC

Table D1: P22-VLPs conjugated to MnPP with calculated concentrations of MnPP inside P22 and r_2 / r_1 ratio based on different loading factors.

APPENDIX E

SUPPORTING INFORMATION FOR CHAPTER 7

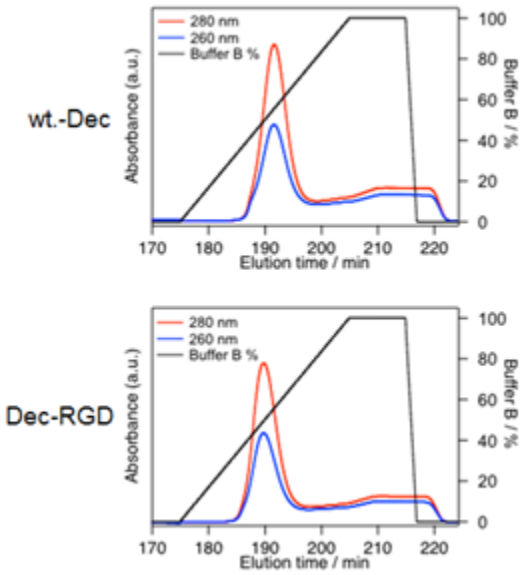

Figure E1: Ni-NTA elusion profile: wt-Dec (top) and Dec-RGD (bottom).

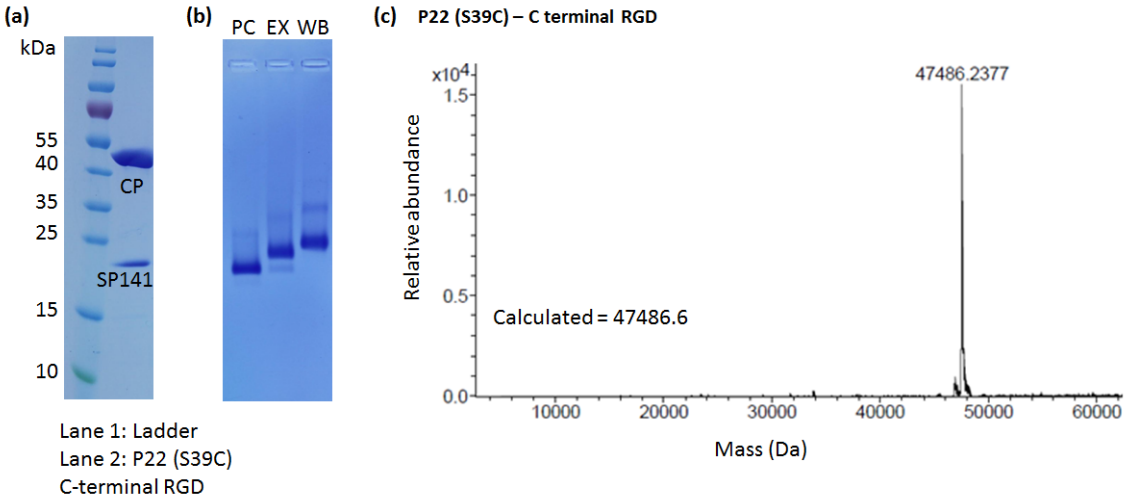

Figure E2: Characterization of P22 (S39C) C-terminal RGD. (a) SDS-PAGE gel showing correct subunit mass of coat protein CP and truncated scaffold protein SP141. (b) Native agarose gel showing morphologies of procapsid PC, expanded shell EX (heated to 65C), and wiffleball WB (heated to 75C), indicated by shifting of bands upward. (c) Subunit mass spectrometry shows correct subunit mass of P22 (S39C) C-terminal RGD

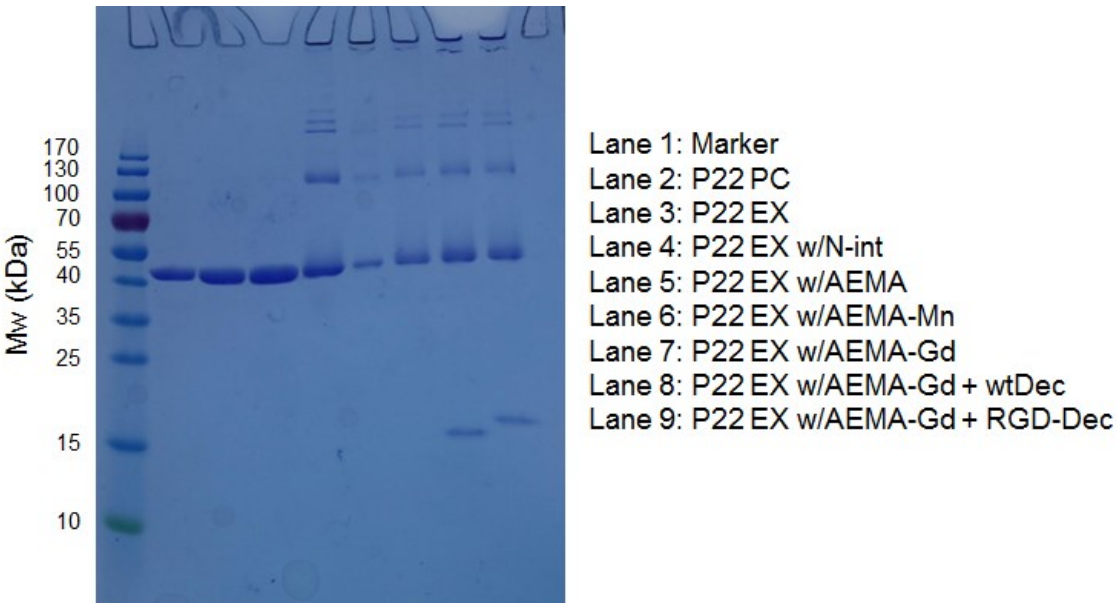

Figure E3: SDS-PAGE gel of P22-xAEMA.

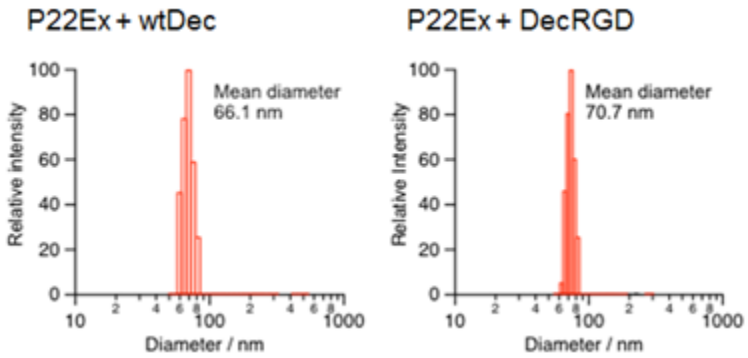

Figure E4: DLS of Dec shows size-distribution of P22 labeled with Dec and Dec mutants do not change size.

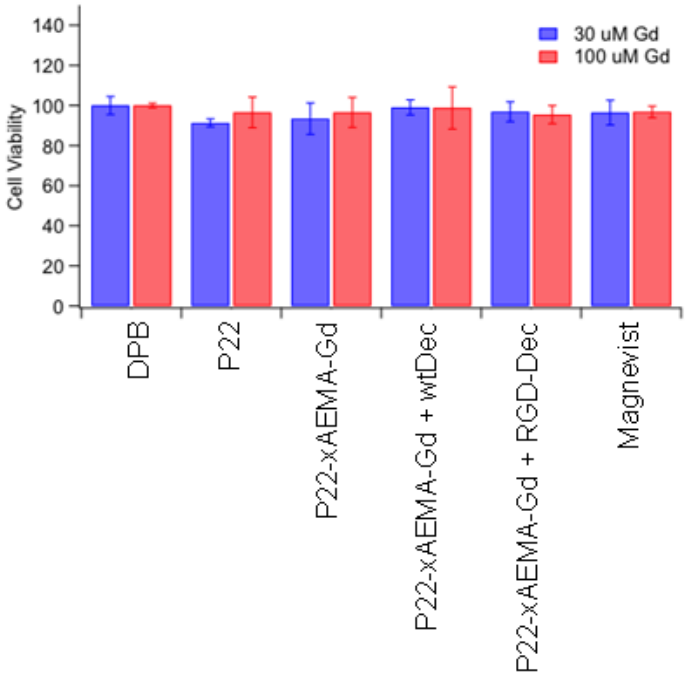

Figure E5. Cell Viability Assay

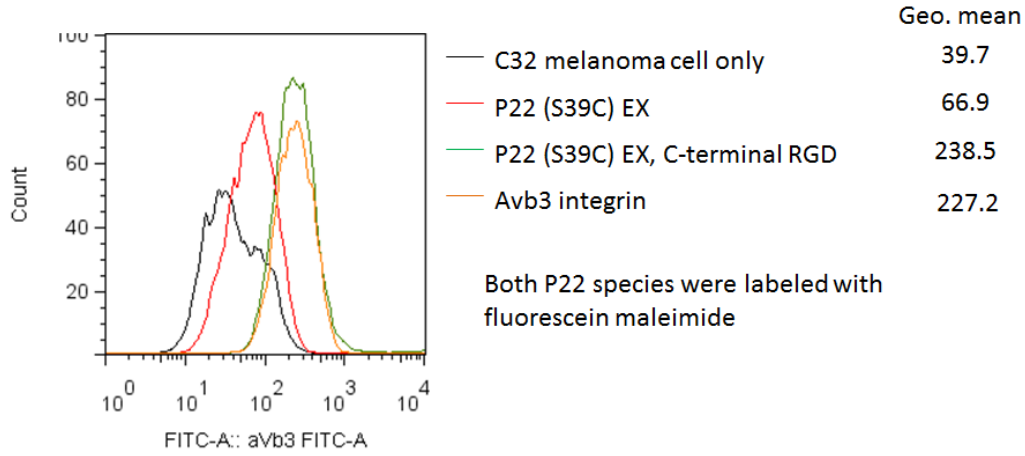

Figure E6: FACS analysis of P22 (S39C) C-terminal RGD. FACS shows that P22 (S39C) C-terminal RGD targets C32 melanoma cells compared to P22 (S39C) control.

REFERENCES CITED

1. Douglas, T., Young, M. (1998). Host-guest encapsulation of materials by assembled virus protein cages. *Nature* 393, 152-155.

2. Meldrum, F. C., Wade, V. J., Nimmo, D. L., Heywood, B. R. and Mann, S. (1991). Synthesis of inorganic nanophase materials in supramolecular protein cages. *Nature* 349, 684-687.

3. Douglas, T., Strable, E., Willits, D., Aitouchen, A., Libera, M., Young, M. (2002). Protein engineering of a viral cage for constrained nanomaterials synthesis. *Adv Mater* 14, 415-.

4. Douglas, T. and Young, M. (2006). Viruses: Making friends with old foes. *Science* 312, 873-875.

5. Koeck, P. J. B., Kagawa, H. K., Ellis, M. J., Hebert, H. and Trent, J. D. (1998). Two-dimensional crystals of reconstituted .beta.-subunits of the chaperonin TF55 from Sulfolobus shibatae. *Biochim Biophys Acta* 1429, 40-44.

6. Trent, J. D. (1996). A review of acquired thermotolerance, heat-shock proteins, and molecular chaperones in archaea. *FEMS Microbiol Rev* 18, 249-258.

7. Kim, K. K., Yokota, H., Santoso, S., Lerner, D., Kim, R. and Kim, S. H. (1998). Purification, crystallization, and preliminary x-ray crystallographic data analysis of small heat shock protein homolog from Methanococcus jannaschii, a hyperthermophile. *Journal of Structural Biology* 121, 76-80.

8. Bozzi, M., Mignogna, G., Stefanini, S., Barra, D., Longhi, C., Valenti, P. and Chiancone, E. (1997). A Novel Non-heme Iron-binding Ferritin Related to the DNA-binding Proteins of the Dps Family in *Listeria innocua*. *Journal of Biological Chemistry* 272, 3259-3265.

9. Grant, R. A., Filman, D. J., Finkel, S. E., Kolter, R. and Hogle, J. M. (1998). The crystal structure of Dps, a ferritin homolog that binds and protects DNA. *Nat Struct Biol* 5, 294-303.

10. Grove, A. and Wilkinson, S. P. (2005). Differential DNA binding and protection by dimeric and dodecameric forms of the ferritin homolog Dps from Deinococcus radiodurans. *J Mol Biol* 347, 495-508.

11. Ramsay, B., Wiedenheft, B., Allen, M., Gauss, G. H., Lawrence, C. M., Young, M. and Douglas, T. (2006). Dps-like protein from the hyperthermophilic archaeon Pyrococcus furiosus. *J Inorg Biochem* 100, 1061-1068.

12. Wiedenheft, B., Mosolf, J., Willits, D., Yeager, M., Dryden, K. A., Young, M. and Douglas, T. (2005). An archaeal antioxidant: Characterization of a Dps-like

protein from Sulfolobus solfataricus. *Proceedings of the National Academy of Sciences of the United States of America* 102, 10551-10556.

13. Zhao, G., Ceci, P., Ilari, A., Giangiacomo, L., Laue, T. M., Chiancone, E. and Chasteen, N. D. (2002). Iron and Hydrogen Peroxide Detoxification Properties of Dps. A Ferritin-Like DNA Binding Protein of *Escherichia coli*. *Journal of Biological Chemistry* epub.

14. Bancroft, J. B., Bracker, C. E. and Wagner, G. W. (1969). Structures derived from cowpea chlorotic mottle and brome mosaic virus protein. *Virology* 38, 324-335.

15. Crick, F. H. C. and Watson, J. D. (1956). STRUCTURE OF SMALL VIRUSES. *Nature* 177, 473-475.

16. Manchester, M. and Steinmetz, N. F. (2009). *Viruses and Nanotechnology*. Current Topics in Microbiology and Immunology, 327.

17. Uchida, M., Klem, M. T., Allen, M., Flenniken, M. L., Gillitzer, E., Varpness, Z., Suci, P., Young, M. J. and Douglas, T. (2007). Protein cage architecture: Containers as templates for materials synthesis. *Adv Mater* 19, 1025-1042.

18. Witus, L. S. and Francis, M. B. (2011). Using Synthetically Modified Proteins to Make New Materials. *Acc Chem Res* 44, 774-783.

19. Allen, M., Willits, D., Mosolf, J., Young, M. and Douglas, T. (2002). Protein Cage Constrained Synthesis of Ferrimagnetic Iron Oxide Nanoparticles. *Adv Mater* 14, 1562-1565.

20. Flenniken, M. L., Willits, D. A., Brumfield, S., Young, M. and Douglas, T. (2003). The small heat shock protein cage from methanococcus jannaschii is a versatile nanoscale platform for genetic and chemical modification. *Nano lett* 3, 1573-1576.

21. Shenton, W., Mann, S., Cölfen, H., Bacher, A. and Fischer, M. (2001). Synthesis of Nanophase Iron Oxide in Lumazine Synthase Capsids. *Angew Chem Int Edit* 40, 442-445.

22. Laufer, B., Steinmetz, N. F., Hong, V., Manchester, M., Kessler, H. and Finn, M. G. (2009). Guiding Vlp's the Right Way: Coating of Virus Like Particles with Peptidic Integrin Ligands. *Biopolymers* 92, 323-323.

23. Raja, K. S., Wang, Q. and Finn, M. G. (2003). Icosahedral virus particles as polyvalent carbohydrate display platforms. *ChemBioChem* 4, 1348-51.

24. Wang, Q., Lin, T. W., Tang, L., Johnson, J. E. and Finn, M. G. (2002). Icosahedral virus particles as addressable nanoscale building blocks. *Angew Chem Int Edit* 41, 459-462.

25. Datta, A., Hooker, J. M., Botta, M., Francis, M. B., Aime, S. and Raymond, K. N. (2008). High relaxivity gadolinium hydroxypyridonate-viral capsid conjugates: Nanosized MRI contrast agents. *J Am Chem Soc* 130, 2546-2552.

26. Hooker, J. M., Datta, A., Botta, M., Raymond, K. N. and Francis, M. B. (2007). Magnetic resonance contrast agents from viral capsid shells: A comparison of exterior and interior cargo strategies. *Nano Lett* 7, 2207-2210.

27. Pettersen, E. F., Goddard, T. D., Huang, C. C., Couch, G. S., Greenblatt, D. M., Meng, E. C. and Ferrin, T. E. (2004). UCSF Chimera—A visualization system for exploratory research and analysis. *Journal of Computational Chemistry* 25, 1605-1612.

28. Qazi, S., Lucon, J., Uchida, M. and Douglas, T. (2013). Protein Cage Nanoparticles for Hybrid Inorganic–Organic Materials. In *Coordination Chemistry in Protein Cages*, pp. 273-304. John Wiley & Sons, Inc.

29. Moghimi, S. M. and Hunter, A. C., Murray, J. C. (2005). Nanomedicine: current status and future prospects. *FASEB J* 19, 311-330.

30. Murthy, M. R. N., Hiremath, C. N. and Savithri, H. S. (1991). Structure and assembly of viruses. In *Molecular conformation and biological interactions* (Balaram, P. & Ramaseshan, S., eds.), pp. 687-702. Indian Institute of Science, Bangalore, India.

31. Yildirimera, L., Thanhb, N. T. K., Loizidoua, M. and Seifaliana, A. M. (2011). Toxicological considerations of clinically applicable nanoparticles. *Nano Today* 6, 585-607.

32. Merbach, A. E. and Tóth, É. (2001). *The chemistry of contrast agents in medical magnetic resonance imaging*, Wiley Online Library.

33. Murthy, S. K. (2007). Nanoparticles in modern medicine: State of the art and future challenges. *Int J Nanomedicine* 2, 129-141.

34. Hermann, P., Kotek, J., Kubicek, V. and Lukes, I. (2008). Gadolinium(iii) complexes as MRI contrast agents: ligand design and properties of the complexes. *Dalton Transactions*, 3027-3047.

35. Caravan, P. (2006). Strategies for increasing the sensitivity of gadolinium based MRI contrast agents. *Chemical Society Reviews* 35, 512-523.

36. Liepold, L., Abedin, M., Buckhouse, E., Frank, J., Young, M. and Douglas, T. (2009). Supramolecular Protein Cage Composite MR Contrast Agents with Extremely Efficient Relaxivity Properties. *Nano Lett* 9, 4520-4526.

37. Caravan, P., Ellison, J., McMurry, T. and Lauffer, R. (1999). Gadolinium(III) chelates as MRI contrast agents: Structure, dynamics, and applications. *Chemical Reviews* 99, 2293-2352.

38. Kluza, E., van der Schaft, D. W. J., Hautvast, P. A. I., Mulder, W. J. M., Mayo, K. H., Griffioen, A. W., Strijkers, G. J. and Nicolay, K. (2009). Synergistic Targeting of avb3 Integrin and Galectin-1 with Heteromultivalent Paramagnetic Liposomes for Combined MR Imaging and Treatment of Angiogenesis. *Nano Lett* 10, 52-58.

39. Mulder, W., Strijkers, G., van Tilborg, G., Griffioen, A. and Nicolay, K. (2006). Lipid-based nanoparticles for contrast-enhanced MRI and molecular imaging. *NMR Biomed* 19, 142-164.

40. Grogna, M., Cloots, R., Luxen, A., Jerome, C., Desreux, J.-F. and Detrembleur, C. (2011). Design and synthesis of novel DOTA(Gd3+)-polymer conjugates as potential MRI contrast agents. *Journal of Materials Chemistry* 21, 12917-12926.

41. Nwe, K., Bryant, L. H. and Brechbiel, M. W. (2010). Poly (amidoamine) dendrimer based MRI contrast agents exhibiting enhanced relaxivities derived via metal preligation techniques. *Bioconjugate Chemistry* 21, 1014-1017.

42. Manus, L. M., Mastarone, D. J., Waters, E. A., Zhang, X.-Q., Schultz-Sikma, E. A., MacRenaris, K. W., Ho, D. and Meade, T. J. (2009). Gd (III)-Nanodiamond Conjugates for MRI Contrast Enhancement. *Nano Lett* 10, 484-489.

43. Anderson, E., Isaacman, S., Peabody, D., Wang, E., Canary, J. and Kirshenbaum, K. (2006). Viral nanoparticles donning a paramagnetic coat: Conjugation of MRI contrast agents to the MS2 capsid. *Nano lett* 6, 1160-1164.

44. Liepold, L., Anderson, S., Willits, D., Oltrogge, L., Frank, J., Douglas, T. and Young, M. (2007). Viral capsids as MRI contrast agents. *Magn Reson Med* 58, 871-879.

45. Prasuhn, D., Yeh, R., Obenaus, A., Manchester, M. and Finn, M. G. (2007). Viral MRI contrast agents: coordination of Gd by native virions and attachment of Gd complexes by azide-alkyne cycloaddition. *Chem Commun* 12, 1269-1271.

46. Jaszberenyi, Z., Moriggi, L., Schmidt, P., Weidensteiner, C., Kneuer, R., Merbach, A. E., Helm, L. and Toth, E. (2007). Physicochemical and MRI characterization of Gd3+-loaded polyamidoamine and hyperbranched dendrimers. *J Biol Inorg Chem* 12, 406-20.

47. Lebduskova, P., Sour, A., Helm, L., Toth, E., Kotek, J., Lukes, I. and Merbach, A. E. (2006). Phosphinic derivative of DTPA conjugated to a G5 PAMAM dendrimer: an 17O and 1H relaxation study of its Gd (III) complex. *Dalton Trans* 28, 3399-406.

48. Rudovsky, J., Botta, M., Hermann, P., Hardcastle, K. I., Lukes, I. and Aime, S. (2006). PAMAM Dendrimeric Conjugates with a Gd-DOTA Phosphinate Derivative and Their Adducts with Polyaminoacids: The Interplay of Global Motion, Internal Rotation, and Fast Water Exchange. *Bioconjug Chem* 17, 975-987.

49. Wickline, S. A., Neubauer, A. M., Winter, P. M., Caruthers, S. D. and Lanza, G. M. (2007). Molecular imaging and therapy of atherosclerosis with targeted nanoparticles. *J Magn Reson Imaging* 25, 667-80.

50. Botta, M. and Tei, L. (2012). Relaxivity Enhancement in Macromolecular and Nanosized GdIII-Based MRI Contrast Agents. *European Journal of Inorganic Chemistry*, 1945-1960.

51. Abedin, M., Liepold, L., Suci, P., Young, M. and Douglas, T. (2009). Synthesis of a Cross-Linked Branched Polymer Network in the Interior of a Protein Cage. *J Am Chem Soc* 131, 4346-4354.

52. Lucon, J., Abedin, M. J., Uchida, M., Liepold, L. O., Young, M. J. and Douglas, T. (2009). Click Based Metal Coordination Polymer Inside Small Heat Shock Protein. *Chem Commun* 46, 264 – 266.

53. Destito, G., Yeh, R., Rae, C. S., Finn, M. G. and Manchester, M. (2007). Folic acid-mediated targeting of cowpea mosaic virus particles to tumor cells. *Chem Biol* 14, 1152-62.

54. Flenniken, M. L., Willits, D. A., Harmsen, A. L., Liepold, L. O., Harmsen, A. G., Young, M. J. and Douglas, T. (2006). Melanoma and lymphocyte cell-specific targeting incorporated into a heat shock protein cage architecture. *Chem Biol* 13, 161-170.

55. Kaiser, C. R., Flenniken, M. L., Gillitzer, E., Harmsen, A. L., Harmsen, A. G., Jutila, M. A., Douglas, T. and Young, M. J. (2007). Biodistribution studies of protein cage nanoparticles demonstrate broad tissue distribution and rapid clearance in vivo. *Int J Nanomed* 2, 715-733.

56. Kaltgrad, E., O'Reilly, M. K., Liao, L., Han, S., Paulson, J. C. and Finn, M. G. (2008). On-Virus Construction of Polyvalent Glycan Ligands for Cell-Surface Receptors. *J Am Chem Soc* 130, 4578-9.

57. Koudelka, K. J., Rae, C. S., Gonzalez, M. J. and Manchester, M. (2007). Interaction between a 54-kilodalton mammalian cell surface protein and cowpea mosaic virus. *J Virol* 81, 1632-40.

58. Koudelka, K. J., Destito, G., Plummer, E. M., Trauger, S. A., Siuzdak, G. and Manchester, M. (2009). Endothelial targeting of cowpea mosaic virus (CPMV) via surface vimentin. *PLoS Pathog* 5, e1000417.

59. Kovacs, E. W., Hooker, J. M., Romanini, D. W., Holder, P. G., Berry, K. E. and Francis, M. B. (2007). Dual-surface-modified bacteriophage MS2 as an ideal scaffold for a viral capsid-based drug delivery system. *Bioconjug Chem* 18, 1140-7.

60. Prasuhn, D. E., Jr., Singh, P., Strable, E., Brown, S., Manchester, M. and Finn, M. G. (2008). Plasma clearance of bacteriophage Qbeta particles as a function of surface charge. *J Am Chem Soc* 130, 1328-34.

61. Rae, C. S., Khor, I. W., Wang, Q., Destito, G., Gonzalez, M. J., Singh, P., Thomas, D. M., Estrada, M. N., Powell, E., Finn, M. G. and Manchester, M. (2005). Systemic trafficking of plant virus nanoparticles in mice via the oral route. *Virology* 343, 224-235.

62. Shriver, L. P., Koudelka, K. J. and Manchester, M. (2009). Viral nanoparticles associate with regions of inflammation and blood brain barrier disruption during CNS infection. *J Neuroimmunol* 211, 66-72.

63. Singh, P., Prasuhn, D., Yeh, R. M., Destito, G., Rae, C. S., Osborn, K., Finn, M. G. and Manchester, M. (2007). Bio-distribution, toxicity and pathology of cowpea mosaic virus nanoparticles in vivo. *J Control Release* 120, 41-50.

64. Steinmetz, N. F. and Manchester, M. (2009). PEGylated viral nanoparticles for biomedicine: the impact of PEG chain length on VNP cell interactions in vitro and ex vivo. *Biomacromolecules* 10, 784-92.

65. Uchida, M., Flenniken, M. L., Allen, M., Willits, D. A., Crowley, B. E., Brumfield, S., Willis, A. F., Jackiw, L., Jutila, M., Young, M. J. and Douglas, T. (2006). Targeting of cancer cells with ferrimagnetic ferritin cage nanoparticles. *J Am Chem Soc* 128, 16626-16633.

66. Uchida, M., Kosuge, H., Terashima, M., Willits, D. A., Liepold, L. O., Young, M. J., Mcconnell, M. V. and Douglas, T. (2011). Protein Cage Nanoparticles Bearing the LyP-1 Peptide for Enhanced Imaging of Macrophage-Rich Vascular Lesions. *ACS Nano* 5, 2493-2502.

67. Bamford, D. H., Grimes, J. M. and Stuart, D. I. (2005). What does structure tell us about virus evolution? *Current Opinion in Structural Biology* 15, 655-663.

68. Prevelige Jr, P. and King, J. (1992). Assembly of bacteriophage P22: a model for ds-DNA virus assembly. *Progress in medical virology* 40, 206-221.

69. Teschke, C. M. and Parent, K. N. (2010). 'Let the phage do the work': Using the phage P22 coat protein structures as a framework to understand its folding and assembly mutants. *Virology* 401, 119-130.

70. Teschke, C. M. (2006). Molecular Glue to Cement a Phage. *Structure* 14, 803-804.

71. Casjens, S. and Weigele, P. (2005). DNA packaging by bacteriophage P22. In *Viral Genome Packaging Machines: Genetics, Structure, and Mechanism*, pp. 80-88. Springer.

72. Rao, V. B. and Feiss, M. (2008). The bacteriophage DNA packaging motor. *Annual review of genetics* 42, 647-681.

73. Lander, G. C., Tang, L., Casjens, S. R., Gilcrease, E. B., Prevelige, P., Poliakov, A., Potter, C. S., Carragher, B. and Johnson, J. E. (2006). The Structure of an Infectious P22 Virion Shows the Signal for Headful DNA Packaging. *Science* 312, 1791-1795.

74. King, J., Lenk, E. V. and Botstein, D. (1973). Mechanism of head assembly and DNA encapsulation in Salmonella phage P22. II. Morphogenetic pathway. *J Mol Biol* 80, 697-731.

75. Prevelige Jr, P. E., Thomas, D. and King, J. (1988). Scaffolding protein regulates the polymerization of P22 coat subunits into icosahedral shells in vitro. *J Mol Biol* 202, 743-757.

76. Parent, K., Khayat, R., Tu, L., Suhanovsky, M., Cortines, J., Teschke, C., Johnson, J. and Baker, T. (2010). P22 Coat Protein Structures Reveal a Novel Mechanism for Capsid Maturation: Stability without Auxiliary Proteins or Chemical Crosslinks. *Structure* 18, 390-401.

77. Chen, D. H., Baker, M. L., Hryc, C. F., DiMaio, F., Jakana, J., Wu, W. M., Dougherty, M., Haase-Pettingell, C., Schmid, M. F., Jiang, W., Baker, D., King, J. A. and Chiu, W. (2011). Structural basis for scaffolding-mediated assembly and maturation of a dsDNA virus. *P Natl Acad Sci USA* 108, 1355-1360.

78. Earnshaw, W., Casjens, S. and Harrison, S. C. (1976). ASSEMBLY OF HEAD OF BACTERIOPHAGE P22 - X-RAY-DIFFRACTION FROM HEADS, PROHEADS AND RELATED STRUCTURES. *J Mol Biol* 104, 387-410.

79. Jiang, W., Li, Z., Zhang, Z., Baker, M. L., Prevelige, P. E., Jr. and Chiu, W. (2003). Coat protein fold and maturation transition of bacteriophage P22 seen at subnanometer resolutions. *Nat Struct Biol* 10, 131-5.

80. Tuma, R., Prevelige, P. E. and Thomas, G. J. (1998). Mechanism of capsid maturation in a double-stranded DNA virus. *P Natl Acad Sci USA* 95, 9885-9890.

81. Greene, B. and King, J. (1994). BINDING OF SCAFFOLDING SUBUNITS WITHIN THE P22 PROCAPSID LATTICE. *Virology* 205, 188-197.

82. Galisteo, M. L. and King, J. (1993). CONFORMATIONAL TRANSFORMATIONS IN THE PROTEIN LATTICE OF PHAGE-P22 PROCAPSIDS. *Biophysical Journal* 65, 227-235.

83. Teschke, C., McGough, A. and Thuman-Commike, P. (2003). Penton release from P22 heat-expanded capsids suggests importance of stabilizing penton-hexon interactions during capsid maturation. *Biophysical Journal* 84, 2585-92.

84. Allen, M., Bulte, J. W. M., Liepold, L., Basu, G., Zywicke, H. A., Frank, J. A., Young, M. and Douglas, T. (2005). Paramagnetic viral nanoparticles as potential high-relaxivity magnetic resonance contrast agents. *Magn Reson Med* 54, 807-812.

85. Datta, A. and Raymond, K. N. (2009). Gdâˆ’Hydroxypyridinone (HOPO)-Based High-Relaxivity Magnetic Resonance Imaging (MRI) Contrast Agents. *Accounts of Chemical Research* 42, 938-947.

86. Garimella, P. D., Datta, A., Romanini, D. W., Raymond, K. N. and Francis, M. B. (2011). Multivalent, High-Relaxivity MRI Contrast Agents Using Rigid Cysteine-Reactive Gadolinium Complexes. *J Am Chem Soc* 133, 14704-14709.

87. Gaberc-Porekar, V., Zore, I., Podobnik, B. and Menart, V. (2008). Obstacles and pitfalls in the PEGylation of therapeutic proteins. *Current Opinion in Drug Discovery and Development* 11, 242.

88. Gauthier, M. A. and Klok, H.-A. (2008). Peptide/protein–polymer conjugates: synthetic strategies and design concepts. *Chemical Communications*, 2591-2611.

89. Qi, Y. and Chilkoti, A. (2014). Growing polymers from peptides and proteins: a biomedical perspective. *Polymer Chemistry* 5, 266-276.

90. Broyer, R., Grover, G. and Maynard, H. (2011). Emerging synthetic approaches for protein-polymer conjugations. *Chem Commun (Camb)* 47, 2212.

91. Lutz, J.-F. and Zarafshani, Z. (2008). Efficient construction of therapeutics, bioconjugates, biomaterials and bioactive surfaces using azide–alkyne "click" chemistry. *Advanced Drug Delivery Reviews* 60, 958-970.

92. Moses, J. E. and Moorhouse, A. D. (2007). The growing applications of click chemistry. *Chemical Society Reviews* 36, 1249-1262.

93. Rostovtsev, V. V., Green, L. G., Fokin, V. V. and Sharpless, K. B. (2002). A Stepwise Huisgen Cycloaddition Process: Copper(I)-Catalyzed Regioselective "Ligation" of Azides and Terminal Alkynes. *Angewandte Chemie* 114, 2708-2711.

94. Tron, G. C., Pirali, T., Billington, R. A., Canonico, P. L., Sorba, G. and Genazzani, A. A. (2008). Click chemistry reactions in medicinal chemistry: Applications of the 1,3-dipolar cycloaddition between azides and alkynes. *Medicinal Research Reviews* 28, 278-308.

95. Xi, W., Scott, T. F., Kloxin, C. J. and Bowman, C. N. (2014). Click Chemistry in Materials Science. *Advanced Functional Materials*, n/a-n/a.

96. Averick, S., Simakova, A., Park, S., Konkolewicz, D., Magenau, A. J. D., Mehl, R. A. and Matyjaszewski, K. (2011). ATRP under Biologically Relevant Conditions: Grafting from a Protein. *ACS Macro Letters* 1, 6-10.

97. Le Droumaguet, B. and Nicolas, J. (2010). Recent advances in the design of bioconjugates from controlled/living radical polymerization. *Polymer Chemistry* 1, 563-598.

98. Matyjaszewski, K. and Tsarevsky, N. V. (2009). Nanostructured functional materials prepared by atom transfer radical polymerization. *Nat Chem* 1, 276-288.

99. Shipp, D. A., Wang, J.-L. and Matyjaszewski, K. (1998). Synthesis of Acrylate and Methacrylate Block Copolymers Using Atom Transfer Radical Polymerization. *Macromolecules* 31, 8005-8008.

100. Siegwart, D. J., Oh, J. K. and Matyjaszewski, K. (2012). ATRP in the design of functional materials for biomedical applications. *Progress in Polymer Science* 37, 18-37.

101. Kolb, H. C., Finn, M. and Sharpless, K. B. (2001). Click chemistry: diverse chemical function from a few good reactions. *Angewandte Chemie International Edition* 40, 2004-2021.

102. Tornøe, C. W., Christensen, C. and Meldal, M. (2002). Peptidotriazoles on Solid Phase: [1,2,3]-Triazoles by Regiospecific Copper(I)-Catalyzed 1,3-Dipolar

Cycloadditions of Terminal Alkynes to Azides. *The Journal of Organic Chemistry* 67, 3057-3064.

103. Gupta, S. S., Kuzelka, J., Singh, P., Lewis, W. G., Manchester, M. and Finn, M. G. (2005). Accelerated Bioorthogonal Conjugation: A Practical Method for the Ligation of Diverse Functional Molecules to a Polyvalent Virus Scaffold. *Bioconjugate Chem* 16, 1572-1579.

104. Wang, Q., Chan, T. R., Hilgraf, R., Fokin, V. V., Sharpless, K. B. and Finn, M. G. (2003). Bioconjugation by Copper(I)-Catalyzed Azide-Alkyne [3 + 2] Cycloaddition. *J Am Chem Soc* 125, 3192-3193.

105. Hong, V., Presolski, S. I., Ma, C. and Finn, M. G. (2009). Analysis and optimization of copper-catalyzed azide-alkyne cycloaddition for bioconjugation. *Angew Chem Int Ed* 48, 9879-83.

106. Pokorski, J. K., Breitenkamp, K., Liepold, L. O., Qazi, S. and Finn, M. G. (2011). Functional virus-based polymer–protein nanoparticles by atom transfer radical polymerization. *J Am Chem Soc* 133, 9242-9245.

107. Lucon, J., Abedin, M. J., Uchida, M., Liepold, L., Jolley, C. C., Young, M. and Douglas, T. (2010). A click chemistry based coordination polymer inside small heat shock protein. *Chem Commun* 46, 264-66.

108. Qazi, S., Liepold, L. O., Abedin, M. J., Johnson, B., Prevelige, P., Frank, J. A. and Douglas, T. (2013). P22 viral capsids as nanocomposite high-relaxivity MRI contrast agents. *Mol Pharm* 10, 11-7.

109. Bontempo, D. and Maynard, H. D. (2005). Streptavidin as a macroinitiator for polymerization: in situ protein-polymer conjugate formation. *J Am Chem Soc* 127, 6508-6509.

110. Heredia, K. L., Bontempo, D., Ly, T., Byers, J. T., Halstenberg, S. and Maynard, H. D. (2005). In situ preparation of protein - "Smart" polymer conjugates with retention of bioactivity. *J Am Chem Soc* 127, 16955-16960.

111. Bloembergen, N. and Morgan, L. (2004). Proton relaxation times in paramagnetic solutions. Effects of electron spin relaxation. *The Journal of Chemical Physics* 34, 842-850.

112. Bloembergen, N., Purcell, E. M. and Pound, R. V. (1948). Relaxation effects in nuclear magnetic resonance absorption. *Physical Review* 73, 679.

113. Solomon, I. (1955). Relaxation processes in a system of two spins. *Physical Review* 99, 559.

114. Burton, D. R., Forsen, S., Karlstrom, G. and Dwek, R. A. (1979). Proton relaxation enhancement (PRE) in biochemistry: a critical survey. *Progress in Nuclear Magnetic Resonance Spectroscopy* 13, 1-45.

115. Lauffer, R. (1987). Paramagnetic Metal-Complexes as Water Proton Relaxation Agents for Nmr Imaging - Theory and Design. *Chemical Reviews* 87, 901-927.

116. Bruckman, M. A., Kaur, G., Lee, L. A., Xie, F., Sepulveda, J., Breitenkamp, R., Zhang, X., Joralemon, M., Russell, T. P., Emrick, T. and Wang, Q. (2008). Surface modification of tobacco mosaic virus with "click" chemistry. *Chembiochem* 9, 519-523.

117. Le Meste, M. and Voilley, A. (1988). Influence of hydration on rotational diffusivity of solutes in model systems. *The Journal of Physical Chemistry* 92, 1612-1616.

118. Resing, H. A. and Wade, C. G. (1976). *Magnetic resonance in colloid and interface science*, American Chemical Society.

119. Lauffer, R. B., Parmelee, D. J., Ouellet, H. S., Dolan, R. P., Sajiki, H., Scott, D. M., Bernard, P. J., Buchanan, E. M., Ong, K. Y. and Tyeklár, Z. (1996). MS-325: a small-molecule vascular imaging agent for magnetic resonance imaging. *Academic radiology* 3, S356-S358.

120. Lattuada, L., Barge, A., Cravotto, G., Giovenzana, G. B. and Tei, L. (2011). The synthesis and application of polyamino polycarboxylic bifunctional chelating agents. *Chem Soc Rev* 40, 3019-3049.

121. Hermanson, G. T. (2008). *Bioconjugate Techniques 2nd Ed*, Elsevier, Rockford, Illinois.

122. Danhier, F., Feron, O. and Preat, V. (2010). To exploit the tumor microenvironment: Passive and active tumor targeting of nanocarriers for anti-cancer drug delivery. *Journal of Controlled Release* 148, 135-146.

123. Matsumura, Y. and Maeda, H. (1986). A NEW CONCEPT FOR MACROMOLECULAR THERAPEUTICS IN CANCER-CHEMOTHERAPY - MECHANISM OF TUMORITROPIC ACCUMULATION OF PROTEINS AND THE ANTITUMOR AGENT SMANCS. *Cancer Research* 46, 6387-6392.

124. Maeda, H., Sawa, T. and Konno, T. (2001). Mechanism of tumor-targeted delivery of macromolecular drugs, including the EPR effect in solid tumor and clinical overview of the prototype polymeric drug SMANCS. *Journal of Controlled Release* 74, 47-61.

125. Wen, A. M., Shukla, S., Saxena, P., Aljabali, A. A. A., Yildiz, I., Dey, S., Mealy, J. E., Yang, A. C., Evans, D. J., Lomonossoff, G. P. and Steinmetz, N. F. (2012). Interior Engineering of a Viral Nanoparticle and Its Tumor Homing Properties. *Biomacromolecules* 13, 3990-4001.

126. Ruoslahti, E. (1996). RGD and other recognition sequences for integrins. *Annual Review of Cell and Developmental Biology* 12, 697-715.

127. Laakkonen, P., Porkka, K., Hoffman, J. A. and Ruoslahti, E. (2002). A tumor-homing peptide with a targeting specificity related to lymphatic vessels. *Nature Medicine* 8, 751-755.

128. Burtea, C., Laurent, S., Port, M., Lancelot, E., Ballet, S., Rousseaux, O., Toubeau, G., Elst, L. V., Corot, C. and Muller, R. N. (2009). Magnetic Resonance Molecular Imaging of Vascular Cell Adhesion Molecule-1 Expression in Inflammatory Lesions Using a Peptide-Vectorized Paramagnetic Imaging Probe. *Journal of Medicinal Chemistry* 52, 4725-4742.

129. Pan, Y., Zhang, Y., Jia, T., Zhang, K., Li, J. and Wang, L. (2012). Development of a microRNA delivery system based on bacteriophage MS2 virus-like particles. *Febs Journal* 279, 1198-1208.

130. Galaway, F. A. and Stockley, P. G. (2013). MS2 Viruslike Particles: A Robust, Semisynthetic Targeted Drug Delivery Platform. *Molecular Pharmaceutics* 10, 59-68.

131. Phillip H. Kuo, A. A.-A., Richard Bucala, Jason Griffith, and Kacie Carlson, M. G., Jeffrey Weinreb, and Shawn Cowper. (2009). MRI in the era of nephrogenic systemic fibrosis: Review, controversies and suggestions for risk reduction. *Applied Radiology* 38, 22-33.

132. Bernstein, E. J., Schmidt-Lauber, C. and Kay, J. (2012). Nephrogenic systemic fibrosis: A systemic fibrosing disease resulting from gadolinium exposure. *Best Practice & Research in Clinical Rheumatology* 26, 489-503.

133. Broome, D. R., Girguis, M. S., Baron, P. W., Cottrell, A. C., Kjellin, I. and Kirk, G. A. (2007). Gadodiamide-Associated Nephrogenic Systemic Fibrosis: Why Radiologists Should Be Concerned. *American Journal of Roentgenology* 188, 586-592.

134. Daftari Besheli, L., Aran, S., Shaqdan, K., Kay, J. and Abujudeh, H. (2014). Current status of nephrogenic systemic fibrosis. *Clinical Radiology* xxx, e1-e8.

135. Grobner, T. (2006). Gadolinium – a specific trigger for the development of nephrogenic fibrosing dermopathy and nephrogenic systemic fibrosis? *Nephrology Dialysis Transplantation* 21, 1104-1108.

136. Haemel, A. K., Sadowski, E. A., Shafer, M. M. and Djamali, A. (2011). Update on nephrogenic systemic fibrosis: are we making progress? *International Journal of Dermatology* 50, 659-666.

137. High, W. A., Ayers, R. A., Chandler, J., Zito, G. and Cowper, S. E. (2007). Gadolinium is detectable within the tissue of patients with nephrogenic systemic fibrosis. *Journal of the American Academy of Dermatology* 56, 21-26.

138. Kitajima, K., Maeda, T., Watanabe, S., Ueno, Y. and Sugimura, K. (2012). Recent topics related to nephrogenic systemic fibrosis associated with gadolinium-based contrast agents. *International Journal of Urology* 19, 806-811.

139. Marckmann, P., Skov, L., Rossen, K., Dupont, A., Damholt, M. B., Heaf, J. G. and Thomsen, H. S. (2006). Nephrogenic Systemic Fibrosis: Suspected Causative Role of Gadodiamide Used for Contrast-Enhanced Magnetic Resonance Imaging. *Journal of the American Society of Nephrology* 17, 2359-2362.

140. Mayr, M. and Bongartz, G. (2011). Nephrogenic systemic fibrosis: what is the risk and how to prevent it? *Gefasschirurgie* 16, 462-468.

141. Reiter, T., Ritter, O., Prince, M. R., Nordbeck, P., Wanner, C., Nagel, E. and Bauer, W. R. (2012). Minimizing Risk of Nephrogenic systemic fibrosis in Cardiovascular Magnetic Resonance. *Journal of Cardiovascular Magnetic Resonance* 14.

142. Sadowski, E. A., Bennett, L. K., Chan, M. R., Wentland, A. L., Garrett, A. L., Garrett, R. W. and Djamali, A. (2007). Nephrogenic Systemic Fibrosis: Risk Factors and Incidence Estimation. *Radiology* 243, 148-157.

143. Tamburrini, O. and Balducci, A. (2012). Gadolinium and nephrogenic systemic fibrosis: have the alarm bells been silenced? *Radiologia Medica* 117, 1-5.

144. Thomsen, H. (2014). Nephrogenic Systemic Fibrosis and Gadolinium-Based Contrast Media. In *Contrast Media* (Thomsen, H. S. & Webb, J. A. W., eds.), pp. 207-217. Springer Berlin Heidelberg.

145. Waikhom R, T. A. (2011). Nephrogenic systemic fibrosis: A brief review. . *Indian J Dermatol* 56, 54-58.

146. Wang, Y., Alkasab, T. K., Narin, O., Nazarian, R. M., Kaewlai, R., Kay, J. and Abujudeh, H. H. (2011). Incidence of Nephrogenic Systemic Fibrosis after Adoption of Restrictive Gadolinium-based Contrast Agent Guidelines. *Radiology* 260, 105-111.

147. Harris, J. M. and Chess, R. B. (2003). Effect of pegylation on pharmaceuticals. *Nature Reviews Drug Discovery* 2, 214-221.

148. Hu, C.-M. J., Fang, R. H., Luk, B. T. and Zhang, L. (2014). Polymeric nanotherapeutics: clinical development and advances in stealth functionalization strategies. *Nanoscale* 6, 65-75.

149. Steinmetz, N. F. (2010). Viral nanoparticles as platforms for next-generation therapeutics and imaging devices. *Nanomed Nanotech Biol Med* 6, 634-641.

150. Strable, E. and Finn, M. G. (2009). Chemical modification of viruses and virus-like particles. *Current Topics in Microbiology and Immunology* 327, 1-21.

151. Brown, S., Fiedler, J. and Finn, M. G. (2009). Assembly of hybrid bacteriophage Qbeta virus-like particles. *Biochemistry* 48, 11155-11157.

152. Mora-Huertas, C. E., Fessi, H. and Elaissari, A. (2010). Polymer-based nanocapsules for drug delivery. *Int J Pharm* 385, 113-142.

153. Petros, R. A. and DeSimone, J. M. (2010). Strategies in the design of nanoparticles for therapeutic applications. *Nat Rev Drug Discov* 9, 615-627.

154. However, the production of polymeric nanoparticles with precise structural homogeneity remains a challenge to the field. Good control over size has been achieved in many systems, including polymer nanoparticles, such as: (a) Duan, H.; Kuang, M.; Zhang, G.; Wang, D.; Kurth, D. G.; Möhwald, H. *Langmuir* **2005**, *21*, 11495-11499. (b) Yanagishita, T.; Fujimura, R.; Nishio, K.; Masuda, H. *Langmuir* **2009**, *26*, 1516-1519. (c) An, S. Y.; Bui, M.-P. N.; Nam, Y. J.; Han, K. N.; Li, C. A.; Choo, J.; Lee, E. K.; Katoh, S.; Kumada, Y.; Seong, G. H. *J. Colloid Interfac. Sci.* **2009**, *331*, 98-103. NOTE.

155. Brunel, F. M., Lewis, J. D., Destito, G., Steinmetz, N. F., Manchester, M., Stuhlmann, H. and Dawson, P. E. (2010). Hydrazone ligation strategy to assemble multifunctional viral nanoparticles for cell imaging and tumor targeting. *Nano lett* 10, 1093-1097.

156. Holder, P. G., Finley, D. T., Stephanopoulos, N., Walton, R., Clark, D. S. and Francis, M. B. (2010). Dramatic thermal stability of virus-polymer conjugates in hydrophobic solvents. *Langmuir* 26, 17383-8.

157. Hu, Y. X., Samanta, D., Parelkar, S. S., Hong, S. W., Wang, Q. A., Russell, T. P. and Emrick, T. (2010). Ferritin-Polymer Conjugates: Grafting Chemistry and Integration into Nanoscale Assemblies. *Advanced Functional Materials* 20, 3603-3612.

158. Zeng, Q., Li, T., Cash, B., Li, S., Xie, F. and Wang, Q. (2007). Chemoselective derivatization of a bionanoparticle by click reaction and ATRP reaction. *Chemical Communications (Cambridge, United Kingdom)*, 1453-5.

159. Li, H., Li, M., Yu, X., Bapat, A. P. and Sumerlin, B. S. (2011). Block copolymer conjugates prepared by sequentially grafting from proteins via RAFT. *Polym Chem*, Advance Article: doi 10.1039/c1py00031d.

160. Many examples exist showing radial polymerization from polymer and metal nanoparticles. For reviews, see: (a) Barbey, R.; Lavanant, L.; Paripovic, D.; Schuwer, N.; Sugnaux, C.; Tugulu, S.; Klok, H.-A. *Chem. Rev.* **2009**, *109*, 5437-5527. (b) Zou, H.; Wu, S.; Shen, J. *Chem. Rev.* **2008**, *108*, 3893-3957. For key examples, see: (c) Ali, A.M.I.; Mayes, A.G. *Macromolecules* **2010**, *43*, 837-844. (d) Skaff, H.; Emrick, T. *Angew. Chem., Int. Ed.* **2004**, *43*, 5383-5386. (e) Perruchot, C.; Khan, M.A.; Kamitsi, A.; Armes, S.P.; Von Werne, T.; Patten, T.E. *Langmuir* **2001**, *17*, 4479-4481. NOTE.

161. De, P., Li, M., Gondi, S. R. and Sumerlin, B. S. (2008). Temperature-regulated activity of responsive polymer-protein conjugates prepared by grafting-from via RAFT polymerization. *J Am Chem Soc* 130, 11288-11289.

162. Lele, B. S., Murata, H., Matyjaszewski, K. and Russell, A. J. (2005). Synthesis of uniform protein-polymer conjugates. *Biomacromolecules* 6, 3380-3387.

163. Control experiments showed that no degradation of or insertion into the tertiary bromide initiation site occurs under CuAAC reaction conditions. NOTE.

164. Peeler, J. C., Woodman, B. F., Averick, S., Miyake-Stoner, S. J., Stokes, A. L., Hess, K. R., Matyjaszewski, K. and Mehl, R. A. (2010). Genetically encoded initiator for polymer growth from proteins. *J Am Chem Soc* 132, 13575-13577.

165. Golas, P., Tsarevsky, N., Sumerlin, B., Walker, L. and Matyjaszewski, K. (2007). Multisegmented Block Copolymers by'Click'Coupling of Polymers Prepared by ATRP. *Aust J Chem* 60, 400-404.

166. Tsarevsky, N. V., Sumerlin, B. S. and Matyjaszewski, K. (2005). Step-growth "click" coupling of telechelic polymers prepared by atom transfer radical polymerization. *Macromolecules* 38, 3558-3561.

167. Gao, W., Liu, W., Christensen, T., Zalutsky, M. and Chilkoti, A. (2010). In situ growth of a PEG-like polymer from the C terminus of an intein fusion protein improves pharmacokinetics and tumor accumulation. *Proceedings of the National Academy of Sciences of the United States of America* 107, 16432-16437.

168. Zhang, S., Li, J., Lykotrafitis, G., Bao, G. and Suresh, S. (2009). Size-Dependent Endocytosis of Nanoparticles. *Adv Mater* 21, 419-424.

169. De Jesus, O. L. P., Ihre, H. R., Gagne, L., Frechet, J. M. J. and Szoka, F. C. (2002). Polyester dendritic systems for drug delivery applications: In vitro and in vivo evaluation. *Bioconjugate Chemistry* 13, 453-461.

170. Bae, Y., Fukushima, S., Harada, A. and Kataoka, K. (2003). Design of environment-sensitive supramolecular assemblies for intracellular drug delivery: Polymeric micelles that are responsive to intracellular pH change. *Angewandte Chemie-International Edition* 42, 4640-4643.

171. Ulbrich, K. and Subr, V. (2004). Polymeric anticancer drugs with pH-controlled activation. *Adv Drug Deliv Rev* 56, 1023-1050.

172. Missirlis, D., Kawamura, R., Tirelli, N. and Hubbell, J. (2006). Doxorubicin encapsulation and diffusional release from stable, polymeric, hydrogel nanoparticles. *Eur J Pharm Sci* 29, 120-129.

173. Mohan, P. and Rapoport, N. (2010). Doxorubicin as a molecular nanotheranostic agent: effect of doxorubicin encapsulation in micelles or nanoemulsions on the ultrasound-mediated intracellular delivery and nuclear trafficking. *Mol Pharm* 7, 1959-1973.

174. Ta, T., Convertine, A. J., Reyes, C. R., Stayton, P. S. and Porter, T. M. (2010). Thermosensitive liposomes modified with poly(N-isopropylacrylamide-co-propylacrylic acid) copolymers for triggered release of doxorubicin. *Biomacromolecules* 11, 1915-20.

175. Karukstis, K. K., Thompson, E. H. Z., Whiles, J. A. and Rosenfeld, R. J. (1998). Deciphering the fluorescence signature of daunomycin and doxorubicin. *Biophysical Chemistry* 73, 249-263.

176. Eichholtz-Wirth, H. (1980). Dependence of the cytostatic effect of adriamycin on drug concenration and exposure time in vitro. *British Journal of Cancer* 41, 886-891.

177. Cormode, D. P., Jarzyna, P. A., Mulder, W. J. M. and Fayad, Z. A. (2010). Modified natural nanoparticles as contrast agents for medical imaging. *Adv Drug Deliver Rev* 62, 329-338.

178. Bumb, A., Brechbiel, M. and Choyke, P. (2010). Macromolecular and dendrimer-based magnetic resonance contrast agents. *Acta Radiologica* 51,, 751-767.

179. Kamaly, N. and Miller, A. (2010). Paramagnetic Liposome Nanoparticles for Cellular and Tumour Imaging. *International Journal of Molecular Sciences* 11,, 1759-1776.

180. Ferreira, M. F., Mousavi, B., Ferreira, P. M., Martins, C. I. O., Helm, L., Martins, J. A. and Geraldes, C. F. G. C. (2012). Gold nanoparticles functionalised with stable, fast water exchanging Gd3+ chelates as high relaxivity contrast agents for MRI. *Dalton T* 41, 5472-5475.

181. Aime, S., Cabella, C., Colombatto, S., Crich, S., Gianolio, E. and Maggioni, F. (2002). Insights into the use of paramagnetic Gd (III) complexes in MR-molecular imaging investigations. *J Magn Reson Im* 16, 394-406.

182. Powell, H., Dhubhghaill, O., Pubanz, D., Helm, L., Lebedev, Y., Schlaepfer, W. and Merbach, A. (1996). Structural and Dynamic Parameters Obtained from ^{17}O NMR, EPR, and NMRD Studies of Monomeric and Dimeric Gd^{3+} Complexes of Interest in Magnetic Resonance Imaging: An Integrated and Theoretically Self-Consistent Approach. *J Am Chem Soc* 118, 9333-9346.

183. Helm, L. (2006). Relaxivity in paramagnetic systems: Theory and mechanisms. *Prog Nucl Mag Res Sp* 49, 45-64.

184. Helm, L. and Merbach, A. (2005). Inorganic and bioinorganic solvent exchange mechanisms. *Chem Rev* 105, 1923-59.

185. Na, H. B., Song, I. C. and Hyeon, T. (2009). Inorganic Nanoparticles for MRI Contrast Agents. *Adv Mater* 21, 2133-2148.

186. Powell, D. H., Dhubhghaill, O. M. N., Pubanz, D., Helm, L., Lebedev, Y. S., Schlaepfer, W. and Merbach, A. E. (1996). Structural and Dynamic Parameters Obtained from 17O NMR, EPR, and NMRD Studies of Monomeric and Dimeric Gd3+ Complexes of Interest in Magnetic Resonance Imaging:â€‰ An Integrated and Theoretically Self-Consistent Approach1. *J Am Chem Soc* 118, 9333-9346.

187. Kang, S., Uchida, M., O'Neil, A., Li, R., Prevelige, P. E. and Douglas, T. (2010). Implementation of P22 Viral Capsids as Nanoplatforms. *Biomacromolecules* 11, 2804-2809.

188. Kang, S., Hawkridge, A., Johnson, K., Muddiman, D. and Prevelige, P. (2006). Identification of Subunit-Subunit Interactions in Bacteriophage P22 Procapsids by Chemical Cross-linking and Mass Spectrometry. *J Proteome Res* 5, 370-377.

189. Crich, S., Biancone, L., Cantaluppi, V., Esposito, D., Russo, S., Camussi, G. and Aime, S. (2004). Improved route for the visualization of stem cells labeled with a Gd-/Eu-chelate as dual (MRI and fluorescence) agent. *Magn Reson Med* 51, 938-944.

190. Bidlingmeyer, B. A., Cohen, S. A. and Tarvin, T. L. (1984). Rapid analysis of amino acids using pre-column derivatization. *J Chromatogr, B: Biomed Sci Appl* 336, 93-104.

191. Grover, G. N. and Maynard, H. D. (2010). Protein-polymer conjugates: synthetic approaches by controlled radical polymerizations and interesting applications. *Curr Opin Chem Biol* 14, 818-827.

192. Krishna, O. D. and Kiick, K. L. (2010). Protein- and Peptide-Modified Synthetic Polymeric Biomaterials. *Biopolymers* 94, 32-48.

193. Thordarson, P., Le Droumaguet, B. and Velonia, K. (2006). Well-defined protein-polymer conjugates-synthesis and potential applications. *Appl Microbiol Biot* 73, 243-254.

194. Depp, V., Alikhani, A., Grammer, V. and Lele, B. S. (2009). Native protein-initiated ATRP: A viable and potentially superior alternative to PEGylation for stabilizing biologics. *Acta Biomaterialia* 5, 560-569.

195. Klok, H. A. (2009). Peptide/Protein-Synthetic Polymer Conjugates: Quo Vadis. *Macromolecules* 42, 7990-8000.

196. Schlick, T. L., Ding, Z. B., Kovacs, E. W. and Francis, M. B. (2005). Dual-surface modification of the tobacco mosaic virus. *J Am Chem Soc* 127, 3718-3723.

197. de la Escosura, A., Nolte, R. J. M. and Cornelissen, J. (2009). Viruses and protein cages as nanocontainers and nanoreactors. *Journal of Materials Chemistry* 19, 2274-2278.

198. Aniagyei, S. E., DuFort, C., Kao, C. C. and Dragnea, B. (2008). Self-assembly approaches to nanomaterial encapsulation in viral protein cages. *Journal of Materials Chemistry* 18, 3763-3774.

199. Dixit, S. K., Goicochea, N. L., Daniel, M. C., Murali, A., Bronstein, L., De, M., Stein, B., Rotello, V. M., Kao, C. C. and Dragnea, B. (2006). Quantum dot encapsulation in viral capsids. *Nano lett* 6, 1993-1999.

200. Comellas-Aragones, M., de la Escosura, A., Dirks, A. J., van der Ham, A., Fuste-Cune, A., Cornelissen, J. and Nolte, R. J. M. (2009). Controlled Integration of Polymers into Viral Capsids. *Biomacromolecules* 10, 3141-3147.

201. Hu, Y. F., Zandi, R., Anavitarte, A., Knobler, C. M. and Gelbart, W. M. (2008). Packaging of a polymer by a viral capsid: The interplay between polymer length and capsid size. *Biophys J* 94, 1428-1436.

202. Abe, S., Hirata, K., Ueno, T., Morino, K., Shimizu, N., Yamamoto, M., Takata, M., Yashima, E. and Watanabe, Y. (2009). Polymerization of Phenylacetylene by Rhodium Complexes within a Discrete Space of apo-Ferritin. *J Am Chem Soc* 131, 6958-60.

203. Mantovani, G., Lecolley, F., Tao, L., Haddleton, D. M., Clerx, J., Cornelissen, J. and Velonia, K. (2005). Design and synthesis of N-maleimido-functionalized

hydrophilic polymers via copper-mediated living radical polymerization: A suitable alternative to PEGylation chemistry. *J Am Chem Soc* 127, 2966-2973.

204. Alidedeoglu, A. H., York, A. W., Rosado, D. A., McCormick, C. L. and Morgan, S. E. (2010). Bioconjugation of D-glucuronic acid sodium salt to well-defined primary amine-containing homopolymers and block copolymers. *Journal of Polymer Science Part a-Polymer Chemistry* 48, 3052-3061.

205. Weinstein, J. N., Yoshikami, S., Henkart, P., Blumenthal, R. and Hagins, W. A. (1977). Liposome-cell interaction: Transfer and intracellular release of a trapped fluorescent marker *Science* 195, 489-492.

206. Chen, R. F. and Knutson, J. R. (1988). Mechanism of fluorescence concentration quenching of carboxyfluorescein in liposomes: Energy transfer to nonfluorescent dimers *Anal Biochem* 172, 61-77.

207. Dunand, F. A., Borel, A. and Helm, L. (2002). Gd(III) based MRI contrast agents: improved physical meaning in a combined analysis of EPR and NMR data? *Inorg Chem Commun* 5, 811-815.

208. Ghaghada, K. B., Ravoori, M., Sabapathy, D., Bankson, J., Kundra, V. and Annapragada, A. (2009). New dual mode gadolinium nanoparticle contrast agent for magnetic resonance imaging. *PLoS One* 4, 1-7.

209. Karfeld-Sulzer, L. S., Waters, E. A., Davis, N. E., Meade, T. J. and Barron, A. E. (2010). Multivalent protein polymer MRI contrast agents: Controlling relaxivity via modulation of amino acid sequence. *Biomacromolecules* 11, 1429-1436.

210. Schuhmanngiampieri, G., Schmittwillich, H., Frenzel, T., Press, W. R. and Weinmann, H. J. (1991). In vivo and in vitro evaluation of Gd-DTPA-polylysine as a macromolecular contrast agent for magnetic resonance imaging. *Invest Radiol* 26, 969-974.

211. Ananta, J. S., Godin, B., Sethi, R., Moriggi, L., Liu, X. W., Serda, R. E., Krishnamurthy, R., Muthupillai, R., Bolskar, R. D., Helm, L., Ferrari, M., Wilson, L. J. and Decuzzi, P. (2010). Geometrical confinement of gadolinium-based contrast agents in nanoporous particles enhances T(1) contrast. *Nature Nanotech* 5, 815-821.

212. Kang, S., Oltrogge, L. M., Broomell, C. C., Liepold, L. O., Prevelige, P. E., Young, M. and Douglas, T. (2008). Controlled assembly of bifunctional chimeric protein cages and composition analysis using noncovalent mass spectrometry. *J Am Chem Soc* 130, 16527-16529.

213. Werner, E. J., Datta, A., Jocher, C. J. and Raymond, K. N. (2008). High-Relaxivity MRI Contrast Agents: Where Coordination Chemistry Meets Medical Imaging. *Angew Chem Int Ed* 47, 8568-8580.

214. Broome, D. R. (2008). Nephrogenic systemic fibrosis associated with gadolinium based contrast agents: A summary of the medical literature reporting. *Eur J Radiol* 66, 230-234.

215. Lin, S. P. and Brown, J. J. (2007). MR contrast agents: Physical and pharmacologic basics. *J Magn Reson Imaging* 25, 884-899.

216. Pan, D., Caruthers, S. D., Senpan, A., Schmieder, A. H., Wickline, S. A. and Lanza, G. M. (2010). Revisiting an old friend: manganese-based MRI contrast agents. *Wiley Interdiscip Rev Nanomed Nanobiotechnol* 3, 162-173.

217. Falk, J. E. (1975). *In: Porphyrins and Metalloporphyrins*. Porphyrins and Metalloporphyrins, Elsevier Scientific Publishing Company, Amsterdam Oxford New York, pp 15-18.

218. Chen, C. W., Cohen, J. S., Myers, C. E. and Sohn, M. (1984). Paramagnetic metalloporphyrins as potential contrast agents in NMR imaging. *FEBS Lett* 168, 70-74.

219. Fiel, R. J., Musser, D. A., Mark, E. H., Mazurchuk, R. and Alletto, J. J. (1990). A comparative study of manganese meso-sulfonatophenyl porphyrins: contrast-enhancing agents for tumors. *Magn Reson Imaging* 8, 255-9.

220. Nasu, H., Takehara, Y., Isogai, S., Kodaira, N., Takeda, H., Saga, T., Nakajima, S., Sakata, I. and Sakahara, H. (2004). Tumor enhancement using Mn-metalloporphyrin in mice: Magnetic resonance imaging and histopathologic correlation. *J Magn Reson Imaging* 20, 294-299.

221. Nelson, J. A. and Schmiedl, U. (1991). Porphyrins as contrast media. *Magn Reson Med* 22, 366-371.

222. Winter, M. B., Klemm, P. J., Phillips-Piro, C. M., Raymond, K. N. and Marletta, M. A. (2013). Porphyrin-Substituted H-NOX Proteins as High-Relaxivity MRI Contrast Agents. *Inorg Chem* 52, 2277-2279.

223. Bruckman, M. A., Yu, X. and Steinmetz, N. F. (2013). Engineering Gd-loaded nanoparticles to enhance MRI sensitivity via T 1 shortening. *Nanotechnology* 24, 462001.

224. Min, J., Jung, H., Shin, H.-H., Cho, G., Cho, H. and Kang, S. (2013). Implementation of P22 Viral Capsids As Intravascular Magnetic Resonance T1

Contrast Conjugates via Site-Selective Attachment of Gd(III)-Chelating Agents. *Biomacromolecules* 14, 2332-2339.

225. Lucon, J., Qazi, S., Uchida, M., Bedwell, G., LaFrance, B., Prevelige, P. E. and Douglas, T. (2012). Use of the interior cavity of the P22 capsid for site-specific initiation of atom-transfer radical polymerization with high-density cargo loading. *Nat Chem* 4, 781-788.

226. Herynek, V., Bulte, J. W. M., Douglas, T. and Brooks, R. A. (2000). Dynamic relaxometry: application to iron uptake by ferritin. *JBIC* 5, 51-56.

227. Koenig, S. H. and Brown, R. D. (1986). Relaxometry of ferritin solutions and the influence of the Fe3+ core ions. 3, 755-767.

228. Schaefle, N. and Sharp, R. (2005). NMR Paramagnetic Relaxation of the Spin 2 Complex MnIIITSPP: A Unique Mechanism. *J Phys Chem A* 109, 3267-3275.

229. Sharp, R., Abernathy, S. M. and Lohr, L. L. (1997). Paramagnetically induced nuclear magnetic resonance relaxation in solutions containing S >= 1 ions: A molecular-frame theoretical and physical model. *J Chem Phys* 107, 7620-7629.

230. Lauffer, R. B. (1987). Paramagnetic metal complexes as water proton relaxation agents for NMR imaging: theory and design. *Chemical Reviews* 87, 901-927.

231. Caravan, P., Farrar, C. T., Frullano, L. and Uppal, R. (2009). Influence of molecular parameters and increasing magnetic field strength on relaxivity of gadolinium- and manganese-based T1 contrast agents. *Contrast Media Mol Imaging* 4, 89-100.

232. Kellar, K. E. and Foster, N. (1992). Relaxation enhancement of water protons by manganese(III) porphyrins: influence of porphyrin aggregation. *Inorg Chem* 31, 1353-1359.

233. Fanali, G., Fesce, R., Agrati, C., Ascenzi, P. and Fasano, M. (2005). Allosteric modulation of myristate and Mn(III)heme binding to human serum albumin. *FEBS Journal* 272, 4672-4683.

234. Neya, S., Morishima, I. and Yonezawa, T. (1981). Binding of imidazoles to manganese(III) protoporphyrin in water. *Biochemistry* 20, 2610-2614.

235. Collman, J. P., Gagne, R. R., Reed, C., Halbert, T. R., Lang, G. and Robinson, W. T. (1975). Picket fence porphyrins. Synthetic models for oxygen binding hemoproteins. *J Am Chem Soc* 97, 1427-1439.

236. McMillan, J. H., Cox, G. G., Kimler, B. F., Spicer, J. S. and Batnitzky, S. (1991). Mn[III] uroporphyrin I: A novel metalloporphyrin contrast agent for magnetic resonance imaging. *Magn Reson Imaging* 9, 553-558.

237. Sur, S. K. and Bryant, R. G. (1995). Spin-Lattice Relaxation Enhancement of Water Protons by Manganese Porphyrins Complexed with Cyclodextrins. *J Phys Chem* 99, 4900-4905.

238. Jolley, C. C., Lucon, J., Uchida, M., Reichhardt, C., Vaughn, M. J., Lafrance, B. J. and Douglas, T. (2011). Structure, dynamics, and solvation in a disordered metal–organic coordination polymer: a multiscale study. *Journal of Coordination Chemistry* 64, 4301-4317.

239. Yonetani, T. and Asakura, T. (1968). Studies on Cytochrome c Peroxidase : XI. A CRYSTALLINE ENZYME RECONSTITUTED FROM APOENZYME AND MANGANESE PROTOPORPHYRIN IX. *J Biol Chem* 243, 3996-3998.

240. Hansson, G. (2005). Mechanisms of disease - Inflammation, atherosclerosis, and coronary artery disease. *New England Journal of Medicine* 352, 1685-1695.

241. Croons, V., Martinet, W, De Meyer, G. (2010). Selective Removal of Macrophages in Atherosclerotic Plaques as a Pharmacological Approach for Plaque Stabilization: Benefits Vs. Potential Complications. *Current Vascular Pharmacology* 8, 495-508.

242. Libby, P. (2002). Inflammation in atherosclerosis. *Nature* 420, 868-874.

243. Wilson, H. M., Barker, RN, Erwig, LP. (2009). Macrophages: Promising Targets for the Treatment of Atherosclerosis. *Current Vascular Pharmacology* 7, 234-243.

244. Choudhury, R., Fisher, EA. (2009). Molecular imaging in atherosclerosis, thrombosis, and vascular inflammation. *Arterioscler Thromb Vasc Biol* 29, 983-991.

245. Jaffer, F., Libby, P, Weissleder, R. (2009). Optical and multimodality molecular imaging: insights into atherosclerosis. *Arterioscler Thromb Vasc Biol* 29, 1017-1024.

246. McCarthy, J. R. and Weissleder, R. (2008). Multifunctional magnetic nanoparticles for targeted imaging and therapy. *Advanced Drug Delivery Reviews* 60, 1241-1251.

247. Uchida, M., Willits, A. D., Muller, K., Willis, A. F., Jackiw, L., Jutila, M., Young, M., Porter, A. E. and Douglas, T. (2009). Intracellular distribution of

macrophage targeting ferriti-iron oxide nanocomposite. *Advanced Materials* 21, 458-62.

248. Laitinen, I., Saraste, A., Weidl, E., Poethko, T., Weber, A. W., Nekolla, S. G., Leppanen, P., Yla-Herttuala, S., Holzlwimmer, G., Walch, A., Esposito, I., Wester, H. J., Knuuti, J. and Schwaiger, M. (2009). Evaluation of alphavbeta3 integrin-targeted positron emission tomography tracer 18F-galacto-RGD for imaging of vascular inflammation in atherosclerotic mice. *Circ Cardiovasc Imaging* 2, 331-8.

249. Waldeck, J., Hager, F., Holtke, C., Lanckohr, C., von Wallbrunn, A., Torsello, G., Heindel, W., Theilmeier, G., Schafers, M. and Bremer, C. (2008). Fluorescence reflectance imaging of macrophage-rich atherosclerotic plaques using an alpha(v)beta(3) integrin-targeted fluorochrome. *J Nucl Med* 49, 1845-1851.

250. Stollman, T. H., Ruers, T. J., Oyen, W. J. and Boerman, O. C. (2009). New targeted probes for radioimaging of angiogenesis. *Methods* 48, 188-92.

251. Parent, K. N., Deedas, C. T., Egelman, E. H., Casjens, S. R., Baker, T. S. and Teschke, C. M. (2012). Stepwise molecular display utilizing icosahedral and helical complexes of phage coat and decoration proteins in the development of robust nanoscale display vehicles. *Biomaterials* 33, 5628-5637.

252. Hayden, M., Adams, M. B. and Casjens, S. (1985). Bacteriophage L: Chromosome physical map and structural proteins. *Virology* 147, 431-440.

253. Gilcrease, E. B., Winn-Stapley, D. A., Hewitt, F. C., Joss, L. and Casjens, S. R. (2005). Nucleotide sequence of the head assembly gene cluster of bacteriophage L and decoration protein characterization. *Journal of bacteriology* 187, 2050-2057.

254. Tang, L., Gilcrease, E. B., Casjens, S. R. and Johnson, J. E. (2006). Highly Discriminatory Binding of Capsid-Cementing Proteins in Bacteriophage L. *Structure (London, England : 1993)* 14, 837-845.

255. Servid, A., Jordan, P., O'Neil, A., Prevelige, P. and Douglas, T. (2013). Location of the Bacteriophage P22 Coat Protein C-Terminus Provides Opportunities for the Design of Capsid-Based Materials. *Biomacromolecules* 14, 2989-2995.

256. Uchida, M., Morris, D. S., Kang, S., Jolley, C. C., Lucon, J., Liepold, L. O., LaFrance, B., Prevelige, P. E. and Douglas, T. (2012). Site-Directed Coordination Chemistry with P22 Virus-like Particles. *Langmuir* 28, 1998-2006.

257. Kang, S., Lander, G. C., Johnson, J. E. and Prevelige, P. E. (2008). Development of Bacteriophage p22 as a platform for molecular display: genetic and chemical modifications of the procapsid exterior surface. *Chembiochem* 9, 514-8.